

Master program in High Energy Physics,  
Astrophysics & Cosmology thesis

---

# **Observations of very-high-energy gamma-ray sources with MAGIC and LST-1 in stereoscopic mode**

---

Juan Jiménez Quiles

Supervised by  
Dr. Abelardo Moralejo



## Abstract

Gamma ray astronomy using ground-based detectors is a relatively new field of study which has a great potential for improvement. In the High-Energy range to Very-High-Energy range transition (from 20 GeV to 20 TeV) the optimal instruments to detect gamma rays are the Imaging Atmospheric Cherenkov Telescopes (IACTs). In this work we analyse the performance of an array of three IACTs: the two MAGIC telescopes and LST-1, the first telescope of the CTA-North observatory, all located in the island of La Palma (Spain). Stereoscopic analysis of the data collected by all three telescopes is expected to improve the performance of MAGIC and LST-1 operated independently. A processing pipeline based on `magic-cta-pipe` [1] has been implemented [2]. Results obtained with different telescope combinations (using the 3-telescopes, MAGIC or LST-1) has been compared. In this case, as LST-1 is relatively young, and not much data has been taken with all three instruments, we will only analyse the Crab Nebula (the standard candle in HE), source for which we have been able to obtain 10.7 h of effective observation time. After the processing, the Instrument Response Functions (IRFs) have been computed, for the angular resolution, an improvement of  $\sim 20\%$  has been obtained compared to MAGIC analysis, reaching an angular resolution of  $0.089^\circ$  at  $\sim 6$  TeV. The obtained integral sensitivity for energies lower and greater than 300 GeV is 2% C.U. and 0.8% C.U. respectively, leading to improvements of the order of 30-50 % comparing to MAGIC and LST-1. Higher-level results also have been obtained. Using the high-level analysis package Gammapy [3], the light curve for energies  $> 64$  GeV has been computed, being compatible with a Crab Nebula flux of  $0.79 \pm 0.16 \times 10^{-9} \text{ cm}^{-2} \text{ s}^{-1}$ . Also, the Spectral Energy Distribution (SED) points obtained by using this work's data, as well as the Fermi-LAT data, have been fitted with a log parabola peaking around 57 GeV. Then, the multiwavelength fit using data from several other facilities, provided us with an estimation of the magnetic field in the Crab Nebula of  $119 \mu\text{G}$ , as well as a phenomenological electron population distribution, modeled with an Exponential Cut-off Broken Power Law (ECBPWL) obtaining an amplitude of  $1.94 \pm 0.15 \times 10^{36} \text{ eV}^{-1}$ .

## Notation and abbreviations

<b>AGN</b>	Active Galactic Nuclei	<b>MAGIC</b>	Major Atmospheric Gamma-ray Imaging Cherenkov
<b>BH</b>	Black Hole	<b>MC</b>	Monte Carlo
<b>CMB</b>	Cosmic Microwave Background	<b>NIR</b>	Near InfraRed
<b>CTA</b>	Cherenkov Telescope Array	<b>NSB</b>	Night Sky Background
<b>DM</b>	Dark Matter	<b>NS</b>	Neutron Star
<b>EBL</b>	Extragalactic Background Light	<b>PMT</b>	PhotoMultiplier Tube
<b>ECBPWL</b>	Exponential Cut-off Broken PoWer Law	<b>PSF</b>	Point Spread Function
<b>FIR</b>	Far InfraRed	<b>PWN</b>	Pulsar Wind Nebula
<b>GRB</b>	Gamma-Ray Burst	<b>RF</b>	Random Forest
<b>HE</b>	High Energy	<b>SA</b>	Surface Array
<b>IACT</b>	Imaging Atmospheric Cherenkov Telescope	<b>SED</b>	Spectral Energy Distribution
<b>IC</b>	Inverse Compton	<b>SMBH</b>	Super Massive Black Hole
<b>IRF</b>	Instrument Response Function	<b>SN</b>	SuperNova
<b>ISM</b>	InterStellar Medium	<b>SSC</b>	Synchrotron Self-Compton
<b>LE</b>	Low Energy	<b>UHE</b>	Ultra-High Energy
<b>LST</b>	Large Size Telescope	<b>VHE</b>	Very-High Energy
		<b>WCD</b>	Water Cherenkov Detector

# Contents

<b>Abstract</b>	<b>I</b>
<b>Notation and abbreviations</b>	<b>II</b>
<b>Index</b>	<b>III</b>
<b>1 Introduction, gamma-ray astronomy</b>	<b>1</b>
1.1 Historical overview & state of the art . . . . .	1
1.2 Cosmic rays and gamma rays . . . . .	3
<b>2 Detection and instrumentation</b>	<b>4</b>
2.1 Space-borne telescopes . . . . .	4
2.2 Atmospheric showers . . . . .	5
2.2.1 Surface Arrays (SAs) and Water Cherenkov detectors (WCDs) . . . . .	7
2.3 Cherenkov radiation . . . . .	7
2.3.1 Imaging Atmospheric Cherenkov Telescopes (IACTs) . . . . .	8
<b>3 Emission mechanisms and sources</b>	<b>13</b>
3.1 Gamma-ray emission mechanisms . . . . .	13
3.2 Sources . . . . .	15
3.3 Crab Nebula . . . . .	17
<b>4 Data analysis pipeline</b>	<b>18</b>
4.1 Data levels . . . . .	18
4.2 Monte Carlo (MC) simulations and Random Forests (RFs) . . . . .	21
4.3 Stereo data taking . . . . .	22
4.4 Implementation . . . . .	23
<b>5 Data sample</b>	<b>25</b>
5.1 Other sources . . . . .	29
<b>6 Checks of the DL2 data</b>	<b>30</b>
6.1 Energy and gammaness reconstruction . . . . .	31
6.2 Direction reconstruction . . . . .	33
6.3 Geometrical reconstruction . . . . .	33
6.4 Instrument Response Functions (IRFs) and instrument characterization . . . . .	36
<b>7 Analysis beyond DL2: Spectrum and light curves</b>	<b>42</b>
7.1 Light curves . . . . .	42
7.2 Spectral Energy Distributions (SEDs) . . . . .	43
7.3 Multiwavelength analysis . . . . .	45
<b>8 Conclusion</b>	<b>48</b>
<b>A Instructions for the processing</b>	<b>55</b>

# 1 Introduction, gamma-ray astronomy

## 1.1 Historical overview & state of the art

The idea of gamma-ray astronomy was born in mid 20th century with the first predictions of processes that could emit gamma rays in the universe. The first ideas of how to look for them, involved using scintillators at high altitudes, or launching detectors on balloons, in the 1960s. But it was not until 1967, that OSO3 (Third Orbiting Solar Observatory) detected the first astrophysical gamma-ray source; the Sun [4], finding the deuterium absorption line at 2.2 MeV.

A few years after, in 1972, the first gamma-ray telescope was launched, SAS-2 (Small Astronomy Satellite 2), with the objective of observing the high energy part of the spectrum [5]. It detected both the gamma-ray background, that is caused by the interaction of cosmic rays with gas and dust, and some possible sources, although they could not be resolved. In 1975 with the launch of COS-B and SAS-3, more evidence of possible sources was found (see Fig.2). These missions also led to finding evidences of gamma-ray emission from the Crab Nebula and the Vela pulsar, among others [6, 7]. All of these initial missions were particularly sensitive to Low-Energy (LE) gamma rays in the range of  $\sim 1$  MeV to 100 MeV because they were also designed to observe the hard X-ray band. Some of them also covered the High-Energy (HE) band i.e. energies ranging from 100 MeV to 100 GeV, for example, the aforementioned COS-B mission.

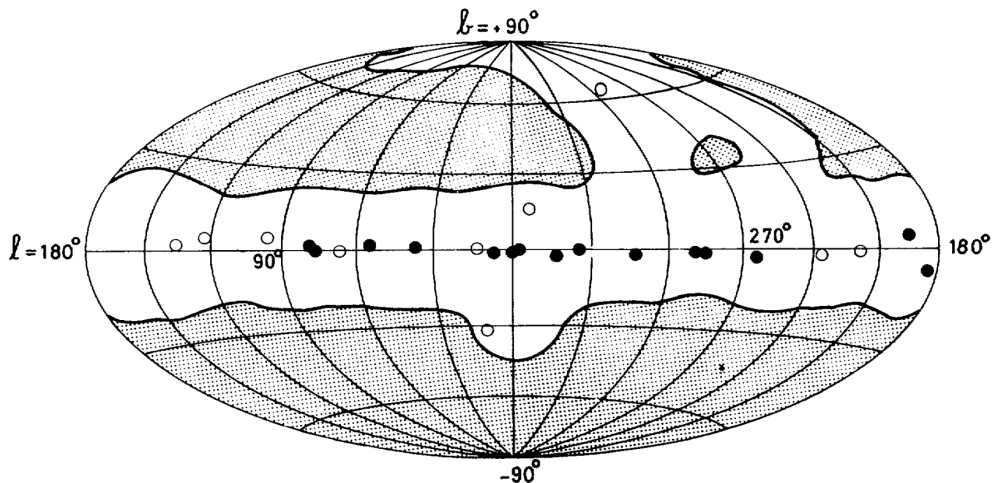


Figure 2: First gamma-ray sky map taken by COS-B in sources with energies above 100 MeV. The area in the sky where COS-B searched (undashed), and the dots are the sources detected, from [8].

These observations opened a new observational window to the universe. Because of the high energy they have, these events were associated to the most violent scenarios in the universe. One significant milestone came after the military detected a mysterious burst of gamma rays in the 1960s. The Vela satellites, that were developed to detect nuclear explosions in space, picked up unidentified burst of gamma rays in 1967, this is the first documented observation of a Gamma-Ray Burst (GRB).

The idea of detecting gamma rays from Earth took shape after the discovery of Cherenkov light in 1934. However, it was not until the 1950s that the first attempts to observe this light from cascades were made. Space-borne telescopes are not efficient at detecting Very-High-Energy (VHE) gamma rays (100 GeV-100 TeV) due to the size limitations of satellites. The small flux of incoming gamma rays within the VHE range and the small size of the telescopes make the

detections highly unlikely. Additionally, they are so small that they are not able to completely stop gamma rays at higher energies. As a result, ground-based telescopes are the only remaining option for detecting efficiently VHE gamma rays. The idea was to use the atmosphere as a calorimeter that absorbs the photons, and to detect the effects of the absorption using instruments on the ground. Several ground-based particle detectors were devised but it was not until the 1960s that the idea of Imaging Atmospheric Cherenkov Telescopes (IACTs) was materialized. Telescopes with effective area orders of magnitude larger than those of space-borne telescopes allowed for the observation of the universe in the VHE gamma-ray band.

At Whipple Observatory with a 10m IACT, the Crab Nebula became the first confirmed source of TeV photons in 1989 [9]. After this, many other important ground-based experiments were built, including the completed projects HEGRA (High Energy Gamma-Ray Astronomy) in the island of La Palma or the CAT (Cherenkov Array at Themis) in France. The currently operational IACTs are MAGIC (Major Atmospheric Gamma Imaging Cherenkov Telescope) in La Palma, HESS (High Energy Stereoscopic System) in Namibia, VERITAS (Very Energetic Radiation Imaging Telescope Array System) in North America, and the LST (Large Size Telescope) which will be part of CTA (Cherenkov Telescope Array), in construction in La Palma and Chile. A summarized sketch of the on ground-based facilities can be seen in Fig.10.

By the early 90s other space instruments were launched, like the Compton Gamma-Ray Observatory (CGRO) mission (see Fig.4), that found also evidence that the Crab and the Vela pulsar emit gamma rays and studied the nature of GRB [10]. The CGRO observations also led to the discovery of new gamma-ray sources, including Active Galactic Nuclei (AGN). Other observatories were launched, in the X-ray to HE range, and with many instruments on board, each with a specific observational purpose, e.g. Granat (1989) [11]. Other ground-based techniques have also been developed such as the Extensive Air Shower Arrays which use arrays of particle detectors, including HAWC (High Altitude Water Cherenkov) in Mexico, CASA (Chicago Air Shower Array) in North America, and the LHAASO (Large High Altitude Air Shower Observatory) experiment, currently under development in Tibet, aims to provide insights into the Ultra-High-Energy (UHE) range, which spans the range from 100 TeV to 100 PeV.

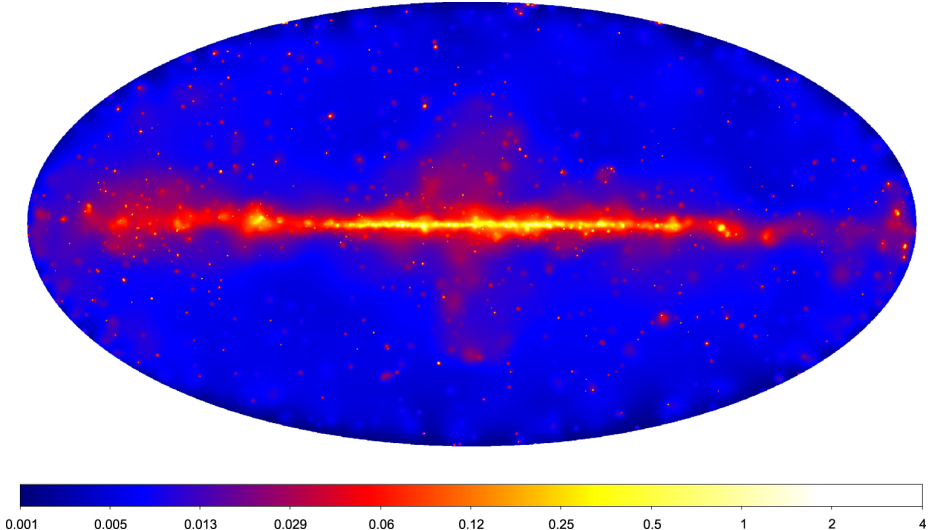


Figure 3: All-sky map done with Fermi, for sources of 50 GeV–2 TeV. In galactic coordinates and the color given in log scale, for counts per  $(0.1^\circ)^2$ , from [12].

With the launch of Chandra in 1999 the gamma-ray counterparts of many X-ray sources were studied. As space telescopes are the only direct way of detecting gamma rays, in the early 2000s

some important missions were launched, for example the INTEGRAL (International Gamma-Ray Astrophysics Laboratory) satellite [13] launched in 2002 and is an ongoing mission. It is a multi wavelength observatory, shown in Fig.4. It was designed to study X-rays and LE gamma rays, and is actually one of the few instruments that cover the energy range around 1 MeV. Other observatories such as the Neil Gehrels Swift Observatory or Gamma-Ray Burst Explorer were also launched. Certainly one of the most important nowadays is the Fermi satellite. Consisting of 2 instruments; LAT and GBM, which cover the HE and the LE bands respectively. It was launched in 2008 and is an instrument capable of performing an all-sky survey every two orbits (3 hours) (see Fig.3), it helped to build a vast catalog of HE gamma-ray emitters, including pulsars, blazars, AGNs or SN remnants [14].

As these important missions are still in operation, the next-generation facilities are already being built, as CTA [15] and LHAASO [16]. One of the primary goals of current and future gamma-ray observatories is to study the sources and mechanisms that produce these phenomena in the universe. This includes investigating the properties of GRB, pulsars, and other objects. The observed VHE gamma rays require scenarios of cosmic rays acceleration to ultrarelativistic energies for their emission. Thus, by studying this radiation, we can investigate cosmic ray accelerators and the various possible mechanisms involved. Another topic related to the study of gamma rays is Dark Matter (DM). DM is considered to be a potential source of gamma-ray radiation via annihilation or decay. There is also significant interest in the multi-wavelength study of GRBs and other transient events, such as those associated with Gravitational Waves.

## 1.2 Cosmic rays and gamma rays

Cosmic rays and gamma rays are two types of HE radiation that are originated in sources beyond our solar system. Both are important fields of research nowadays that try to answer some fundamental questions about the universe. There is a link between the acceleration of cosmic rays to high energies and the production of VHE gamma rays, so these two fields are closely interconnected.

Cosmic rays consist of charged particles, that can be of different types, protons, electrons, atomic nuclei... These particles have VHE and travel at ultrarelativistic velocities. As they are charged particles, they are deflected by magnetic fields, so it is not possible to determine where they come from by simply looking at the direction they have when arriving to Earth. That is why the nature of the cosmic-ray sources is still a subject of speculation, but we are sure that they are coming from very energetic events. They are constantly arriving to Earth at a high rate, even though we are partially shielded by the magnetosphere [17].

Gamma rays, on the other hand, are VHE electromagnetic radiation. The boundary between X-rays and gamma rays is usually defined around 100 keV in energy, corresponding to a wavelength of about 0.01 nm. Gamma rays are believed to be produced by the same astrophysical processes as cosmic rays, but in this case we have the advantage of that, as photons are not charged particles, they are not deflected by the magnetic fields, so studying their direction when arriving to Earth, the position of the source can be inferred. The mechanisms that can emit gamma rays include nuclear decay and electron-positron annihilation in the LE band, synchrotron and curvature radiation in the HE and VHE bands, and Inverse Compton scattering and Bremsstrahlung for the hard VHE. Detecting gamma rays directly is challenging because photons are highly energetic and interact very easily with matter, so it can only be done in space. Additionally, gamma rays can interact with other photons in intergalactic space, the so-called Extragalactic Background Light (EBL), which hinders observations in the VHE band (and above) of very distant sources.

Another type of particle that can be used as astronomical messenger is neutrinos, which are also neutral particles capable of traveling at ultrarelativistic energies. Like gamma rays, they are not deflected, and they are also produced in highly violent phenomena in the universe. Their main characteristic is that they are governed by weak processes, so it is very difficult to induce interactions with matter. This is advantageous because neutrinos do not interact with the EBL and dust, thus, they can open up new windows for observing the universe, but also poses a big challenge for their detection. In order to detect them, large and complex infrastructures are needed, such as the IceCube experiment [18].

## 2 Detection and instrumentation

There are different options that have been used to detect gamma rays over the years, and new and more effective techniques have been developed. Direct gamma-ray detection is only possible in space due to the interaction of gamma rays with the Earth's atmosphere, however, the absorption of a VHE photon in the atmosphere produce detectable effects in ground. Therefore, gamma-ray telescopes can be divided into two major groups: ground-based and space-borne.

### 2.1 Space-borne telescopes

Space-borne telescopes became possible after beginning of space age. Some of the first telescopes to produce gamma-ray sky maps are the CGRO onboard instruments, COMPTEL [19], EGRET [20] and BATSE [21], or the instruments onboard Granat [11]. Telescopes designed for detecting LE photons function differently than those designed for detecting HE photons. For the LE photons, the photoelectric effect dominates, for energies around 1 MeV Compton effect dominates, and finally for photons with energies greater than 20 MeV the pair production should be used in order to detect the photons [22].

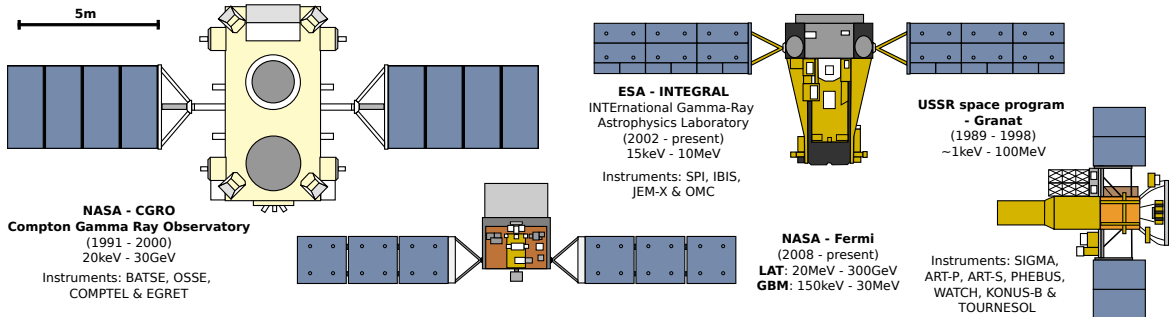


Figure 4: Scaled image of different space-borne gamma ray telescopes. The image shows the operational years, energy ranges and different onboard instruments. Redrawn from [23].

As we are interested in study HE and VHE energies, pair production mechanism will be the one to deal with, so *particle detectors* should be used. Space-borne telescopes have an anti-coincidence shield that detects the charge of the incoming particle so cosmic rays can be discarded in the analysis. With that, the path reconstruction of the  $e^-$  and  $e^+$  inside the detector and the dissipation of energy in the calorimeter, the direction and energy of the gamma ray can be inferred. The most important pair production telescope nowadays is the Large Area Telescope (LAT) on board of the Fermi satellite [24], that has been analysing the sky in the HE range since 2008, Fermi satellite is represented in Fig.4.

Space-borne telescopes have the advantage of the absence of atmosphere or complex processes as atmospheric showers, gamma rays are detected almost directly. Space telescopes also have longer observation time since they are not affected by day-night cycles, and do not need to be pointed at specific locations in space as gamma rays can arrive at the detector from various directions. This is similar for some certain specific ground-based gamma-ray detectors, that we will see later.

## 2.2 Atmospheric showers

In order to detect the gamma rays from ground as they cannot be detected directly because the photons interact in the upper layers of atmosphere. Instead what can be detected are the results of these interactions. We call these type of chain reactions produced by gamma rays as well as by cosmic rays *atmospheric showers* or *particle cascades*.

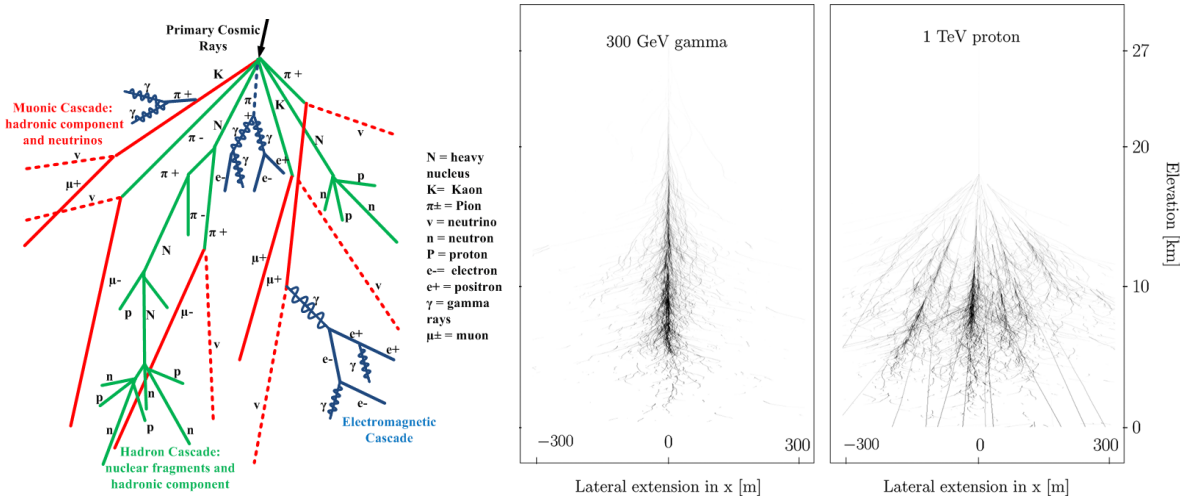


Figure 5: (Left) Representation of a atmospheric shower with its different possible parts, taken from [25]. (Right) Comparison of a MC simulated electromagnetic shower (from a 300 GeV  $\gamma$  ray) and a hadronic one (from a 1 TeV proton), the projection on a lateral plane is shown. The simulations were done using CORSIKA and are taken from [26].

Normally HE cosmic rays interact tens of km above the ground [27]. When one of these particles interacts, they can produce different outcomes, with most of the energy being transferred to new secondary particles, which in turn, are energetic enough to undergo further interactions. This process continues until the energy of the particles is reduced sufficiently, and ionization losses start to dominate, which leads to the extinction of the cascade. We can see in Fig.6 the number of particles that reach the ground for different initial energies following the Greisen semi-empirical model [28]. As expected for higher energies more particles reach the ground level, also if the observatory is at high altitudes more particles will reach the ground. For the case of the MAGIC and CTA-North site, Roque de Los Muchachos, is located at  $\sim 2200$  m altitude. For HE and part of the VHE range only few particles reach the ground. For the higher energies otherwise, the atmosphere is not enough deep to extinguish all the cascade. So we can differentiate between two cases [29]:

- *Sufficient particles reach the ground.* This is the case of VHE up to UHE gamma rays. In this case the detectors that will detect the gamma rays should be particle detectors, that can stop or track the particles using mechanisms such as scintillation or other diverse methods. The instruments used for detecting these energies are Surface Arrays (SAs) and Water Cherenkov Detectors (WCDs).

- *No particles reach ground.* This is the case of HE up to VHE range. In this case, the atmosphere acts as the calorimeter, and the high energy charged particles that are produced emit Cherenkov radiation. This radiation can be detected from the ground. In this case the IACTs will be used for this purpose.

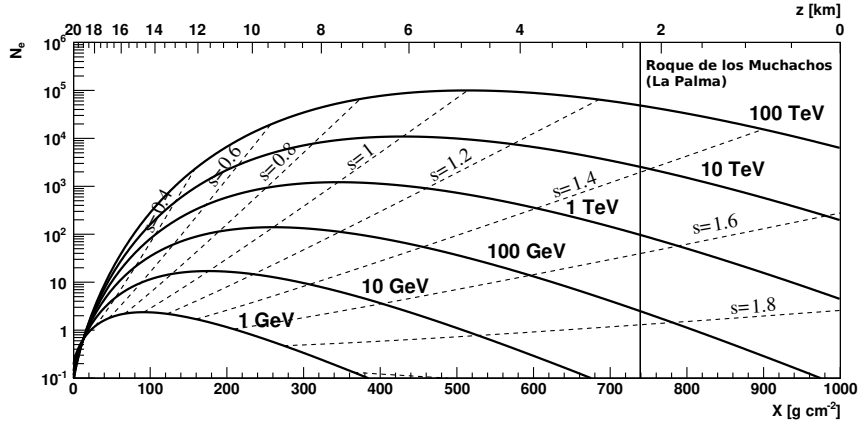


Figure 6: Number of particles reaching the ground as a function of altitude and radiation lengths. Solid lines represent curves of the same energy, and the dashed ones curves of equal age [27].

We can see from Monte Carlo (MC) simulations that are used in this work the geometrical distribution of cascades in Fig.7. We can see that the most energetic particles reach to deeper parts of the atmosphere. For low energies, in fact, the maximum number of particles occurs few km above than for  $E > \text{TeV}$ .

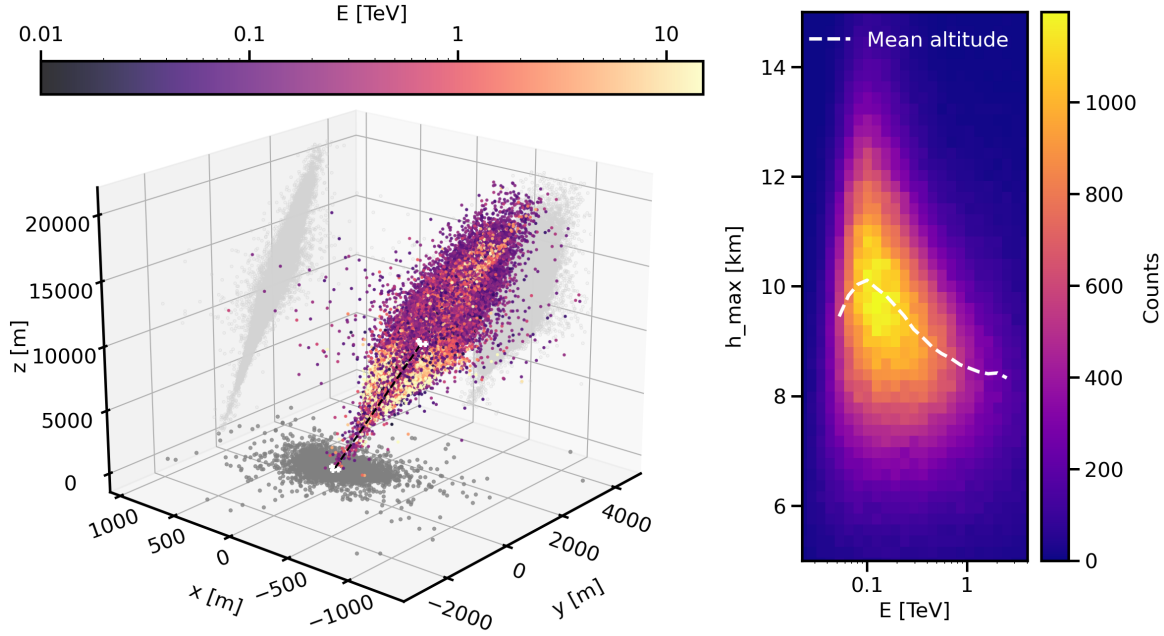


Figure 7: (Left) Geometrical representation of all events in a Monte Carlo MC simulation of gamma rays, where color represents the recovered energy of the primary particle. The dots represent the points in space where the reconstruction indicates a larger number of particles of the shower (the  $h_{\max}$  parameter). It can be observed that higher energy gamma rays produce lower  $h_{\max}$ , reaching deeper parts of the atmosphere. (Right) A histogram is shown for the same data as the left plot, showing the distribution of altitudes ( $h_{\max}$ ) in front of the energies. The mean altitude for each bin is shown with dotted lines.

### 2.2.1 Surface Arrays (SAs) and Water Cherenkov detectors (WCDs)

SAs and WCDs are the detectors responsible for detecting higher energy gamma rays, ranging from VHE to UHE, where the particles of the cascade reach the ground. Essentially they function as particle detectors. They are fixed arrays providing a field of view that covers the entire sky. For the case of SAs, they are composed of scintillation counters that detect the charged secondary particles passing by, and the trajectory can be inferred. Otherwise for the WCD water tanks are used as detector stations. The Cherenkov light emitted inside the tank can be measured, and the parameters inferred from that. Arrays of this type of detectors can be expanded relatively easily, and can cover large areas increasing the effective area easily. The two main detectors nowadays working are High Altitude Water Cherenkov (HAWC) [30] and Large High Altitude Air Shower Observatory (LHAASO)[16] (that now is almost finished).

Table 1: Main features comparison between IACTs and WCD and SA telescopes. The values will change depending on the instrument, but the general approximation is given. Adapted from [29].

	$E$ threshold	Duty cycle	Field of view	$E$ resolution	Angular resolution	Sensitivity
IACT	$\sim 10 - 100 \text{ GeV}$	$\sim 10\%$	a few msr	$\sim 15\%$	$\sim 0.1^\circ$	$\sim 1\% \text{Crab} / 25 \text{ h}$
SA/WCD	$\sim \text{TeV}$	$\sim 100\%$	$\sim \text{sr}$	$\sim 40\%$	$\sim 0.2^\circ$	$\sim 1\% \text{Crab} / \text{year}$

### 2.3 Cherenkov radiation

Before going into detail in the IACT techniques we can explain the main principle that is behind these telescopes, the *Cherenkov light*. It is a type of emission that occurs when a charged particle passes through a medium exceeding the speed of light in that medium [27]. This will happen when the medium is a dielectric, then the charged particle will induce a change in the disposition of dipoles (see Fig.8) emitting photons through all the trajectory of the particle. As the particle travels faster than light, the light spheres that are produced stack in a front forming a *light cone*.

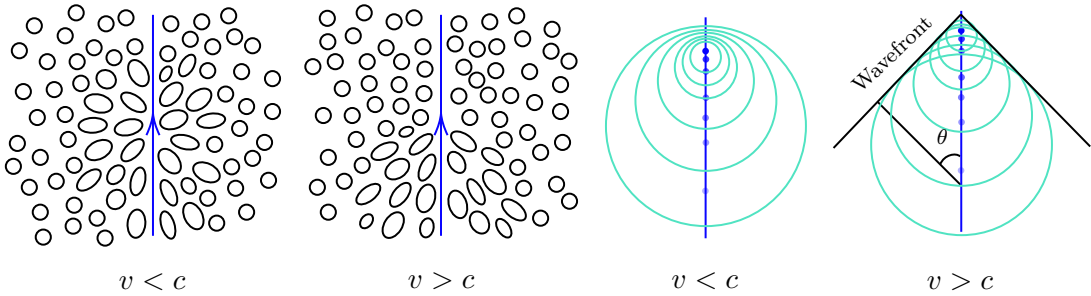


Figure 8: (Left) Scheme of induced polarization in a dielectric medium by a charge traveling at speed lower and greater than light. (Right) Diagram of Cherenkov light cone geometry in the case of traveling also slower and faster than light.

The angle that the front forms with the propagation direction will depend on the relative velocity of the particle with the speed of light  $\beta$ , and hence on the refractive index  $n$ ,

$$\cos \theta = \frac{c}{vn} = \frac{1}{\beta n} \quad ; \quad \beta = \frac{v}{c}. \quad (1)$$

For the case of individual particles, measuring the angle of the cone will give us estimation of the velocity. In our case for the IACTs, in general we are only seeing small fractions of the cone of light. So this geometric argument cannot be used to estimate directly the energy in our case.

From Eq.(1) we can see that there is a dependency on the angle and the velocity and energy of the particle. To put some numbers on this, we can show the energy required for some individual

particles to produce Cherenkov light in dry air at sea level [31]. For electrons the energy required is around  $\sim 20$  MeV, while for protons it is around  $\sim 40$  GeV and for muons  $\sim 5$  GeV.

About the general morphology of the gamma-rays showers, some characteristics can be highlighted [27]. Firstly the atmosphere density gradient make the Cherenkov emission angle change over the light path, going from approximately  $0.2^\circ$  to  $\sim 1.5^\circ$ . The difference in angle and height of emission produces an accumulation at around 150 m from the impact location (for the case of an observatory at  $\sim 2000$  m of altitude), the so-called *light annulus* Fig.9. Secondly, we also observe an effect of the arrival time of the photons at the detector, with the delay depending on the height of emission. As particles travel faster than light, Cherenkov radiation emitted at low altitude will arrive first, but otherwise showers at low altitudes with larger impact parameter will have a large geometrical path over atmosphere, making the light to arrive later (see Fig.9). For showers with a small impact parameter, the Cherenkov radiation emitted at low altitudes will arrive first. For showers with a large impact parameter, the first light to arrive is the one emitted at high altitudes. The two processes balance out at approximately  $\sim 120$  m (again for the case of an observatory at  $\sim 2000$  m of altitude), where the light emitted at all altitudes arrives to the detector at approximately the same time.

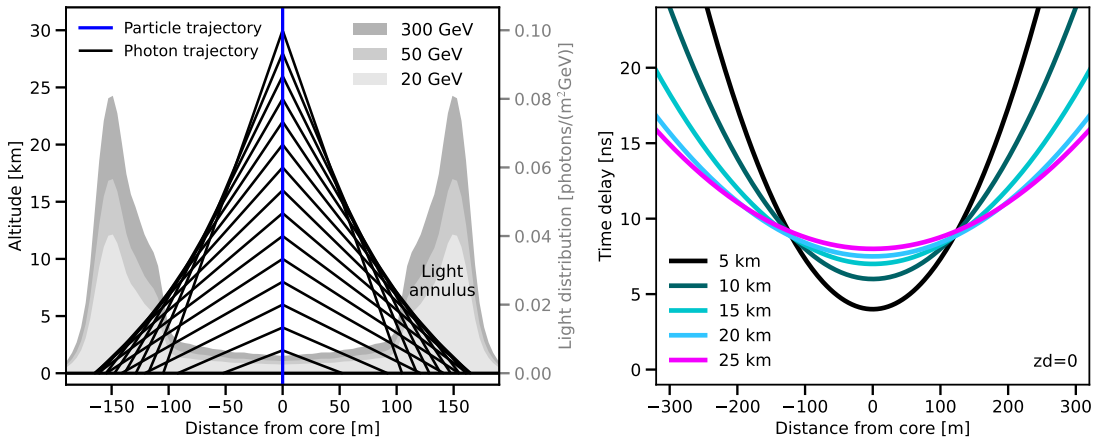


Figure 9: (Left) The paths of the charged particle and the paths of the Cherenkov photons for a perpendicularly falling particle. From a lateral view, it can be seen how the angle changes with the atmosphere density, concentrating light at the annulus. In addition to that, the scattering of the particles diffuses the distribution. (Right) The time delay for the arrival at the detector, for light emitted at different heights. Showing how the arrival time varies with the distance to the core i.e. the detector. The plots are adapted from [27].

### 2.3.1 Imaging Atmospheric Cherenkov Telescopes (IACTs)

The telescopes that detect the Cherenkov light emitted by the secondary particles before reaching the ground, are called IACTs. In order to detect the showers, they need to extinguish in the atmosphere, therefore, they cover the HE to VHE energy range. The shape and characteristics of light distributions can be very difficult to analyze. The interactions that take place in showers are ruled by stochastic processes, so simulations are required. The way to analyze the detection of showers is based on comparing the measures with the results of simulations using different techniques. In order to produce the simulations, a model of the physical processes need to be created. Normally MC simulations are the best option in these cases.

The simulations are performed for different types of particles, photons (gamma rays), protons, electrons and muons generally. Protons and in general cosmic rays, more irregular showers because of the hadronic interactions which may give raise to sub-showers at different angles (see

Fig.5). Otherwise photons interact mostly through pair production, which can be highly directional producing a more focused beam. Also we have muons, coming from cosmic ray interactions. Some muons will not interact easily with atmosphere so they generate a distinct Cherenkov cone. This last case have a distinguishable pattern, that can be discarded easily when the cosmic ray falls near the telescope i.e. when it has a low impact parameter.

IACTs may also detect cosmic particles, in fact, these are the vast majority of events that are detected. Cosmic rays are the main source of background noise in the search of gamma-ray signals. They are composed of a mirror dish that focuses the light and generates an image on a fast camera. The camera is usually composed of PhotoMultiplier Tubes (PMTs) detectors that amplify the electric signal and digitize it. The trigger mechanism prompts the acquisition and storage of data from all pixels whenever there is a rapid increase in intensity is detected in any group of nearby pixels. The time window corresponds to the typical duration of a Cherenkov flash, a few ns. As large mirror dishes are needed, in general, segmented mirrors are used. The main differences between the SA and WCD techniques can be summarized in Table 1.

The major IACTs that are operating nowadays are Very-High Energetic Radiation Imaging Telescope Array System (VERITAS) in the USA [32], High Energy Stereoscopic System (HESS) in Namibia [33], Major Atmospheric Gamma-ray Imaging Cherenkov (MAGIC) in Spain [34] and the Cherenkov Telescope Array (CTA) in Spain [15], under construction. We will focus our work on the ones at La Palma (Spain), MAGIC and CTA North, so we can perform stereo analysis using them. CTA will be the next-generation IACT observatory, it will be composed of an array in the northern hemisphere that is being built, and an array in the southern hemisphere, in Paranal, Chile. The north array is constituted nowadays on the prototype of Large Sized Telescopes (LST), LST-1, and 3 more LSTs will be available by early 2026. It will have also 9 Medium Size Telescopes (MST), that will cover the higher energy range of the spectrum. The CTA South will be composed of LSTs, MSTs and also Small Size Telescope (SST), and construction has not yet been started. A comparison between mirror sizes of the main existing and planned IACTs can be seen in the image Fig.10.

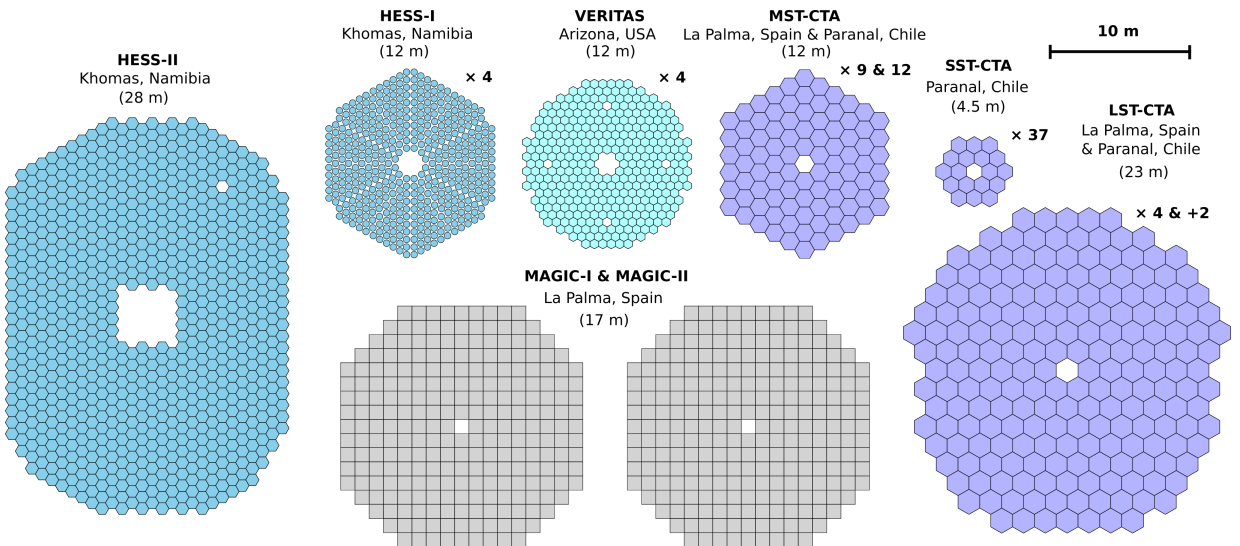


Figure 10: A scale representation of the most important Cherenkov telescopes in operation and planned. It is indicating how many of them there are on-site. In the case of the CTA collaboration, the ones in Chile are not yet installed, and at La Palma, there is only one LST, but the following three will be installed in the following years.

About the telescopes we are going to use in stereoscopic mode, MAGIC and LST-1, as LST-1 has a larger size will have more energy resolution against one MAGIC telescope, but the pair of MAGICs operating as a system will outperform LST-1, thanks to the stereoscopic reconstruction of the shower geometry. It therefore expected to achieve better energy and angular resolution. A comparison of the main features and characteristics of both instruments can be seen in Table 2. MAGIC is composed of two telescopes with a diameter of 17 m each, and LST-1 has a diameter of 23 m. All of them are located at Roque de Los Muchachos (La Palma, Spain), situated at 28°N, 18°W and at an altitude of  $\approx 2200$  m (see Fig.11).



Figure 11: On-site location at Roque de Los Muchachos (La Palma, Spain). View of all three telescopes from left to right: LST-1, MAGIC-2 and MAGIC-1. Taken from [35].

Table 2: Comparison between MAGIC and LST parameters. They both have parabolic dish and pixel Field of View (FoV) of 0.1°. Table adapted from [29].

	Diameter	Focal length	Camera FoV	# Pixels	Quantum efficiency	Sampling rate	Event rate
LST-1	23 m	28 m	4.5°	1855	41 %	1 GHz	7000 events s <sup>-1</sup>
MAGIC-1 & 2	17 m	17 m	3.5°	1039	34 %	1.64 GHz	300 events s <sup>-1</sup>

IACT analysis need simulations to study the morphology of the showers. In general MC simulations are used. The complexity of the problem and all the parameters make it the best option. MC techniques consist of simulating gamma rays or cosmic rays entering the atmosphere and being detected by the telescopes. The MC simulations are performed for photons, protons, electrons and muons. With this, the background contribution can be reduced more easily. In this work MCs are produced suing the tools **CORSIKA**, **sim\_telarray** [36].

- **CORSIKA** is used for the simulation of all the physical processes involved in the shower creation. Such as Earth magnetic fields, nuclear interactions, the electromagnetic radiation that is emitted such as Cherenkov radiation, the atmospheric conditions, the scattering and other variable parameters. Also there are also many other parameters of the incoming gamma ray or cosmic ray, such as the direction from which the particle is coming, energy, the type of particles and other parameters of the incoming primary ray.
- **sim\_telarray** package is used to simulate the interaction of the telescope with light and detection of the shower. It considers all the geometric aspects of the telescope and the interaction of light with it. It also simulates the amplification and digitalization of the signal in the detection mechanism, in our case, PMT tubes.

The MC files are used to "compare" the real images acquired by the telescopes with the MC ones, and based on this similarities, assign a direction and energy, and quantify how closely the event resembles a gamma ray or a hadron [37, 38]. To quantify this characteristic, the quantity known as *gammaness* is used, which is a number between 0 and 1 that tells how similar an event is to a gamma ray shower (*hadroness* is also used sometimes, and simply quantify similarity with an hadronic shower). The comparison of the MC files and the real data are done through Random Forests (RFs). A RF is a machine learning algorithm that basically uses subsets of data to generate a tree of binary "questions" and depending on the chosen branches, it will provide a result [38]. In IACTs, this is done to calculate the energy, direction and gammaness.

The use of more than one IACT will give a big advantage over having only one, the *stereoscopic analysis* [29, 39]. Observing the same part of the sky with more than one telescope allows for different reconstructions from each telescope. In the case of energy or gammaness, you can compare the values from each telescope. If all of them provide similar results, it is very likely that they are fairly accurate. The final values can be calculated as a weighted mean of the values from all the telescopes. In the case of the direction reconstruction, stereoscopic observation really make a big improvement. As can be seen in Fig.9, depending on the impact parameter, the first light that arrives the telescope can either be the first emitted or the last emitted. Reconstructing the shower in the opposite way would be a considerable source of error. Stereo observations allow for crosschecking the directions in each telescope, and the real direction will be near the point where all the directions should intersect. An sketch of how the stereoscopic technique is applied can be seen in Fig.12.

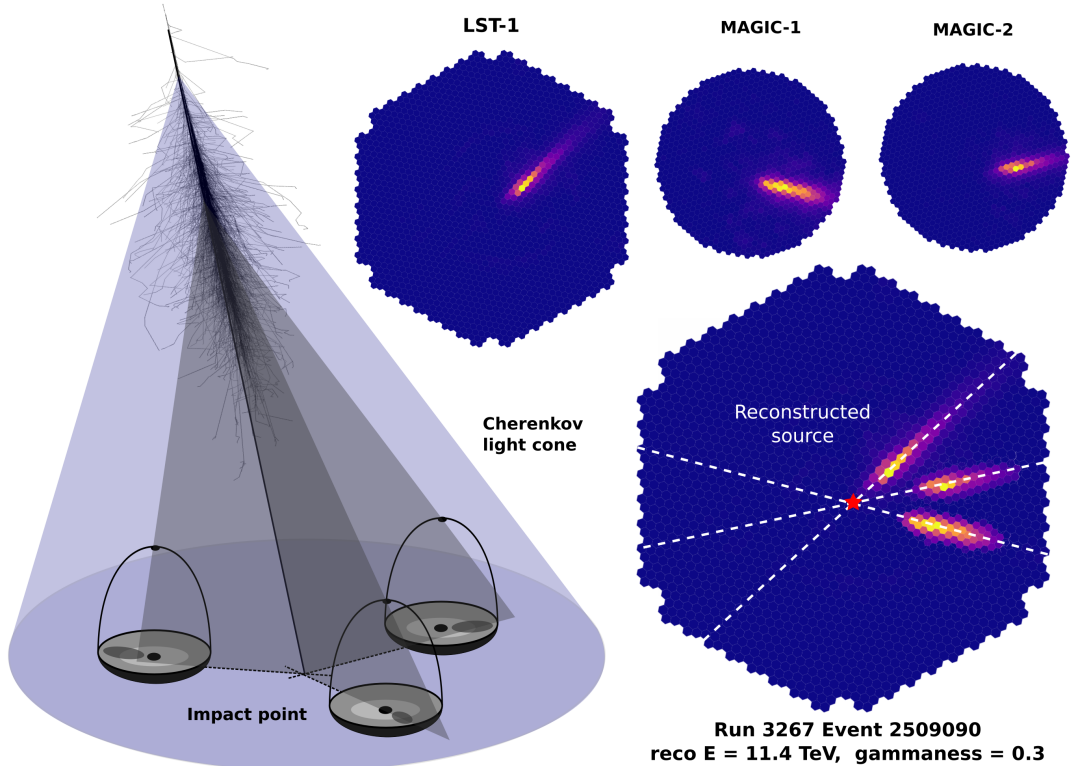


Figure 12: (Left) Sketch of the stereo reconstruction of atmospheric showers. The reconstructed direction is found intersecting the planes formed by the center of the camera, the mirror, and the direction of the image in the camera. (Right) Example of a real event (from 15 of December of 2020) detected by all three telescopes. The event in the camera geometry is found as the intersection of the different images.

The observation of determined sources follow a specific methodology. In contrast to other types of telescopes such as radio and optical telescopes, which usually directly point to the source they want to observe, IACTs do not directly point to it. Due to the fact that the IACT methodology consists of counting photons one by one, the background contribution has to be taken into account. A background region should also be studied, to "subtract" this contribution from the source region. The background region should be near the source but in a way that the source does not affect it. As the mirror dishes (in general) have spherical symmetry or are very close to it, the idea is based on observing the source (the *on-region*) and the background regions (*off-region*) at the same radius from the center of the camera. Multiple off-regions can be used to obtain different background samples. The tracking position will be adjusted over the night to change the background regions. This methodology is called the *wobble mode* [40]. A sketch of the main concepts can be seen in Fig.13. In this work, the standard LST wobble offset of  $0.4^\circ$  is used.

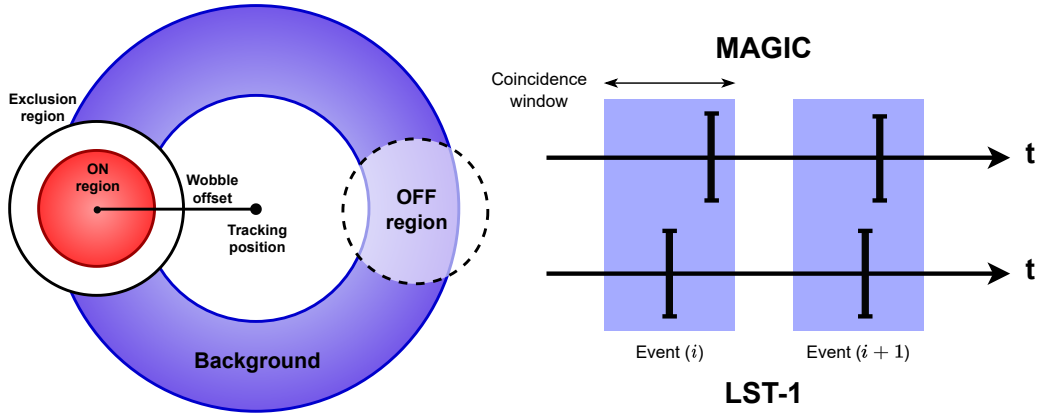


Figure 13: (Left) Geometrical definition of the different regions used in IACT imaging. The ON region represents the position of the source, and the tracking position the place where the telescope is pointing. A radial area (at the same distance as the source) from this center is defined as the background region. (Right) A sketch showing how the event coincidence is done using the different timestamps saved by each instrument.

Another challenge that IACTs face, when used in wobble mode, is the time calibration of the telescopes. Due to geometric reasons, Cherenkov flashes will not arrive at the same time at different telescopes. In fact, the telescopes are separated by approximately 100 m, which corresponds to a time delay of approximately 300 ns in terms of light travel time. These time differences remain relatively constant over short time periods. The event coincidence processing between telescopes is performed run by run. Here, a run refers to a continue observation period (of approximately 20 min for LST-1). Multiple time offsets are added to the timestamps of one of the telescopes and determine the appropriate time offset for that observation period. Once the time offset is determined, a coincidence window is used to perform the crosscheck, the linked events can be identified (see Fig.13). Events last for a few ns, and for example, the chosen coincidence window for this work is 300 ns. Which is smaller than the dead time of the PMTs, ensuring consistent event identification.

The analysis then is done these on and off regions. The  $\theta^2$  parameter can now be calculated for each zone. This parameter is simply the square of the angular distance between the direction of an event and the on-source or off-source regions. The nominal source coordinates are used as the on-source, and the off regions are chosen symmetrically around the center of the camera. We calculate  $\theta^2$  instead of  $\theta$  because the solid angle scales with the square. In the absence of any source we expect to have a more or less flat  $\theta^2$  distribution from the isotropic cosmic-ray

background. These parameters are important for the analysis and quantify the excess of events in the regions near the source.

### 3 Emission mechanisms and sources

Gamma ray astronomy is a relatively novel research field that has seen significant advances in recent decades. The development of advanced techniques and telescopes, has allowed the study of gamma-ray sources with unprecedented detail. The sources that produce VHE gamma rays are associated with acceleration of particles to relativistic energies. This is therefore associated to violent events in the universe as SuperNovas (SNs), relativistic jets etc. There are some types of sources that are well known, but there are sources where other wavelengths counterparts have not been observed and therefore we do not know what type of objects they are with exactitude. Also the tools we have nowadays add some limitations. There are still a lot of open questions in this topic.

Gamma rays can be produced here on Earth with nuclear disintegration processes of various species, that are able to generate gamma rays of few MeV. But if we want to explore the range of VHE, we will need to go outside Earth. Going out of Earth the next source of gamma rays is the sun, but as it generate them by nuclear reactions, it also add up to few MeV, so for the search of VHE gamma rays we need to go for extra-solar sources.

We can discard thermal emission in general because the temperatures related to VHE gamma rays through black body emission are around  $10^{10}$  K, which can only be achieved in the very most energetic events in the universe. The places where this thermal equilibrium is achieved require also very high pressures that at the same time do not allow the radiation to reach us. Then the source of energy of the gamma rays we observe should be related to non thermal processes.

#### 3.1 Gamma-ray emission mechanisms

The principal emission mechanisms are related to collisions between accelerated cosmic rays and a target; that can be from magnetic and electric fields (virtual photons), other particles to photons. The energy spectrum of the different emission mechanisms will have a dependency with the energy spectrum of the accelerated cosmic rays [41]. Usually, it is considered a power law with a certain power law index  $\alpha$ , i.e. the energy spectrum of cosmic rays follows the form  $\phi_e \propto E_e^{-\alpha}$  where  $E_e$  represents the cosmic ray energy. This is due to the consensus nowadays on the main possible mechanisms of cosmic ray acceleration, *Fermi acceleration* [42, 43]. This mechanism happens in SN shock regions, and is the main one that can account for the observed amount of cosmic rays, even though it has not been consistently verified yet. The main mechanisms are represented in Fig.14 and include the following:

- o *Bremsstrahlung* is the mechanism by which a charged particles passing close to an atomic nucleus, then the electric field bends the trajectory, causing acceleration and therefore radiation emission (see Fig.14) [41, 44]. The energy spectrum produced will be Black Body in lower energies, a flat spectrum in the optically thin region, and a exponential cutoff at high energies. Is more efficient for low mass particles i.e. electrons.
- o *Synchrotron radiation* is the process where a charged particle emits radiation when passes through a magnetic field and curve its trajectory by Lorentz force (see Fig.14) [41, 45]. It is a relativistic process, the non-relativistic analog is the *cyclotron*. It is emitted in the direction of the trajectory and it produces a spectrum of  $\sim E_\gamma^{-(\alpha+1)/2}$  with a  $\sim E_\gamma^{5/2}$  cutoff at low energies and a exponential one at large energies. The process is more efficient for particles of low mass.

- o *Curvature radiation* is similar to synchrotron radiation, but in this case, the acceleration is caused by the charged particle moving through a curved magnetic field, and then emitting radiation (see Fig.14) [41, 46]. In this case, the energy spectrum produced depend on different factors but can be approximated in some cases to  $\sim E_\gamma^{-(\alpha+1)/3}$ .
- o *Inverse Compton Scattering* is the mechanism by which energetic electrons transfer momentum to photons through Compton effect (see Fig.14) [47, 48].

$$e^- + \gamma_{\text{low}E} \rightarrow e^- + \gamma_{\text{vhe}}. \quad (2)$$

Depending on the energy of the photon before scattering the emission has two regimes [41]. If the photon has low energy (In the rest frame of the electron) interaction takes place in Thomson regime, otherwise the regime will be the so-called Klein-Nishina. The spectrum in this case depend on more factors, as the Lorentz factor of the particles or the optical depth, that determines the number of scatterings that could happen. The spectrum will depend as well on the photon field that is being scattered, as can be the Cosmic Microwave Background (CMB), light from stars, from synchrotron etc.

- o *Neutral pions decay*. This is the main process responsible for hadronic gamma-ray emission. It occurs when HE hadrons interact with other hadrons, the main candidates are those from the InterStellar Medium (ISM) (see Fig.14). This will produce three types of pions:  $\pi^+, \pi^-, \pi^0$ . Charged pions decay into muons and neutrinos, while neutral pions decay into photons [49],

$$p_{\text{vhe}} + p_{\text{ISM}} \rightarrow \pi^0, \pi^-, \pi^+ \dots \pi^0 \rightarrow 2\gamma. \quad (3)$$

This mechanism leaves a footprint of regions where protons are accelerated to ultrarelativistic energies, i.e. cosmic accelerators.

- o *Exotic processes*. There are theories that expect DM particles to produce gamma-ray emission when they annihilate [50]. This phenomenon has not been observed yet. If a VHE spectral line is detected, it could potentially be evidence of the presence of DM particles.

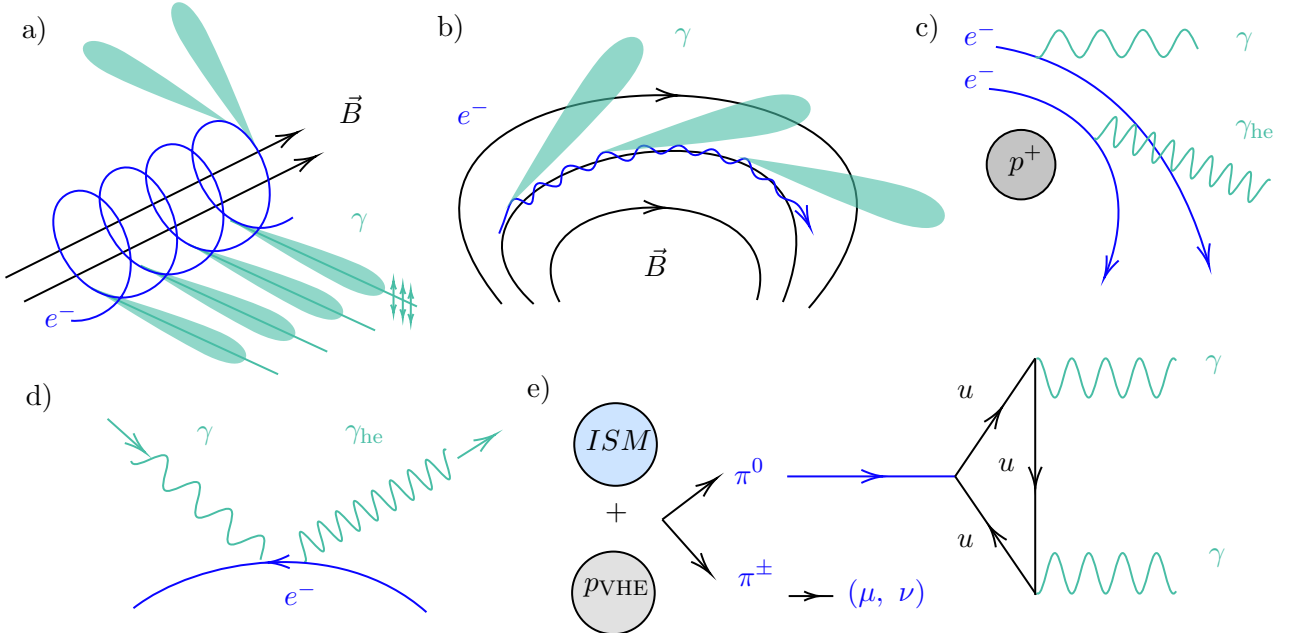


Figure 14: Main gamma ray emission mechanisms. a) Synchrotron radiation. b) Curvature radiation. c) Bremsstrahlung emission. d) Inverse Compton mechanism. e) Neutral pions decay emission.

### 3.2 Sources

There are multiple candidates for emitting gamma rays in the universe, but for those that are closer and better studied, we have a better understanding of their emission nature than those that are very far away us. The galactic sources that are well-known to us are basically *pulsars* and *supernova remnants*. We can see both galactic and extragalactic sources from Fermi data [14] in Fig.17.

- **Pulsars** are Neutron Stars (NSs) spinning at high velocities. NSs are one of the most compact objects we can observe and are formed with SN explosions. Their interiors exceed nuclear density, so the gravitational fields that generate nearby are very intense. If there is material around it can be accreted onto the NS and accelerated to relativistic speeds.

Material rotating around the NS gets accelerated and therefore, it can emit via curvature and synchrotron mechanisms. In addition, another process that dominates in pulsars is the Inverse Compton (IC) scattering. Some pulsars can have enormous jets that are detectable in multiple wavelengths and can accelerate particles to VHE, allowing them to emit gamma rays, see Fig.15. When large quantities of material are expelled due to the pulsar's rotation they can form the so-called *Pulsar Wind Nebula* (PWN). PWN can also emit through the interaction of their shock waves with the shock waves from the SN. This phenomenon extends much farther than the pulsar and does not exhibit periodic behavior.

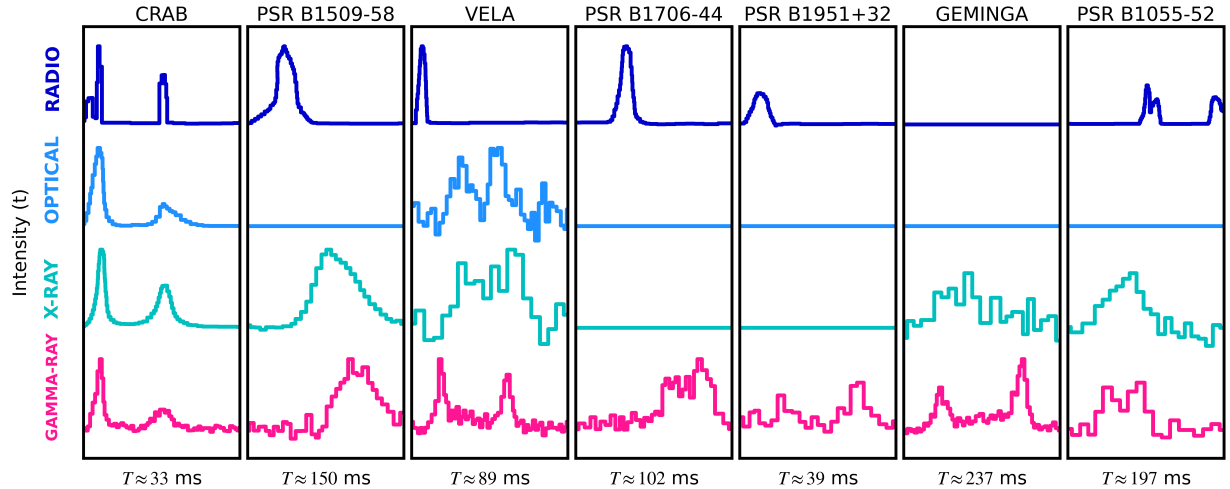


Figure 15: Multi wavelength observations of the pulse timing for seven of the most studied gamma-ray pulsars, with the period  $T$  also provided for each. Image adapted from [51].

- **Supernova remnants** are the vestiges of massive stars that could no longer resist the gravitational pressure and then exploded violently. This energetic ejection of material accelerates particles and can emit via most of the mechanisms listed above, depending also on the presence of magnetic fields.

This process is closely related with *pulsars* because SN can produce NSs when happen. Having two sources at the same time, the point source i.e. the pulsar, and a more extended source; the nebulae or SN remnant. This is the case, for example, of Crab Nebula and some others. SN that have not produced PWN but still have shock waves are called *shell-type* SN remnants. VHE emissions have been detected from the shock waves of this type of SN. An example with the SN1006, detected by HESS, can be seen in Fig.16.

- **X-ray binaries** are systems of two bodies where one is a compact object, either a NS or a Black Hole (BH), that is close enough to the companion to accrete matter. There are two ways where this happens, when stars are very massive and are at the end of their life, winds are ejected, which can form an accretion disk, and also if the star is close enough to the compact object, it can fill the Roche limit and start extracting material gravitationally. The formed disk can accelerate particles and usually emit in X-rays, but it has been detected some that also emit HE gamma rays [52].

After those we can start to search for sources also in extra-galactic sources, where we can find even more energetic events happening. So here we can differentiate between some different type of sources:

- **Active Galactic Nuclei (AGN)** are among the most powerful and energetic objects in the universe. They are Super Massive Black Holes (SMBH) at the center of galaxies that are powered by accretion. The ultrarelativistic jets some of them have are the main HE and VHE emission mechanisms for this sources.

A plausible explanation for the observed AGN types is the *AGN unification model*. The explanation for the different spectra observed in AGNs is provided by the observing angle of the source [53] (see Fig.16). We can see the isotropic distribution of AGN sources in Fig.17.

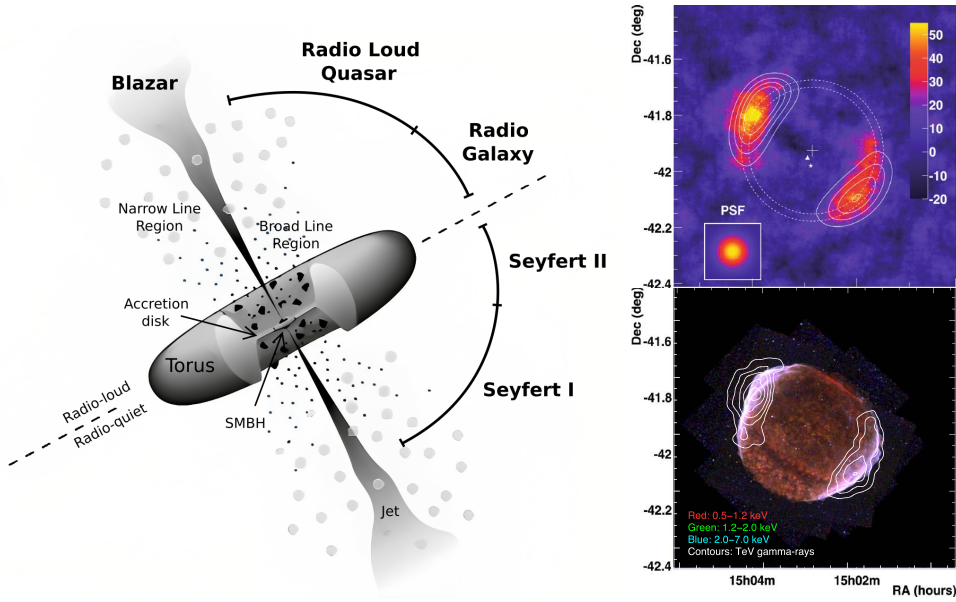


Figure 16: (Left) Unified model scheme of AGNs, and the different parts of the center of these galaxies shown, and the different type of galaxies that can be observed depending on the viewing angles. Adapted image from [53]. (Right) SN 1006, showing the gamma-ray detection with HESS and the resolved shell that emits VHE radiation, and the observations in other wavelengths, where the shell can be also distinguished. Adapted from [54, 55].

- **Blazars & BL Lac**, are specific AGN types that are well detected due to their high luminosities. In the unified AGN model [53], blazars correspond to the case when the jet is directly pointing towards us Fig.16. The jet emission typically produces a broad-band continuum emission ranging from radio to gamma wavelengths.

There are different classifications of blazars, but maybe the most important are *Optically Violently Variant blazars* and *BL Lac* objects, named after BL Lacertae, which are blazars characterized by a strong continuum and also strong variability. The vast majority of AGNs observed in HE or VHE are blazars (see Fig.17). Are very interesting sources because it can be detected from very far distances.

- **Starburst Galaxies** are galaxies where the Star Formation Rate is very high. Consequently massive stars are created at fast rate, leading to luminosity dominated by these young stars. Moreover, as massive stars have very short life, SN occur frequently, creating an optimal environment to generate gamma rays.
- **Gamma-Ray Bursts (GRBs)** are the most energetic events known in our universe. They emit an enormous amount of energy, approximately  $\sim 1 \times 10^{54}$  erg in a very short timescale. To compare with the energy released by the sun in one second. The classification of GRBs is mainly based on their duration [41]; if the duration is shorter than 2 s, they are called short GRBs; otherwise, they are called long GRBs.

Short GRBs are related to mergers of compact objects as these events happen in same timescales. This was demonstrated with the observation of gamma-ray emission counterpart of a gravitational wave event [56]. On the other hand, long GRBs are associated to SN created by the death of very massive stars. In both cases a BH is formed and a highly energetic jet forms. If the jet is pointing toward us we are able to detect the GRB.

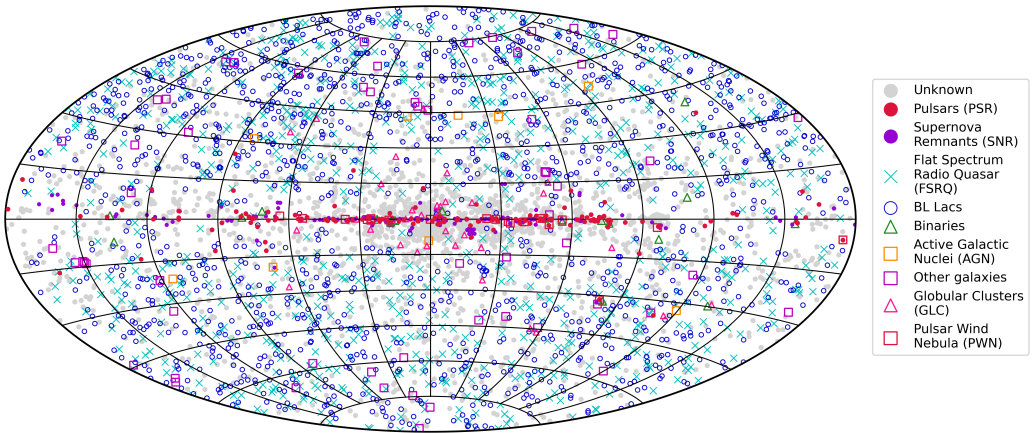


Figure 17: High-energy gamma-ray sources of different types are plotted in galactic coordinates, where the size corresponds to the flux. The data is taken from the fourth data release of the Fermi telescope of 2020 [14].

### 3.3 Crab Nebula

In this work we will focus our study in the Crab Nebula. Studying the Crab Nebula during the initial stages of stereo MAGIC + LST-1 analysis is of particular interest. Crab Nebula is one of the most studied sources, not just in gamma rays, so we have a lot of documentation to compare and validate our results (see Fig.18). The Crab Nebula has been used as a standard source in gamma-ray astronomy because of its high flux levels and the fact that the Crab Pulsar is a point source of gamma rays [57]. Furthermore, the flux is particularly stable in the VHE range, specifically within the IC regime i.e. energies greater than  $\sim 100$  GeV. Therefore, the Crab flux is often used as a standard unit of measurement, where 1 C.U. is equal to the flux observed from

the Crab Nebula [57].

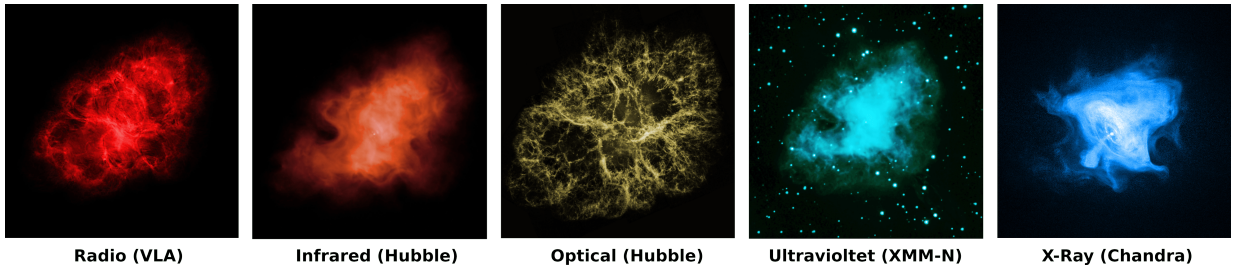


Figure 18: Different wavelength observations of the Crab Nebula. Different emission zones can be resolved for each type of radiation. The data were extracted and adapted from [58].

Crab Nebula and the respective associated compact object, is the remnant of supernova SN 1054 observed by Chinese astronomers, and being relatively young, it still emits intense radiation. It emits in all wavelengths, and the intensity of gamma rays is particularly high (compared to other objects). An example of the multi-wavelength emission can be seen in the phaseograms of the pulsar, in Fig.15. It is composed by a nebula, and the compact object that resulted from the SN explosion, the Crab Pulsar. It is a pulsar with  $\approx 33$  ms period, so this feature is something that also makes Crab an interesting source.

## 4 Data analysis pipeline

### 4.1 Data levels

In the LST analysis pipeline, there are different data levels that can be used for different purposes. As the data stored initially is very large, it needs to be reduced. The processing takes place at the on-site LST-1 computing cluster, also known as the *IT cluster*. All the computation performed in this work was done at this data center.

For the data taking, in addition to cosmic events LST is also constantly (at a rate of 100 Hz) taking data of pedestals, i.e. events that consist only of noise, and events triggered by a flasher that produces a uniform signal over the entire camera, known as flat-field events (with the same rate). This type of events are taken for calibration purposes, and are labeled by the Data Acquisition System. The rest of events triggered by showers are called *cosmics*. The analysis of the LST-1 is done using the LST tools i.e. `lstchain` [59].

Data is collected in events, in which the camera is triggered by detecting a light intensity above a threshold in any zone of the camera. When the camera is triggered it saves 40 frames, one per ns, referred to as the *waveform*. The camera splits the PMT signals and processes them in two separate branches with different amplification: high gain and low gain. Two different gains serve to augment the dynamic range. The signal is digitized with 12-bit resolution. Counts reaching  $2^{12}$  will saturate the signal, so the lower gain branch is added for these cases.

Two waveforms (one per gain) of 40 ns are stored per pixel. There are 1855 pixels in the case of LST-1. Approximately 150 000 numbers need to be saved per event. Taking into account that  $\sim 7000$  events are detected per second, in single run lasting approximately 20 min, the total weight of one run is usually around 900 GB. The purpose of the data levels structure is to compress the information and reduce the size of the files. In order of their application, this is the description of the data levels (see the sketch in Fig.19).

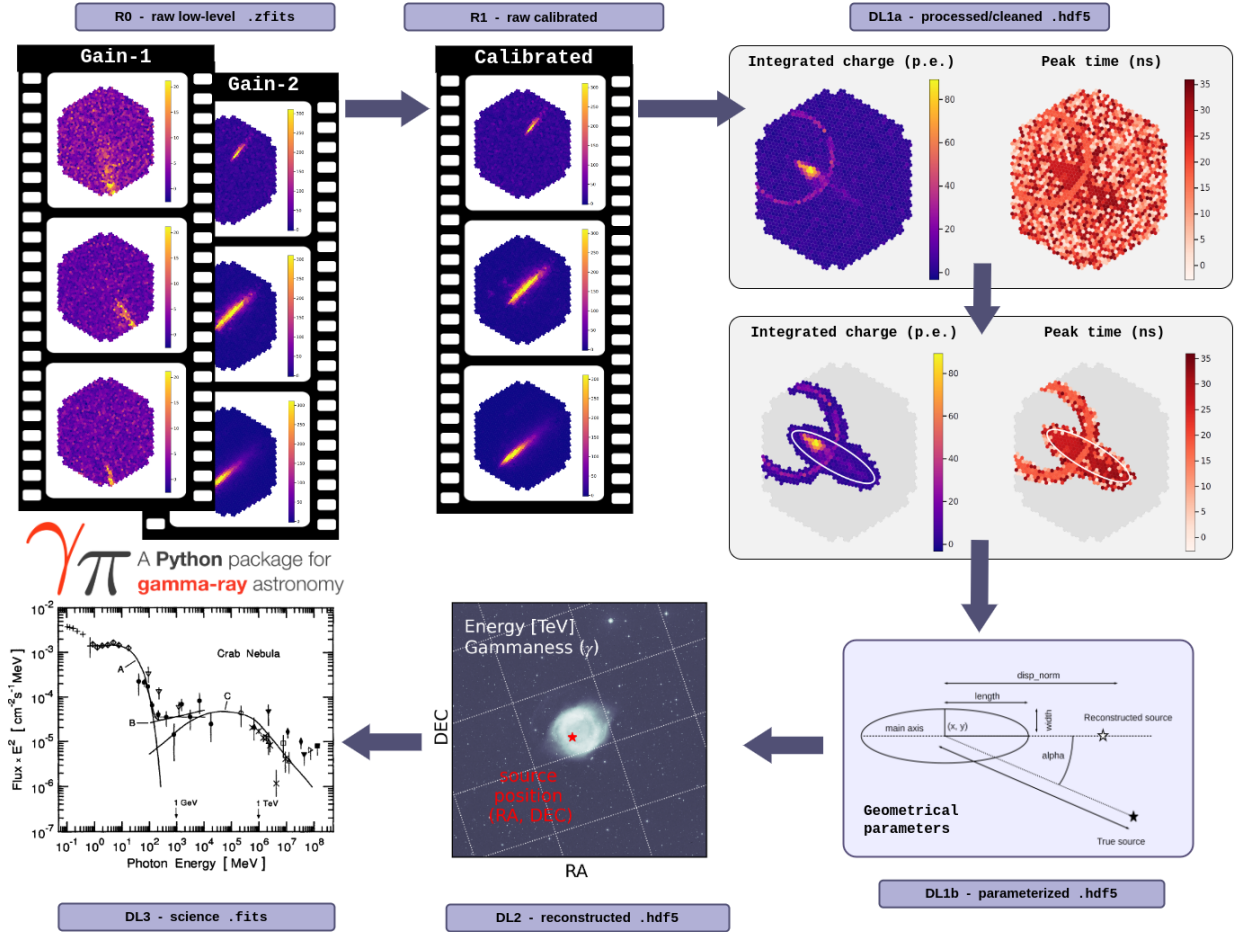


Figure 19: Sketch of the LST-1 analysis pipeline, the different data types and their corresponding file extensions in the same order that are produced.

- **R0 or raw low-level data**, this level is the lowest one, where the data is stored as the camera detects it. At this level, all waveforms for both gains are stored without any data being discarded. Keeping such data is unfeasible, especially when there will be 4 LSTs, so this will change in the future. This data level is saved directly into the IT cluster, in **.zfits** format [60].
- **R1 or raw calibrated data** This data level is not saved and is only used in-memory during the analysis pipeline. At this step, low-level corrections are applied to correct for peculiarities of the data acquisition electronics. Then, data of both gains is reduced to one calibrated waveform per pixel per event, which gives approximately 75 000 numbers per event.
- **DL1 or processed data**, is the level where the highest reduction of data is performed, going from having 40-frame movies of events to having few parameters that characterize the image. There are two sub-levels:
  - **DL1a**, is the level where, for each pixel, the charge is integrated over 8 ns (8 frames), this integrated charge and the peak time for each pixel are stored. A cleaning is also performed, where an algorithm identifies the pixels that are most likely to have detected Cherenkov flashes.
  - **DL1b**, is the final stage of DL1. In this level, the image of integrated charges is parameterized, using among other parameters the moments up to third order of the

charge distribution. We end up with a few tens of numbers per event, which will be saved in `.hdf5` format.

The conversion from R0 to DL1 is done using the `1stchain` pipeline [59]. In this work, for LST-1 we use the DL1 standard files (produced by the on-site analysis). For MAGIC, as we will use LST tools to perform the analysis, we will start from calibrated events images and obtain the DL1 files in the same format as those used for LST.

- **DL2 or reconstructed data** is the level where we obtain the most relevant parameters for each event in a scientific sense. The reconstructed energy, direction and the so-called *gammaness* for each event, which is a score (from 0 to 1) based on how closely the image resembles one produced by a gamma ray initiated shower.

To perform this step more information is needed, RFs are used to calculate all these quantities. MC simulations are used to build three RFs; for the energy, direction and gammaness (How these RFs are produced will be explained later).

- **DL3 or science data** is the level that we want to end up with for the scientific purposes of the study. Event lists of gamma-ray candidates containing the main reconstructed quantities, and an associated set of Instrument Response Functions (IRF) which allow to obtain higher-level scientific data (like energy spectra or light curves). The analysis from DL3 onwards is done using *Gammapy* [61, 3] that is a standard tool used in HE gamma ray astronomy, based in Python. The file format used at this point will be `.fits`, the standard format in astronomy [62].

In our work as said we will do every step using LST tools. Other aspect that we will study here is the comparison of the results obtained with the analysis of MAGIC data using `magiccta-pipe` and with the standard MAGIC analysis, called `MARS` [63]. For the case of MAGIC the DL2 data is called *melibea* calibrated level. In this case, the file format is `.root` [64]. This data is stored in the IT cluster and is the one that we will use to start our stereo analysis. We expect to find similar results using both pipelines.

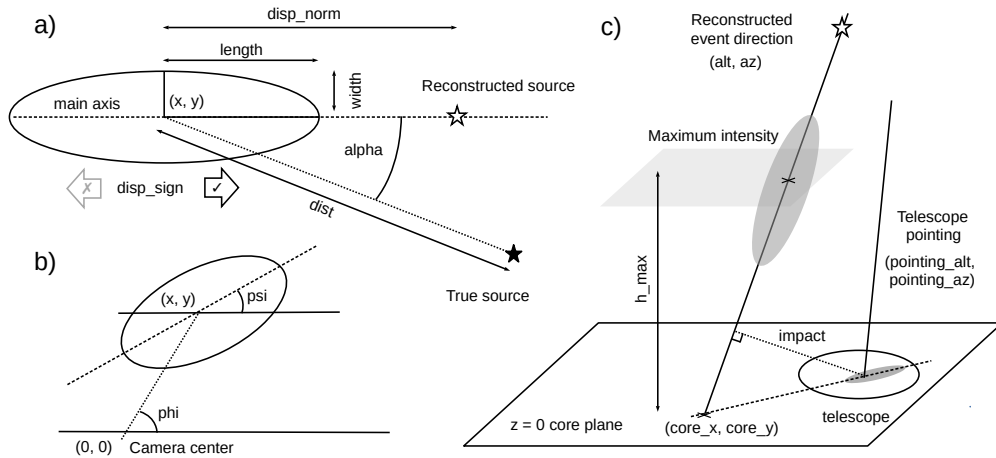


Figure 20: Most of the parameters that are given in DL2 files, schematized. In (a) we can see some parameters of the image and the reconstructed event direction. In (b) the parameters describing the position and orientation are shown. Finally in (c), the parameters related with the shower itself. Adapted and extended from [65].

Among some of the parameters that are saved in the DL2 stage there is the geometrical parametrization of the ellipse. Described with the centroid position ( $x$ ,  $y$ ), minor and major semiaxis, width and length (the second order moments), and the angles formed with the main axis;  $\psi$  (see Fig.20).

For the parameters related to the location of the source for example we have the reconstructed direction `alt`; the altitude and `az`; the azimuth. It can be converted to Equatorial Coordinates `ra` and `dec`. The `impact` parameter, that is the distance of the shower axis to each telescope, and the height of maximum shower development, called `h_max` (estimated from centroid positions in different cameras).

As the data in the lower levels is usually quite heavy, the files are often fragmented into smaller parts. In general for each observation night, the data is taken by runs, where each run usually corresponds to an observation time of about 20 min. Data is fragmented in subruns, which contain up to 53 000 events. The typical size of the subrun files is of 6.8 GB.

## 4.2 Monte Carlo (MC) simulations and Random Forests (RFs)

For the generation of the MC files, a grid of telescope pointings is created. Simulations are done for each point of the grid in horizontal coordinates (`alt`, `az`) (see Fig.21). Furthermore, all these simulations are performed for different levels of Night Sky Background (NSB) light. MCs are produced with a base level of NSB that corresponds to a dark field (extragalactic). Then, Poissonian noise is added to simulate observations with higher NSB. The assigned values to the NSBs represent the amount of noise added to the MC simulations as fractions of the minimum standard background simulated. To perform the analysis, the MC simulation that is closest to the observed field in terms of pointing and NSB level should be used.

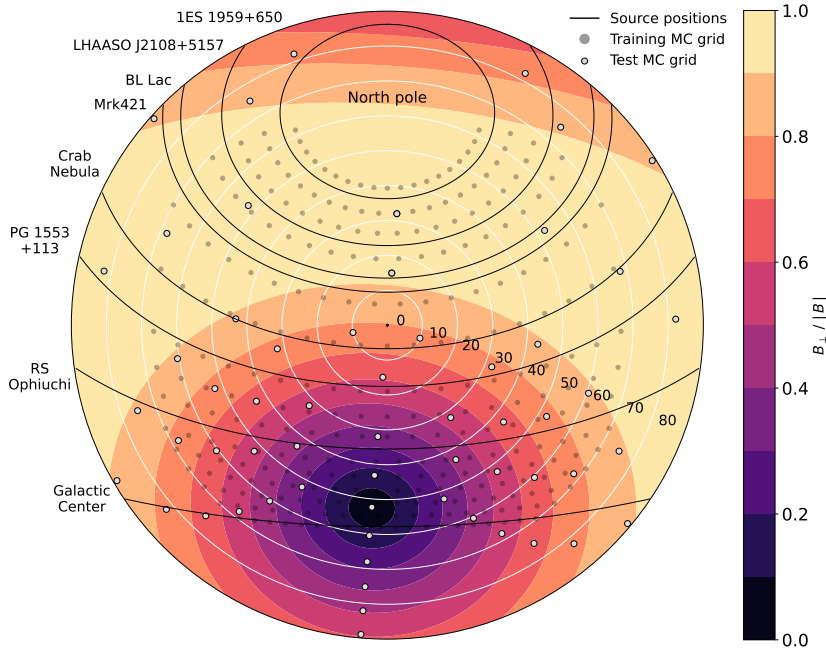


Figure 21: Sky map for Roque de Los Muchachos (La Palma) observations in horizontal coordinates (`alt`, `az`). Showing the MC simulations grid of pointings of the MC simulations that have been produced. The center of the plot corresponds to the zenith, and each white circle to a given zenith distance. Black lines represent the positions of some sources of interest throughout any day of the year (day and night).

The selection should be done taking into account the stars or the presence of the moon, among others. In our case, the Crab Nebula is a galactic source, but since it is in the opposite direction of the galactic center, the NSB level is moderate. For the analysis of the Crab Nebula, we use MC with an additional Poissonian noise of 1.5 p.e. per pixel. As explained before in our case the MC simulations are done using `CORSIKA` and `sim_telarray` [36].

RFs are algorithms that handle a large number of conditions and summarize them in a set of binary decision trees. They are constructed using a dedicated set of MC simulations (all pointings along one of the declination lines in Fig.21). In our case, they are constructed using MC simulations, for which the real target values (e.g. the direction or energy of a given gamma-ray event) are known. This is therefore a "labeled" set, and therefore the method is a supervised machine-learning approach. For the case of RFs, the selected one to analyze a run will be a linear interpolation of the closest RFs to the observed field in terms of pointing and NSB levels.

In the case of the stereo analysis the RFs are produced for each parameter we want to infer; direction, energy and gammaness. Additionally we have different RFs for each combination of the three telescopes (MAGIC-1, MAGIC-2 and LST-1). Each combination contains the stereo information of the three or two telescopes, as well as the image parameters for each telescope. For each one, a RF for all different telescopes is needed. The gammaness RFs are constructed using gamma-ray and proton MCs, in order to separate them properly. However, for energy and direction, only gamma-ray MCs are needed. The MCs described are the training MC, the ones used to optimize and calibrate the RFs. There are other type of MC that are used, the *test MCs*, that are used to test the model's performance. Training MC simulations are used to train a model, while test MC simulations are used to assess the model's performance on specific observations.

### 4.3 Stereo data taking

Stereo observations with MAGIC 1 & 2 and LST-1 consist on simultaneous observations of the same parts of the sky with all three telescopes. It can potentially provide a better performance than the one achieved by any of the instruments separately. It has been done since November 2019. Stereo analysis was also used during a period where one of the MAGIC telescopes was unavailable due to a malfunction. In our case, we are interested in studying the Crab Nebula, which is the standard candle of VHE gamma rays. The stereo data has been taken from various sources, we can see the most observed sources in the totality of the observations in Table 3. Also the fraction of data from before spring 2023 is shown. We can see the totality of sources that have been observed in the period the data is available in Fig.22.

Table 3: Main sources that have been observed in stereo mode with MAGIC and LST. The effective observation time is significantly reduced from the real time of observation, due to the application of coincidence windows (same wobble time) and compatible pointing. The time that is given in the table is already the effective time. Due to a malfunction in one of the MAGIC not all data is available right now (it needs to be processed in a different way), so the available fraction is represented (data from before spring 2023).

Source	Crab Nebula	BL Lac	Mrk 501	Mrk 421	Galactic center	M87
Effective obs time [h]	50.32	31.34	27.83	23.00	23.77	14.58
Available fraction	33.34 %	12.64 %	77.59 %	42.92 %	59.17 %	67.87 %

The date convention must be taken into account for Stereo analysis. Observations are conducted at night and span across two consecutive days. MAGIC takes the reference for the file names based on the day when the observations end, while LST-1 has the convention of the day when the observation starts. The different sources observed during the entire period from 2020

to 2022 can be seen in Fig.22.

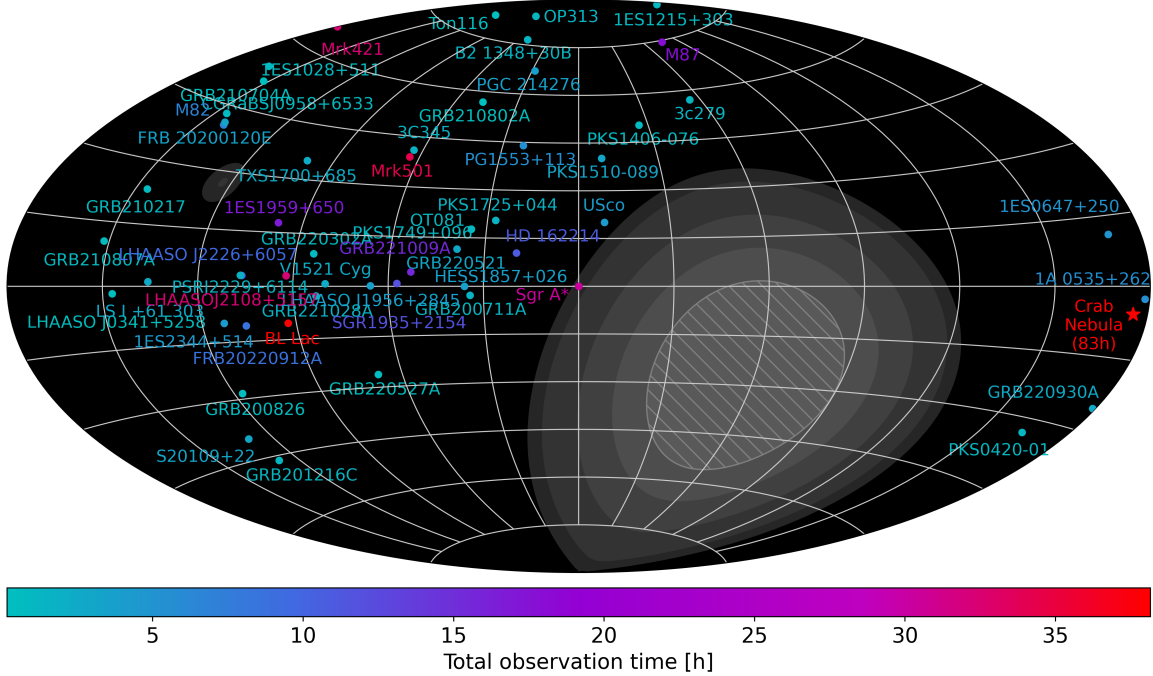


Figure 22: Distribution of the different observed sources in stereo mode by MAGIC and LST-1 in the period of 2021-2022, shown in galactic coordinates. The lighter areas indicate limited sensitivity due to the the observatory location in Earth while the dashed area indicates the sky region that is always under the horizon throughout the year.

For stereo analysis, a specific pipeline has been developed which is based on `1stchain` and `ctapipe`, called `magic-cta-pipe` [1]. This pipeline will primarily be used for the stereoscopic analysis and is currently under constant development. Therefore, in this work, we will also analyze the operation and performance of this software.

## 4.4 Implementation

In order to optimize and automate the processing, a GitHub repository was prepared, it uses the latest version of `magic-cta-pipe` (version 0.3.0) [2]. Given different run numbers for LST and MAGIC, the scripts produce the respective DL3 files. The set of scripts uses Python to perform all the steps individually, and Bash to send the jobs to the IT cluster queues. The processing is divided in different jobs to ensure reasonable processing time. Each job converts one DL1 run DL1 into DL2 stereo and then into DL3, which is the final stage. A flowchart with all the steps involved in the processing can be seen in Fig.23.

The stereo analysis starts in the DL1 level, with all the images of all three telescopes parameterized. In the case of LST the standard DL1 files are already available at the IT cluster. For MAGIC on the other hand, only the calibrated files (equivalent to the DL1a level) are stored in the IT cluster. The step to convert these calibrated files to the DL1b MAGIC files should also be done (cleaning and parameterization). In order to do it we will use `magic-cta-pipe`; an utility called `magic_calib_to_dl1`. So at this point we have for each telescope a set of DL1 files, organized by runs and subruns ( see Fig.23). As the data has been reduced, we can apply a merging between subruns to obtain a single file per run. The merging of .hdf5 files will be done with the `magic-cta-pipe` utility, `merge_hdf_files`.

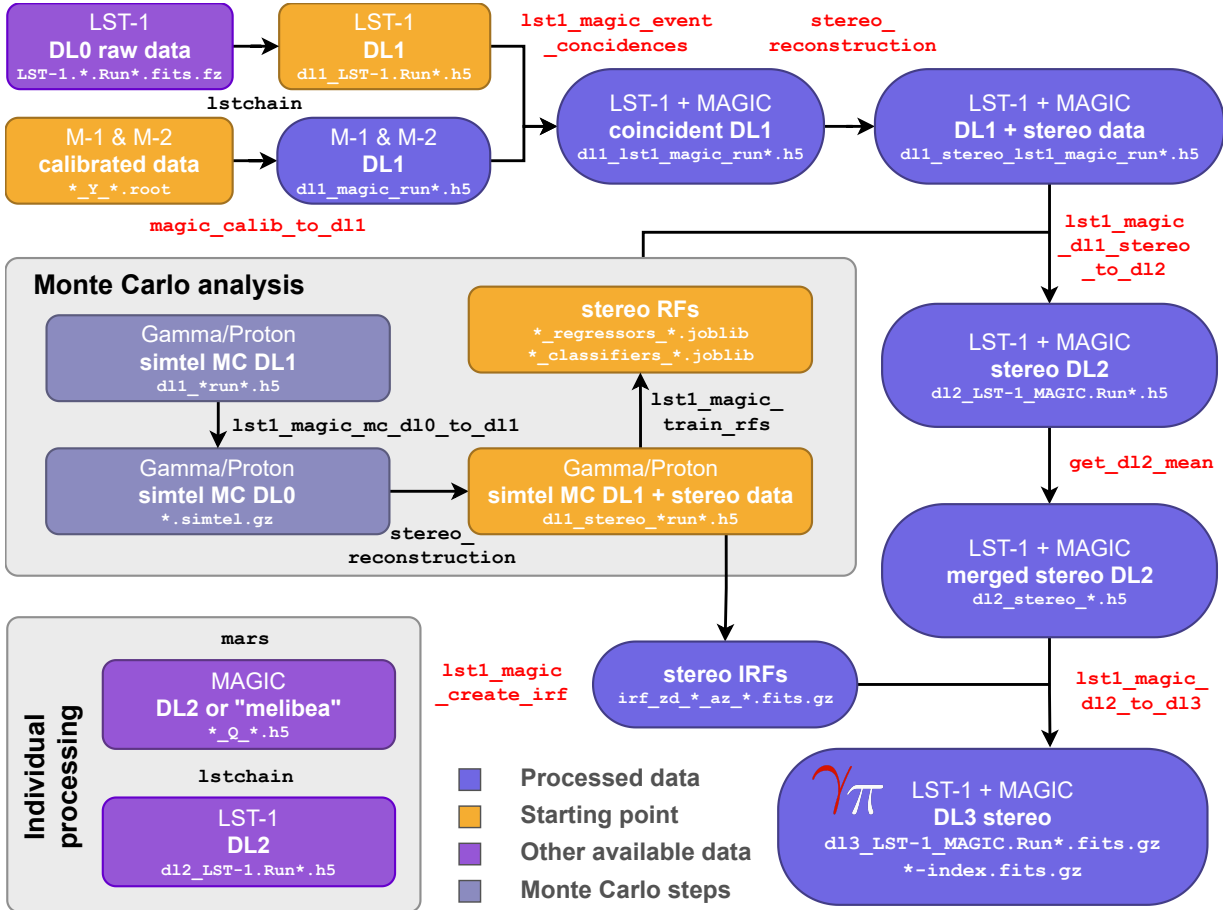


Figure 23: Flowchart showing all the steps performed in this work. The names of the tools used for each step are specified. We also indicate the data produced in this work and the data that has been already produced.

Now, when we have all the data of MAGIC and LST in DL1 format, we want to convert it to DL2. First of all, as we want to do the joint analysis, we need to search for the coincident events between the different observations, and discard events that are detected only in one of the telescopes. LST-1 has a higher rate, as seen in Table 1, and a larger effective area. Therefore, in general, LST-1 will observe most of the events detected in MAGIC. This is the reason why coincidence finding is performed by comparing each LST run with all the MAGIC runs. This process can potentially take a long time, as it involves checking different time offsets (see Fig.13). To optimise the computation we will sample the time offset in steps of  $0.1 \mu\text{s}$  from 0 to  $10 \mu\text{s}$ . The time offsets are applied to the event timestamps, and by applying a coincidence window, the events can be correlated. This step is performed using the `event_coincidence` function from `magic-cta-pipe`. The additional information produced in this processing, such as the statistics of events detected by each telescope or the offsets found, is also stored. A summary of the telescope groups that have detected different events can be seen in Table 4.

Table 4: Different event types in the stereo DL2 files and the respective percentages of the total amount of data.

Combination type	M-1+M-2	LST-1+M-1	LST-1+M-2	LST-1+M-1+M-2
Percentage of total	17.7 %	6.8 %	16.7 %	58.8 %

Afterwards, the stereo reconstruction of events is performed using `stereo_reconstruction`, which utilizes the stereo information and the individual images in DL1 format (see Fig. 12).

Quality cuts are applied to discard events with potentially poor reconstructions, events with intensity less than 80 p.e. are discarded. Then the stereo parameters are calculated. The output of this step is provided in subruns, which can later be merged into a single file per run in the final DL1 stereo format.

After we have the final DL1 file, we need to convert it to DL2, i.e. reconstructing the main parameters we are interested in. This is done using `lst1_magic_dl1_stereo_to_dl2`, that needs the RFs to reconstruct the parameters. These RFs has been already produced at IT cluster. After this we end up with one DL2 file for each run, and the information of each telescope is also preserved in the files.

As we are observing specific sources, in this last step, the calculation of the  $\theta^2$  parameter (defined in section 2.3.1) was added for the source. We calculate it for each event direction using as reference direction the nominal source coordinates (on-source), and also a control region (off-source), which contains no gamma sources (see Fig.13). In this work, 5 off-regions have been used in general. The reason for this is that, as explained later, 5 off-regions are defined as the standard for certain parameter calculations. The off-source zones are taken symmetrically with respect to the camera center.

To finalize the processing of DL2 data, we utilize the `get_dl2_mean` tool to merge the parameters calculated by each RF (for each telescope respectively). With that we can obtain a unique value for the energy, gammaness, and direction. Additionally, in this step, the reconstructed direction of each event is converted into equatorial coordinates (RA, DEC). The merging can be accomplished by three different ways:

- *No weights*, simply the mean value of three telescopes.
- *Intensity weight*, the mean weighted by the intensities.
- *Variance weight*, the mean of each parameter (direction, energy, and gammaness) will be calculated weighted by the variance of the RF output for each of the telescopes. This method will be the one that we will use for this work because it is in principle the one which takes best into account the uncertainty of the RFs outputs.

Finally, we have the DL2 files for each run. To proceed to the last step, DL3, we will need the IRFs. To obtain them, we will utilize the `lst1_magic_create_irf` tool. We input the corresponding MC files (already available on the IT cluster) and obtain the corresponding IRFs. We will have different IRFs for the various pointing directions of the telescope, namely azimuth and zenith distance. Since the last step is performed on a run-by-run basis, the IRFs will be *interpolated*. For each run, we select the closest IRFs based on zenith distance, azimuth and NSB. The IRFs are taken form the test MC grid (see Fig.21), that is not the same MC as the one used to construct the RFs. Subsequently, an interpolation (linear in our case) is performed. The interpolation is done over cosine of zenith distance angle. The transformation to DL3 is achieved using `lst1_magic_dl2_to_dl3` and `create_dl3_index_files`. The latter is employed to generate index files that store general information about all the data.

## 5 Data sample

Now we are going to discuss the data that have been selected and the data that finally will be used for the DL3 final analysis. It's worth noting that all data from November 2020 to March 2022 as we said have been analyzed. The process was done using the previously described pipeline [2] without discriminating any data. Once we have processed the data at least up to DL2 we can

apply certain selection criteria to discard bad quality data. First of all, a summary of the Crab Nebula distributions of dates and timestamps for the runs taken can be seen in Fig.24. The total amount of effective time available is 10.7 h over 55 LST-1 runs.

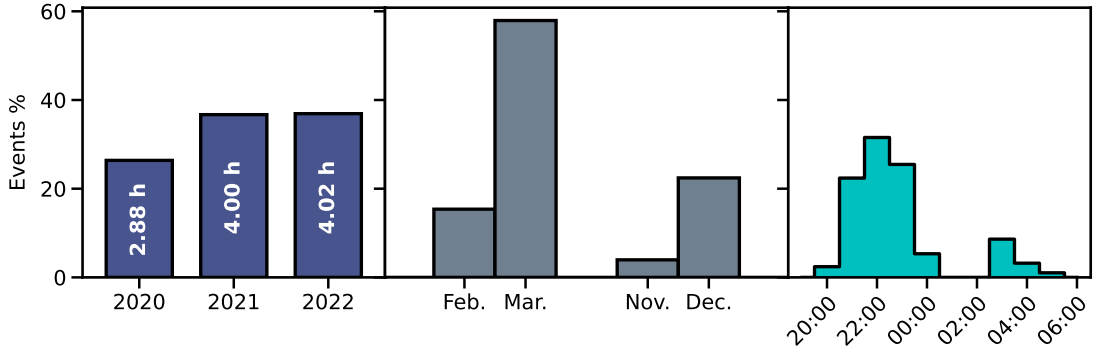


Figure 24: Distribution of all the Crab Nebula data across the years, months, and observation hours (from left to right). The percentage of events captured in each period is shown. The effective time for each year is also displayed.

We need to take into account that a volcano eruption occurred in La Palma in 2021. The event happened from 19 September to 13 December of 2021. During the eruption no data were taken due to reduced visibility produced by airborne particles, and also to prevent some elements from being damaged by the ash. That resulted in a gap in the observations. Because of that, the data can be grouped into 2020-2021 (pre-eruption) and 2022 (post-eruption). This is something important to consider because as reported in [65], LST-1 experienced a diminished reflectivity after the eruption. Although no damage was noticed in any of the telescopes as a result of the eruption, the long period of inactivity may have produced changes in the performance (e.g. from accumulation of dirt on the mirrors) so we decided to consider the two periods of data, pre and post-eruption, separately. 63 % of the data was taken before the eruption (see Fig.24). If we take a look at the month distribution in Fig.24 we can see that all runs were taken in winter. That is simply because the Crab Nebula is only observable during the night in winter.

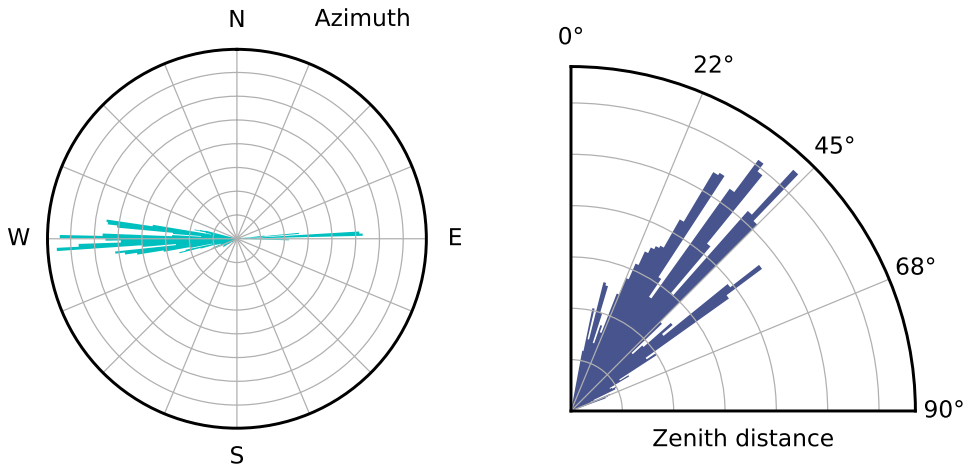


Figure 25: The zenith distance and azimuth distributions of the entire dataset we constructed. The weights are determined by the number of events, not by the number of runs.

Almost 50 runs have been processed, and each will cover different regions of azimuth and zenith during the observations. In general data with small zenith distances is preferred because the showers develop closer to the telescopes, the Cherenkov light density is higher, and hence the

energy threshold of the instrument is lower. We can observe the zenith distance distribution in Fig.25, the majority of the 3-telescope observations are at intermediate zenith angles. Regarding the azimuth distribution shown in Fig.25, the observations were mainly directed towards the east and west, with a significantly larger number of observations towards the west. This is basically due to the fact that the declination of the Crab is close to the latitude of La Palma, so the source culminates at a zenith distance of less than  $7^\circ$  (see Fig.21).

When checking the output information from the event coincidence step we can find the pointing information through events from each run. We have this information for LST-1 and both MAGICs. We computed the angular distance between two pointing directions ( $\text{az}_i, \text{zd}_i$ ) obtaining the distributions seen in Fig.26. We can distinguish two regions, the first one corresponding to the data from 2020 and 2021 that have very small pointing differences. Another regime with larger differences between LST-1 and MAGIC, corresponding to 2022 data. The first one has a mean difference in pointing of  $4 \times 10^{-3}$  deg, and the latter has  $13.9 \times 10^{-3}$  deg. On the other hand the pointing difference between MAGICs is much lower over the entire period, with a mean value of  $2.7 \times 10^{-3}$  deg. In general the differences are very low, all of them below  $0.05^\circ$ , so no data need to be removed for this reason.

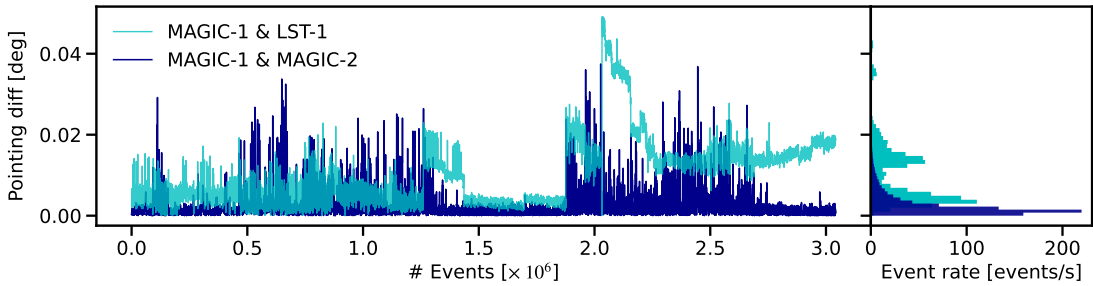


Figure 26: Pointing difference between LST-1 with MAGIC-1 as well as between the two MAGICs across all events in the entire dataset. On the right, we can see the respective histograms of these distributions.

Furthermore, when examining this data from the coincidence finding, the time offsets found for each event are stored (see Fig.27). The time offset refers to the difference in the timestamps stored by each instrument for the same events. We can see in Fig.27 that there are two distinct regimes. The first one corresponding to the data from 2020 and 2021, that peaks around  $-2.96 \mu\text{s}$ , and the second peaks around  $-5.92 \mu\text{s}$ , almost twice as large, corresponding to the data from 2022. There is a significant difference between the two, and the exact reason for this difference is unknown.

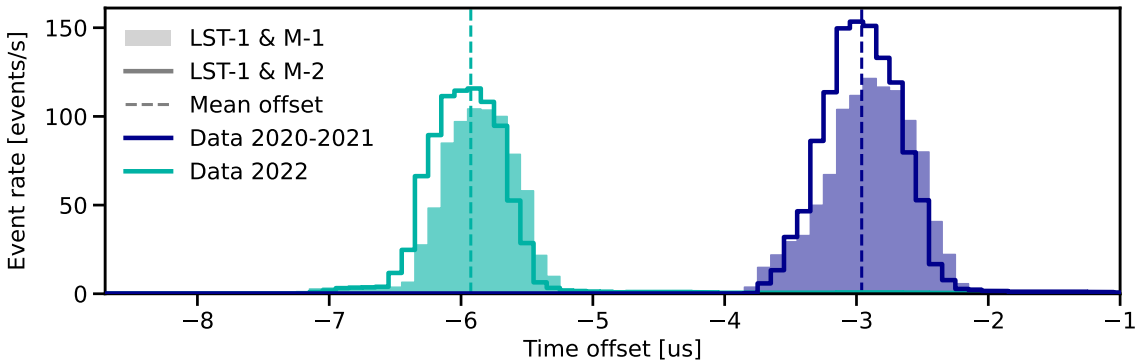


Figure 27: The distribution of time offsets observed between MAGIC-1,2 and LST-1 data. The two main periods are shown separately. The mean offset value is also represented for LST-1 and MAGIC-2.

For MAGIC telescopes there was a decrease in the optical efficiency between these periods. Usually different MC productions are performed for different observation periods depending on parameters such as the telescope’s light collection efficiency. The MC simulations for this period after the volcano eruption have not been yet produced for the analysis of stereo MAGIC and LST-1. Therefore in this work the MC files from before the eruption will be used, MC files labeled as M2.03.18. This may introduce a slight bias in the parameter reconstruction for the second part of the data sample. We will perform various checks in order to see how it affects the whole analysis.

Atmospheric conditions also affect the performance of the telescopes. In La Palma it is common to experience *calima*, which is the presence of dust from the Sahara desert suspended in the air, that complicates the observation. Additionally, there will always be cloudy days that interfere in the data collection. The conditions for each observation can be checked in the commissioning log, where information of dust density, cloud cover, transmission, temperatures, etc., can be found. These environmental conditions affect the event rate captured by the telescope. During unfavorable conditions the event rates can drop from normal numbers i.e.  $\sim 6$  kHz to 3 kHz. These conditions can significantly impact the analysis by decreasing the observed flux introducing biases into our data.

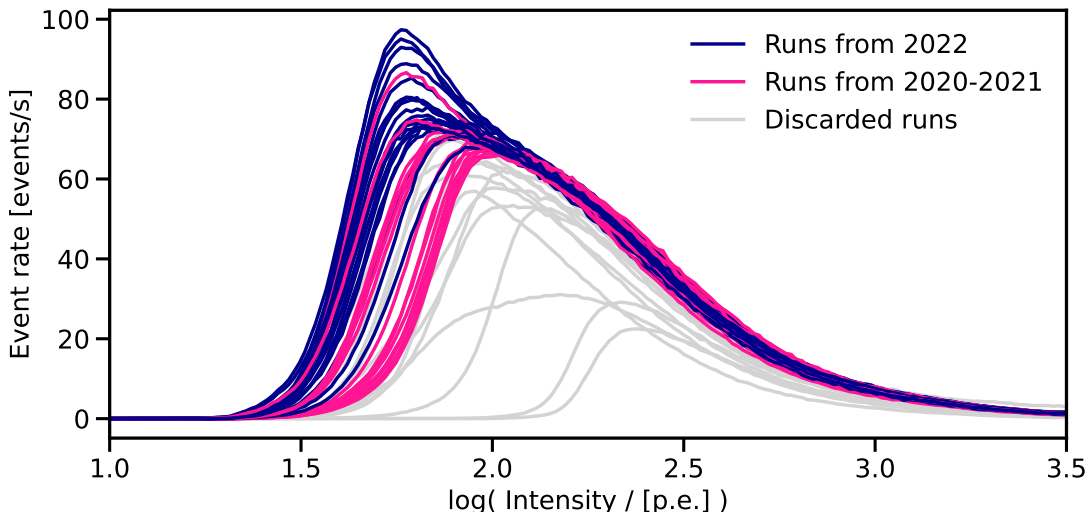


Figure 28: Distributions of the logarithm of image intensities distributions for different runs. The runs from 2020 to 2021 and those from 2022 are represented separately. The discarded runs are shown in gray and most of them (10 out of 11) correspond to the group of runs from 2020 to 2021, which are observed to be more unstable, specially in the low-intensity regime. LST-1 has an automatic rate control system which modifies the trigger thresholds depending on the NSB conditions. In August 2021 the settings of the system were revised, resulting in significantly lower and more stable threshold of the telescope.

A way to apply a filter is to discard data with low intensity images in the regions near the telescope threshold. These variations are not present in the MC simulations, so a systematic error will be produced [65]. The rate of shower images of a given intensity should not change much between runs, if the telescope performs in a stable way (there is some small dependence with zenith, but we can ignore it here since we just want to remove clear outliers). The intensity distributions of all runs are shown in Fig.28. The rates in the lower intensity region vary a lot, this is not a problem because the reconstruction of low-intensity events, which occupy very few pixels in the camera, is generally worse than in the high-intensity region. Also as we are applying a intensity filter of 80 p.e. this unstable region is discarded completely. Also, this variation is due to changes that have been applied to the trigger settings over time. The rates for the bulk of

the runs are quite similar for intensities larger than 100 p.e.. The filtering will be applied in this region. We will only keep the runs that are close to each other in the mentioned region. There is also a dependency with the zenith distance [65], but the impact will be almost negligible, and the cut we are applying is not so strong, so the effect will be minimal. No dependencies on zenith distance are considered.

We filtered the runs and selected the colored ones shown in Fig.28. We revised the runs in order to find what could be wrong in these runs. We searched at the commissioning log, and also crosschecked with the weather station of Roque de Los Muchachos. It was confirmed that the runs with different rates generally correspond to days with lower data-taking rates, primarily due to high dust concentration (runs with  $\sim 30 \mu\text{g m}^{-3}$ , whereas the typical optimal values are around  $1 \mu\text{g m}^{-3}$ ). After discarding these runs, we went from 55 LST-1 runs to 44, reducing the effective time by approximately one hour (most of the discarded presented lower detection rates).

## 5.1 Other sources

In this work we have focused on the study of the Crab Nebula. This source is the standard candle in HE and VHE and the high flux allows us to obtain enough photon statistics in a reduced time. As in this case we need data from joint observations with LST-1 and MAGIC, that were not fully coordinated during the commissioning period of LST-1, the statistics are limited. If we add to this the fact that there were some technical problems which have made the analysis of the data difficult, it is one of the few sources that for the moment can be analyzed in detail.

The next good candidates to be analyzed in stereoscopic mode are among the most observed sources (see Fig.22 and Table 3). We selected BL Lac and Mrk421, both extragalactic objects, AGNs and of the BL Lac class (named after the first object BL Lacertae). The first one was chosen because observations were taken during a flare state in summer 2021 (see the timeline of observations in <https://astronomerstelegram.org/?read=14783> [66]). BL Lac achieved a flux  $\sim 5 \text{ C.U.}$ , which presents an excellent opportunity to collect a lot of statistics in a short time. However, while these observations happened, in the most active days of the flare, specifically for 8 of August 2021, there was an error in the timestamps of one MAGIC, so the procedure to find the coincident to find the events cannot be done as usual. It has been found by the MAGIC+LST-1 working group of CTA that this time error changed during time, which further complicates the analysis. The specific data of these observations needed a much more specific and tedious treatment. The BL Lac data which did not have this problem were analyzed following the described pipeline (see Fig.23). But unfortunately the runs that do not present this timestamp error do not coincide with the high activity days of the flare. Not enough statistics were obtained to compute a energy spectrum.

For the case of Mrk421, it is also a AGN with high gamma-ray flux [67] and it is as well one of the most observed sources in stereo mode. We tried to analyze the  $\sim 35$  LST-1 runs that were taken but we also found some problems. The same problem presented for BL Lac has affected the Mrk421 observation. Also in this case some of the observations were taken only with LST-1 and MAGIC-2 due to a malfunction in MAGIC-1 that needed repair. This fraction of the data will not be completely useful for our purposes: understanding how the 3-telescope reconstruction improves the performance of the analysis, as in this case, where we would be working with only two telescopes. Even though we performed the analysis for the available data of Mrk421 and just as it has happened with BL Lac, the statistics are not enough to compute a spectra or a light curve without having huge uncertainties. For these reasons, this work has been focused on the analysis of the Crab Nebula, source for which we have enough data and with no technical problems.

## 6 Checks of the DL2 data

Without entering in much detail on the final results that this work aims to obtain, the intermediate processed data can also be analyzed to provide an evaluation of the performance of the software `magic-cta-pipe` that is at a very early stage of development. The data can be compared with the other individual instruments, LST-1 analysis with `1stchain` [59] and stereo MAGIC with `mars` [63]. Before going into detail with the IRFs or the characterization of the instrument, we will analyze some reconstructed parameters of the data obtained in DL1 and DL2 stages.

As we said Crab Nebula is the standard candle in VHE gamma-ray astronomy, and is the source from which we have the most statistics, and has been observed the most in stereo mode. Because of its stability in this range of energies ( $\sim 0.1$  TeV – 10 TeV), it will be the source used for the characterization of the instrument and the stereo reconstruction. We will make three basic types of comparisons:

- *MC comparison.* The comparison of the true and reconstructed parameters obtained for MC data. In this case we know the real parameters values.
- *Instrument comparison,* where we will compare the results of different telescope combinations; the 3 telescope stereo, the LST-1-only analysis (done using `1stchain`) and the stereo MAGIC analysis (done using `mars`).
- *3-Tel stereo; telescopes comparison.* We will observe the differences in the calculated parameters for each telescope, all analyzed using the same software, `magic-cta-pipe`.

In order to make these comparisons fair for each of the telescopes we will keep only the events that have triggered all three telescopes, and then we can see what the effect that have another telescope working with MAGIC. Then, a unique dataset containing all the data is created with a total of 2979 565 events, this will be the dataset used for most of the DL2 analysis.

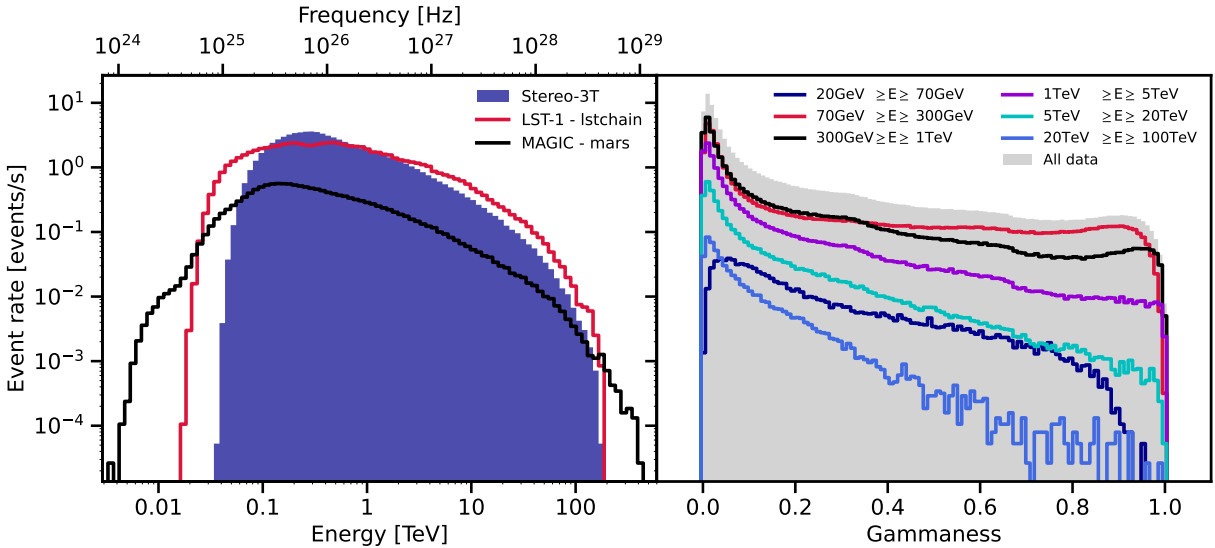


Figure 29: (Left) The reconstructed energy distributions for the different instruments. For the case of LST-1 and 3-tel stereo representing the same events. For the case of MAGIC alone, the events shown are the ones where the energy was successfully reconstructed (remaining data after standard quality cuts 30 %). (Right) The total gammaness distribution in gray, and the energy binned gammaness contributions as color lines. The left part of the distributions is mostly populated by cosmic rays, while gamma rays will tend to concentrate on the right part.

## 6.1 Energy and gammaness reconstruction

As we said IACTs operate in the VHE range, approximately around 1 TeV. We can see the energy distributions for the different instruments in Fig.29, and indeed the distribution peaks near 300 GeV, spanning a few orders of magnitude. We can also observe from the gammaness distributions in Fig.29 that the low gammaness population is the most dominant, i.e. the vast majority of detected events are cosmic rays rather than gamma rays. We calculated the gammaness distributions for 6 logarithmic bins with a size of 0.45 in logarithmic scale, and starting from 200 GeV up to 100 TeV. The gammaness distributions within different energy ranges show different distributions. The peak at low gammaness decreases for higher energies because at higher energies distinguish showers is easier.

Once we have calculated the energies of each event and applied a reasonable gammaness cut (which removes most of the background events) we can start comparing the data event by event. The gammaness cuts will be discussed in more detail later. For now on we can simply apply a strong cut that discards most of the cosmic rays. In our case, a cut of  $\text{gammaness} > 0.95$  give us enough statistics for the comparisons. It represents a very strong cut, as we are keeping only 0.6 % of the events. We can compare the data in two different ways:

- *Independent analysis methods.* Comparing the data of this work, i.e. the 3-telescope stereo analysis with the same specific events analyzed with other methods. For LST-1 standalone analysis, using `lstchain` and for MAGIC standalone analysis using `mars` (see Fig.30).
- *Telescope wise reconstruction using `magic-cta-pipe`.* Using only 3-tel stereo reconstruction (`magic-cta-pipe`), comparing the different telescopes. As for each telescope a individual RF reconstruct the parameters independently and then a mean over telescopes is done, the values in each telescope can be compared (for the case of MAGIC-1 and 2, see Fig.31).

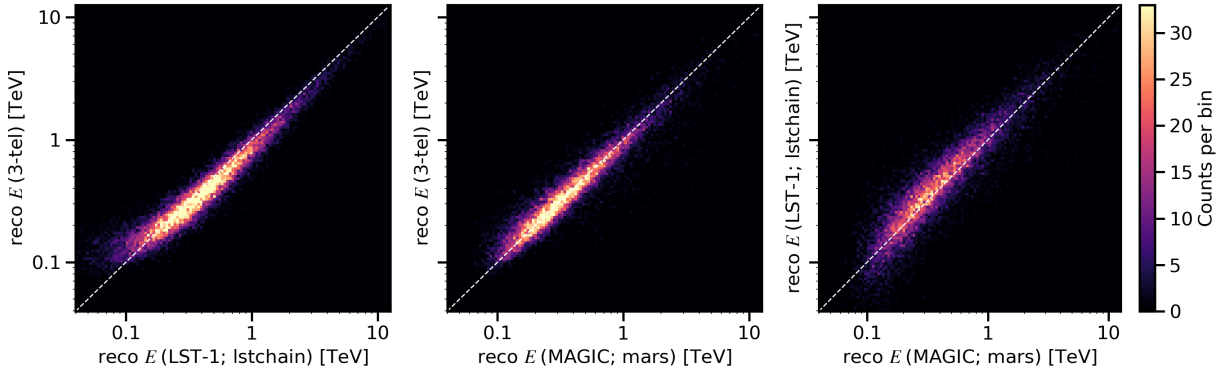


Figure 30: Reconstructed energies of the different methods (3-tel stereo, LST-1 alone, and MAGIC alone) represented as pairs, event by event. The displayed white lines represent the ideal energy reconstruction i.e. reconstructing the same values of energies. All possible comparisons are shown.

In both comparisons (Fig.30, Fig.31) it can be observed that some instruments and methods overestimate/underestimate the energy, as their distributions are slightly shifted away from the 1 to 1 reconstruction. To quantify this, we can compute the energy ratios between different methods as  $\text{ratio}_{i,j} = E_i/E_j$ . In ideal cases, the ratio should be close to 1. All energy ratios are represented in Fig.32 and also for different periods in Fig.31.

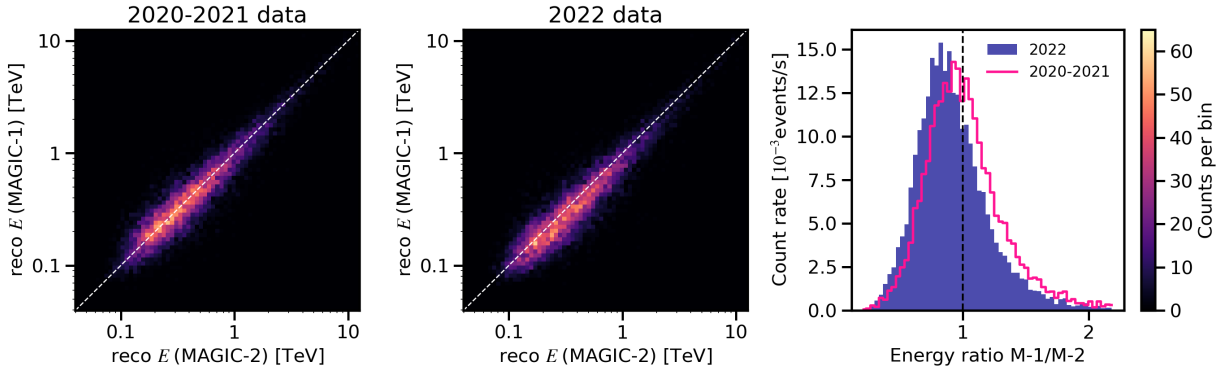


Figure 31: Comparison of reconstructed energies for MAGIC-1 and MAGIC-2 using `magic-cta-pipe`. The data is obtained with the independent image of each telescope given by the respective RF but also using the stereo common information. Data has been separated in periods in order to see the performance of the used MC files over the different periods.

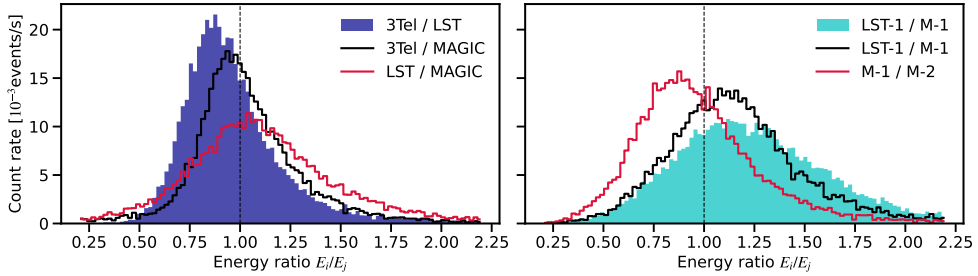


Figure 32: Summary of energy comparisons shown in Fig.30 (on the right) and Fig.31 (on the left). The energy ratios for the different methods and telescopes are shown. A shift to the right or left of 1 indicate an overestimation or underestimation in one or the other direction.

First we can look at the results between the different methodologies in Fig.30 and 32. It can be observed that 3-tel stereo generally reconstructs energies near those reconstructed by LST-1 (`l1tchain`) or MAGIC (`mars`). Regarding LST-1 (`l1tchain`) and MAGIC (`mars`), they recover similar energies but the LST-1 reconstructs slightly higher energies. Examining the median values of the energy ratios, it can be seen that energy reconstructed by 3-tel stereo is 7.8% lower than that recovered by LST-1 alone, and 4% lower than that recovered by MAGIC alone. The distribution between MAGIC and LST-1 standalone is more spread, but based on the medians, we can conclude that MAGIC reconstruct in average 2% lower than LST-1 alone.

The comparison of the recovered energies by different telescopes only using `magic-cta-pipe` is shown in Fig.31 and Fig.32. First of all, we notice that there is a mismatch between the reconstructions, and is not as sharp as in Fig.31; all of them are a bit more spread out. In this case, higher mismatches can be expected because these are not the final energies of the 3-tel stereo methodology; that will be the mean value of all three (weighted by the inverse of the variances). In this case the medians for LST-1 indicate that in average the energy is 22% higher than MAGIC-1 and 13% higher than MAGIC-2. Regarding the two MAGICs, M-2 energies are in average 7.4% higher than the ones calculated by M-1.

As we explained earlier, the data was processed using the same MC files, although different MC files are required for the data obtained after the volcano eruption of La Palma (2022). These files have not yet been produced so we had to use the available ones. If we perform the same analysis by restricting the data to the period before the volcano eruption, we observe that the reconstruction,

particularly in cases where there are larger mismatches, is reduced by approximately  $\sim 5\text{--}8\%$ . We will continue working with the same amount of data because this change will significantly affect the other results and will reduce a lot our already limited statistics.

## 6.2 Direction reconstruction

About the direction that is reconstructed in the DL2 step, we can check the correlation with the known location of the source, which in our case is the Crab Nebula (RA=5 h34m32 s, DEC=22°00'52"). The positions in equatorial coordinates are represented in Fig.33, where the data is also represented with different gammaness cuts. The left plot shows the reconstructed direction for all of the data. We can see that is very diffuse and covers only a few degrees of the sky, although a denser spot can be distinguished. If an initial gammaness cut is applied, as we see in central image of Fig.33, the background is significantly reduced. Even though the gammaness cut is weak ( $\gamma > 0.5$ ), the events are much more concentrated in the region of the sky where the Crab Nebula is located. If we apply further filtering by gammaness ( $\gamma > 0.95$ ), the results are shown in the right plot of Fig.33. At this point, a zoom into the region of interest has also been performed. The background near the source has been further suppressed.

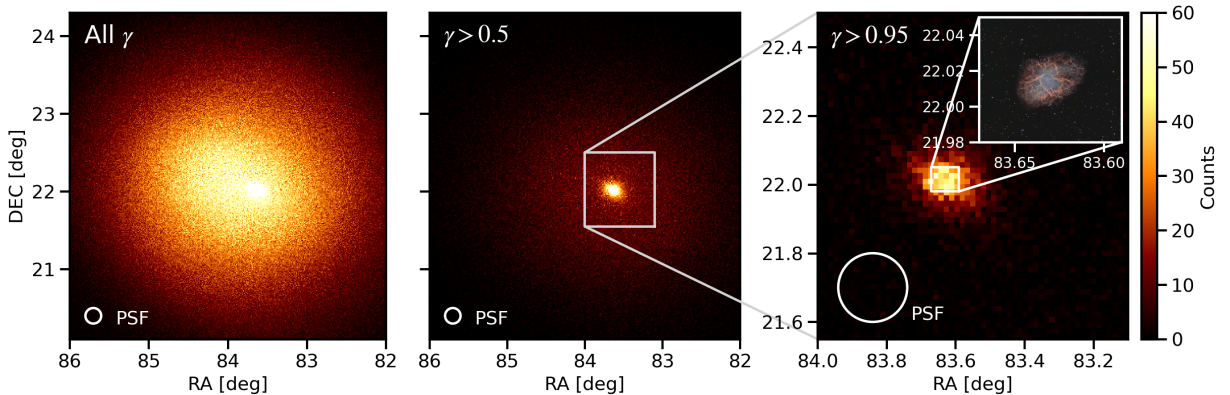


Figure 33: Different sky maps of the Crab Nebula data from this work. Represented in equatorial coordinates and with different gammaness cuts in each plot. Also featuring different zoom levels, with the last one displaying the multiwavelength image of the Crab Nebula observed by other instruments with higher angular resolutions (radio, optical and x-rays [58]).

Fig.33 also represents an approximation of the instrument's Point Spread Function (PSF); which shows the 68% containment within the energy range in which the energy resolution is lower  $\sim 5$  TeV (see Fig.6). This representation aims to provide a comparison of the angular resolution between IACTs and telescopes operating at other wavelengths. The last plot shows a zoomed-in view of the source region, along with observations made at other wavelengths. It can be observed that the angular resolution of LST-1 and MAGICs is not sufficient to resolve any details of the Crab Nebula. The instrument sees the source as a point source.

## 6.3 Geometrical reconstruction

Since the methods applied using `magic-cta-pipe` are still under development, we analyzed in detail each step and outcome of the processing, searching for any possible errors. We found some peculiar features in the analysis of some of the geometrical reconstructed parameters.

One of the parameters that we can study is the reconstructed "on-ground position". For each event, the shower axis is reconstructed (it should be aligned with the primary gamma-ray

direction for a gamma-initiated shower). The direction, and the point at which the axis crosses the  $z = 0$  plane (the so-called *shower core*) is stored. The reconstructed positions on the  $z = 0$  plane are shown in Fig.34. A pattern composed of three ellipses can be seen. It can also be observed that each ellipse is associated with one of the telescopes, with one of its focus located approximately at the position of the telescope. The other focus of all the ellipses is nearly shared by all three. This unexpected geometrical pattern indicates that some part of the reconstruction is not functioning correctly. The expected distribution should be more homogeneous in the areas near the three telescopes.

The events that are shown in Fig.34 are events detected by all three telescopes. We also explored the detection of events by two groups of telescopes instead of all three. The distributions obtained for the 2-telescope events are shown in Fig.35. It can be seen that the pattern is completely different from the distribution of events detected by all three telescopes. The observed pattern in this case is the expected one. A gap seems to form between the two telescopes that detected the events, indicating that no events have been reconstructed in this area. This is caused by the geometrical reconstruction using only 2 telescopes. An event falling in this area needs to be reconstructed almost perfectly; the alignment of the core and the two telescopes results in two nearly-parallel images, and the intersection of the corresponding planes will only very rarely lie close to the line joining the telescopes. This effect is also observed also in the analysis using MAGIC alone. We cannot draw any strong conclusions from this because these events are likely LE events, where the light does not reach one of the telescopes. We conducted some tests, and in general, the LE events do not reproduce the pattern found in Fig.34, so no strong conclusions can be drawn from this.

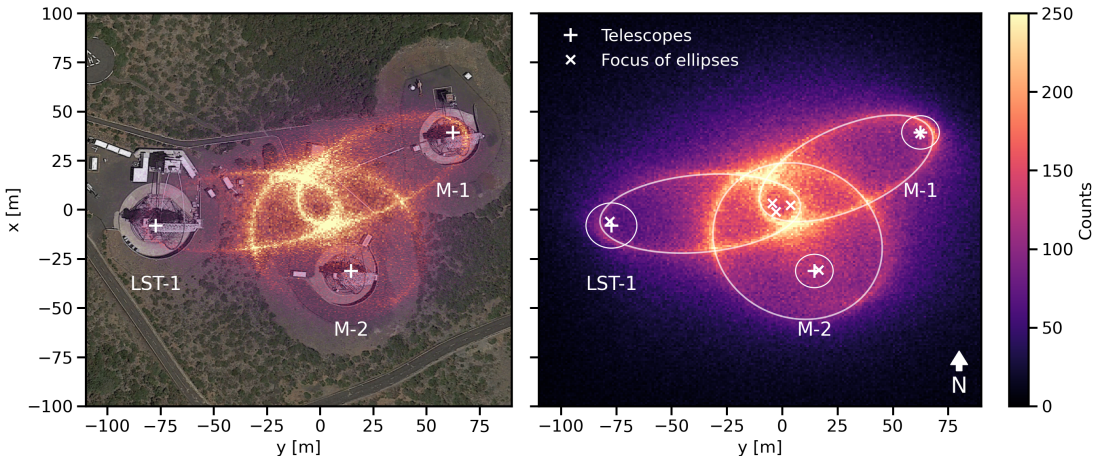


Figure 34: Distribution of reconstructed event positions in the plane  $z = 0$ . (Left) Shown with the on-site satellite image. (Right) Representing the respective sizes of each telescope’s mirrors and a fit of the three ellipses visible above the pattern. The different focus of each ellipse is also shown. The  $x$  and  $y$  axes are positioned according to the convention used in CORSIKA, with  $x$  increasing to the north and  $y$  increasing to the west (in a coordinate system looked from above) [68].

Another test that has been conducted was analyzing the MC files. The artifact was also present in the MC, which indicates that the issue is not caused by some problem specific to real data. From this check we observed that the pattern depends on the zenith distance of the observation. We will now present the results of the analysis using the MC files. This approach is chosen because, as a dependence on the zenith distance is observed in the pattern shape, it will provide more control by using data from a fixed pointing. Furthermore, in this situation, we have the true values of most of the actual variables that have been reconstructed.

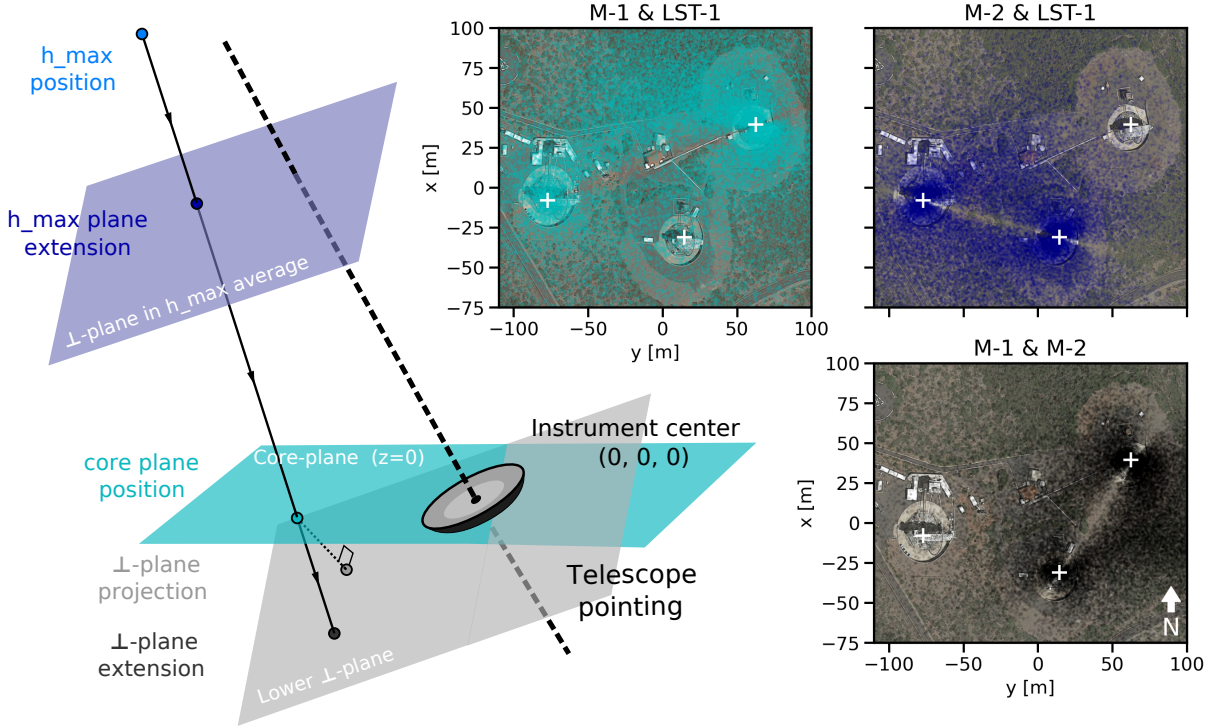


Figure 35: (Left) Sketch illustrating the different planes and geometric elements involved in the analysis. (Right) The three distributions for events detected in groups of two telescopes.

To further investigate this artifact, we can analyze the reconstructed positions more in detail. As telescopes are not pointing completely upwards, the core positions in the plane  $z = 0$  will be distorted. By considering the pointing direction and the reconstructed direction of the showers, we can project them onto different planes. The sketch of the different planes involved can be seen in Fig.35. We can project these positions onto the plane perpendicular to the pointing direction, passing through the mean location of the three telescopes at  $(0, 0, 0)$ . In addition to the projection, a prolongation of the trajectory will be calculated up to this plane. A plane which is more physically meaningful is the plane orthogonal to the shower direction located at the altitude at which the bulk of the detected light is emitted. This plane will be perpendicular to the pointing direction and will pass through the  $z = \text{mean}(h_{\max})$  point of the defined straight line of the pointing (see Fig.35).

In Fig.36 we can observe the analysis done for a MC file with  $zd = 23.63^\circ$ , which is relatively low. The  $h_{\max}$  points (altitude with maximum number of particles) and other projected points are represented. Note that the scale is not the same in all directions. The  $x$  and  $y$  coordinates span a few km, while the  $z$  direction about 20 km. The different projections are shown on the right side of Fig.36, all using the same scale.

In the  $z = 0$  plane shown in Fig.36, we observe a similar pattern to the one shown in Fig.34. The projection and expansion of the shower trajectories is shown in gray. It can be observed that the pattern is still present but is no longer stretched in the observation direction, and it regains a more circular shape. Although the shape cannot be completely circular due to the asymmetric footprint of the telescope array and the presence of the Earth's magnetic field [26]. It should be noted that the pattern is not visible in the upper plane projection (in blue) with the same coordinate scale. This may indicate that the problem arises when the direction of each event is determined. The different ellipses observed in the pattern do not show any relation to the trajectory of the particles or the true reconstructed positions. Furthermore, no dependence

on intensity, energy, width, or length is found. The only thing that can be observed is that the pattern disappears with lower energy events. However, with these events, the reconstruction is usually imprecise, so perhaps the pattern is simply blurred.

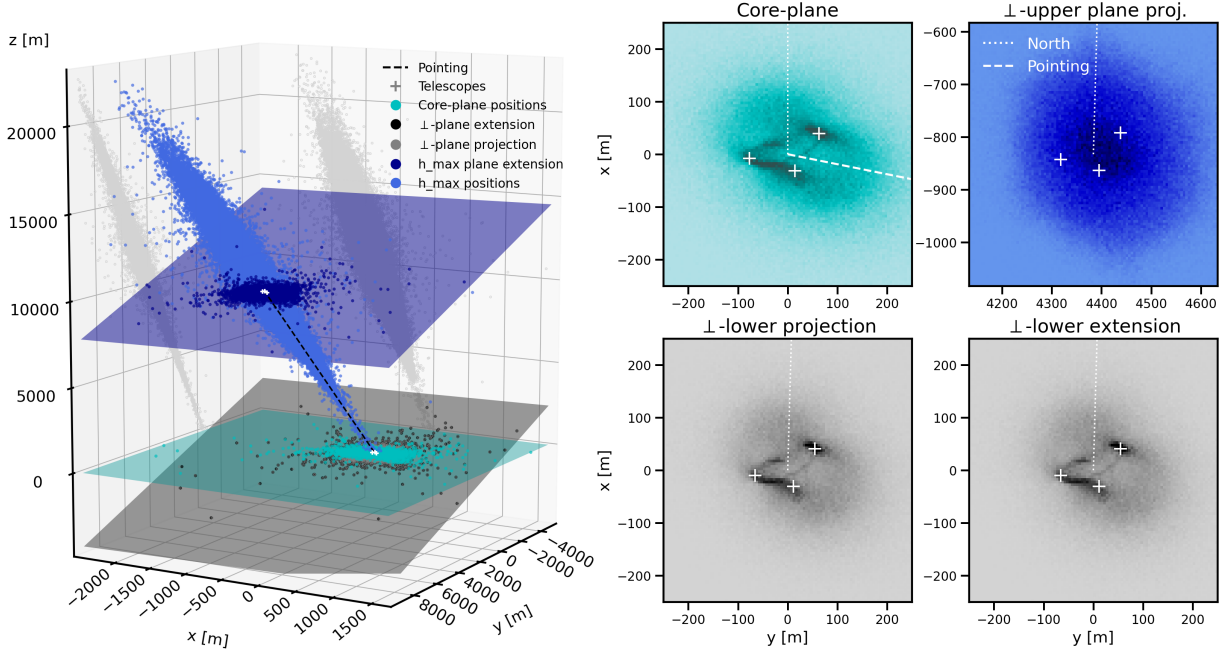


Figure 36: An example of the geometrical analysis using an MC file with  $zd = 23.63^\circ$ . (Left) A three-dimensional representation of the planes and the projected points. (Right) The distributions of the reconstructed positions in the different planes. The pointing position and the north position are displayed, illustrating how the north position changes when the planes are projected. Since the zenith distance is small in this case, the north is pointing almost in the same direction in all planes.

Some more checks have been done in order to find the source of this artifact. A search has been conducted to find a relation between the particles that fall within the denser ellipses and certain parameters, but no significant relation was found. The impact parameters have been recalculated, and the distances between the reconstructed and true positions in the planes have been determined. No insights or additional information regarding this artifact have been discovered. The relevant information that could be extracted from this work regarding this problem has been communicated to the individuals working on the development of `magic-cta-pipe`.

#### 6.4 Instrument Response Functions (IRFs) and instrument characterization

The IRFs of an instrument characterize its response (i.e., what it reconstructs) as a function of the true parameters of the detected phenomenon (a gamma ray, in our case), allowing the effects of the instrument during data collection to be later corrected in the analysis. The objective is to obtain physical results about the object of study, that can then be compared to those obtained by different instruments. In our case, the IRFs can be constructed using controlled MC data. We can also use the Crab Nebula (standard candle of gamma-ray astronomy) to compute some IRFs directly from the real observations [57]. In this situation, some parameters may not be fully known when using only real data. However, a good estimation of different IRFs can still be calculated.

In this case, since we are observing the Crab Nebula, the analysis will be *source-independent*,

meaning that the position of the source is not assumed to be the nominal value of Crab Nebula for the MC files [65, 69]. In this work, 5 OFF-zones are used (the definition and methodology of the ON and OFF-regions are described in Section 2.3.1), as shown in Fig.37, where the two different wobbles can be distinguished; these are the two pointing positions symmetric around the source. The ON-OFF analysis is performed by counting events in the ON and OFF regions, and then subtracting the background contribution (inferred from the OFF zones). The number of excess events is calculated as follows,

$$n_{\text{excess}} = n_{\text{ON}} - n_{\text{OFF}} = n_{\text{ON}} - \frac{1}{n_{\text{off reg}}} \sum_i^{n_{\text{off reg}}} n_{\text{OFF}}^i. \quad (4)$$

Where  $n_{\text{ON}}$  is the number of events in the ON region,  $n_{\text{off reg}}$  the number of OFF regions, that in this work is 5. And  $n_{\text{OFF}}^i$  represents the number of events that fall into each OFF-region ( $i$ ). To calculate this, the regions must be properly defined. For each region, a angular  $\theta$  cut should be done. Otherwise, as can be observed in Fig.37, for OFF-regions 3 and 4, the signal of the source starts contributing to the OFF region. This cut needs to be optimized. If it is too loose, a lot of noise is integrated together with the signal, and the signal may contaminate some of the OFF regions; if it is too tight, excess events will be lost. In all the analysis methods the chosen cut is  $\theta^2 < 0.04 \text{ deg}^2$ . These values are the standard used.

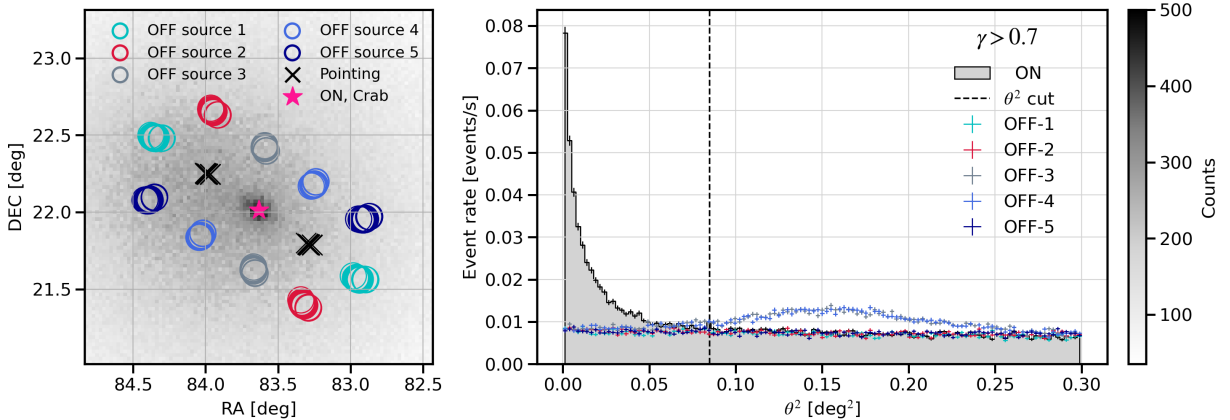


Figure 37: Reconstructions for data with no energy cuts and a cut in gammaness of 0.7, all reconstructed with 3-telescope stereo analysis. (Left) The sky map in equatorial coordinates of the Crab Nebula. Showing the ON-region, as well as the pointing positions and the OFF-regions. (Right) An example of an event excess calculation, showing the rates for the ON-region and all 5 OFF-regions. The event rate per bin is shown for all the regions.

We are applying cuts in the direction of reconstruction of an event, but this is not enough as the cosmic ray background will be also producing events in the ON-region. A gamma/hadron separation needs to be applied [38], in this case performing a cut in gammaness. This can be achieved in various ways. The simplest approach is to apply a fixed gammaness cut that provides sufficient statistics. This is not the most optimal thing that can be done, as the gammaness is computed using the RFs and it has different efficiencies in different energy ranges [68, 70]. To account for that, the gammaness cut can be performed in energy bins by applying a fixed cut in each bin, referred to as the *dynamic cut*. The cut can be determined as the gammaness value that retains a certain percentage of events, we used 68 % and 90 %. These values are calculated using gamma MC files, where all events are known to be gammas. The cuts are determined for each bin of reconstructed energy as the gammaness value that retains 90 % of events. The results are shown in Fig.38. It can be observed that the regions with higher optimal gammaness cut are between 1 TeV and 10 TeV.

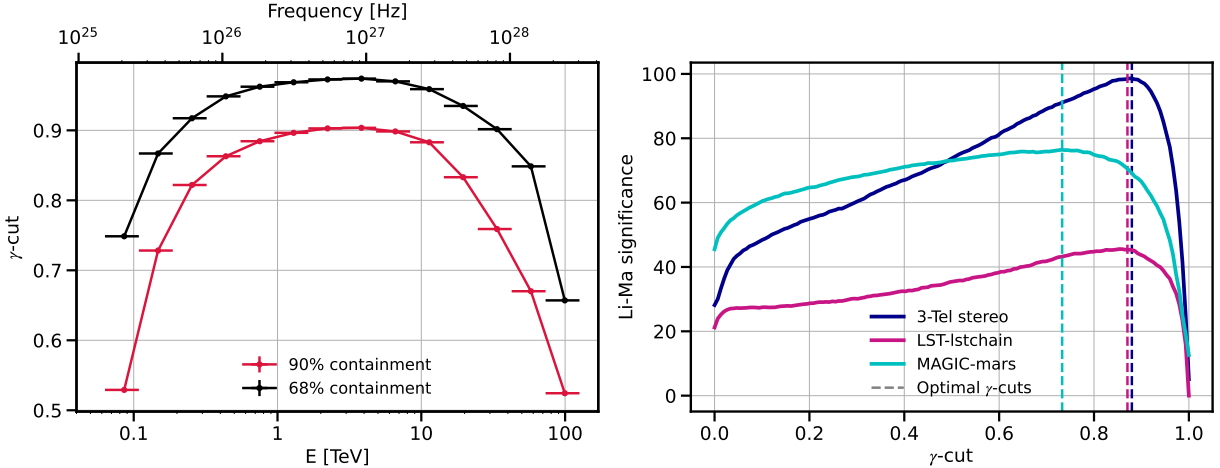


Figure 38: (Left) Gammaness cuts per bin that retain 68 % and 90 % of the gamma rays. Computed using gamma MC files. (Right) The Li-Ma significance [71] obtained for different values of gammaness cuts. All three instruments results are displayed.

Another way of filtering by gammaness is to observe the significance of the hypothesis of having a source in the expected position (in our case, the nominal position of the Crab Nebula) compared to the background signal alone. This significance can be maximized by varying the gammaness cut. This is done using the Li-Ma significance [71] from the `pyirf` Python library [72]. In order to compute the significance the only input that is needed are the counts in the different regions. After maximizing the gammaness cut, the one that gives us the highest significance can be used as a fixed cut. The different significances for all instruments are shown in Fig.38, and the values that maximize the significance are given in Table 5. Comparing the significances obtained by each instrument, the one achieved with the 3-telescope stereo is 29 % higher than MAGIC and a 116.4 % higher than LST-1 alone.

Table 5: The maximum values of significance found for each of the analysis methods are shown in Fig.38. The respective fixed gammaness cuts to achieve these results are also given.

	3-tel stereo	LST-1 (lstchain)	MAGIC (mars)
Achieved significance [ $\sigma$ ]	98.59	45.56	76.42
Gammaness cut	0.879	0.852	0.732

The first IRF we will calculate to characterize the instrument is the *angular resolution*. The angular resolution is defined as the angle within which the 68 % of excess events are contained [73, 74]. It is calculated per energy bin. Also, in the bins where the OFF-region subtraction provides a negative number of counts, it will be taken as zero. An example of the  $\theta^2$  distributions for different energies is shown in Fig.39.

Finding the 68 % containment of excess events in the distribution obtained by subtracting the OFF counts from the ON counts will give the angular resolution. In this case, for all three instruments being analyzed, 7 energy bins were chosen, ranging from 50 GeV to 20 TeV. The results are shown in Fig.40. The different gamma cuts defined above are used. The 90 % dynamic cut seems to perform better in the high-energy regimes, while the fixed gammaness cuts produce higher angular resolution at lower energies. The obtained results for MAGIC are compatible with reference values [34, 73] as well as for LST-1 [65, 75]. The obtained minimum angular resolutions are shown in Table 6.

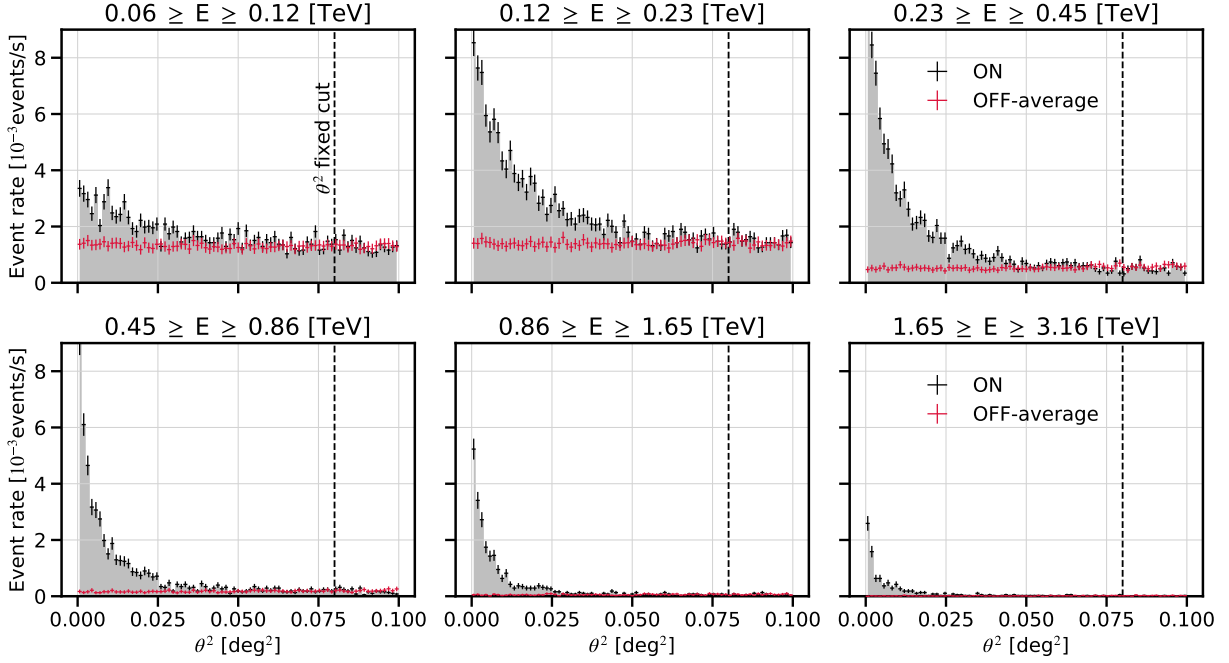


Figure 39: Distributions of  $\theta^2$  counts in the ON and OFF regions. One plot per energy bin, where there are 6 energy bins defined, each with a width of 0.25 on a logarithmic scale.

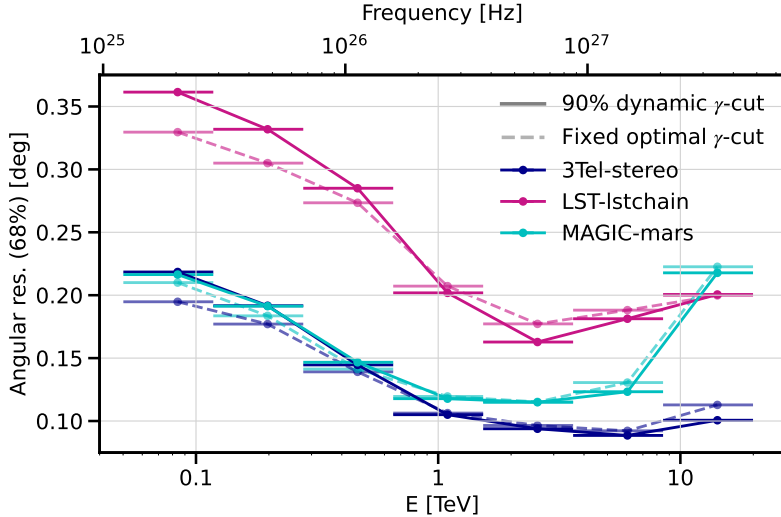


Figure 40: The angular resolution is computed in 7 different energy bins. The calculations have been performed for each instrument, considering two gammaness cut options: 90 % gamma containment (solid lines) and the fixed cut that maximizes the Li-Ma significance (dashed lines).

Table 6: The best angular resolutions are achieved as shown in Fig.40. The energy bin corresponding to the minimum angular resolution is also provided. The minimum values for all three analysis methodologies are obtained using the dynamic 90 % gammaness cuts.

	3-tel stereo	LST-1 (1stchain)	MAGIC (mars)
Minimum angular resolution	$0.089^\circ$	$0.16^\circ$	$0.11^\circ$
Energy where is achieved	$\sim 6 \text{ TeV}$	$\sim 2.5 \text{ TeV}$	$\sim 2.5 \text{ TeV}$

The 3-telescope stereo analysis seems to have better resolution at higher energies compared

to both other instruments and is very similar to the two MAGICs in the lower energy regime. In this region, the LST-1 standalone analysis has a much higher angular resolution and only seems to approach the other two instruments in the higher energy regime [69]. In general the angular resolution achieved with the 3-telescope analysis is similar but slightly better than that of MAGIC alone. The differences with MAGIC are of  $\sim 0.005^\circ$  for energies lower than 1 TeV and  $\sim 0.03^\circ$  for higher energies. The results obtained for the LST-1 standalone analysis are compatible with those achieved in the LST-1 performance paper [65], and the results obtained in the 3-telescope analysis are also compatible with those obtained in the performance paper of LST+MAGIC [69].

The other IRF we are going to work with, which characterizes the instrument, is the *sensitivity*. The sensitivity is defined as the minimum flux from a point-like source that the telescope can detect with  $5\sigma$  of significance in a determined time of 50 h [65, 69, 73, 75]. Calculated using 5 OFF regions and logarithmic bins with a width of 0.2 in logarithmic scale. Additionally, it needs to fulfill other conditions: at least 10 excess events need to be detected, and a signal-to-background ratio of 5 % is also required. This is why we have chosen 5 OFF zones for our analysis. In this work, we will calculate the so-called *integral sensitivity*, which has the same definition but is defined for wider energy ranges. We will calculate the integral sensitivity for energies greater than 300 GeV and for energies less than 300 GeV. In order to do that, the cuts; in gammaness and  $\theta^2$  need to be optimized. For each of the two datasets we will calculate the sensitivity using different cuts. The value of the integral sensitivity will be computed by looking for the minimum flux which fulfills the sensitivity definition, performing a 2-D scan of the cut values (in gammaness and  $\theta^2$ ). We have ensured that we have sufficient statistics in each of the ranges to fulfill always the two conditions needed for the sensitivity computation. The obtained  $\theta^2 - \gamma$  planes for each energy range and instrument are shown in Fig.41, and the achieved sensitivity is given in Table 7.

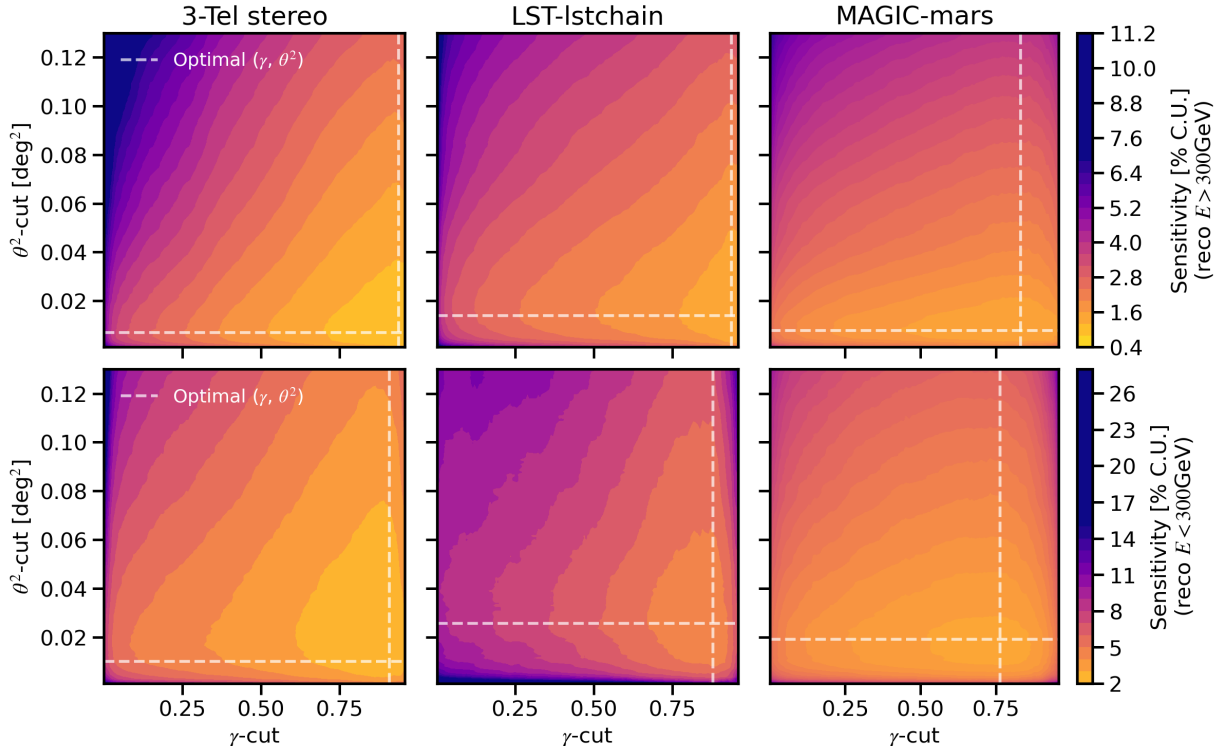


Figure 41: Integral sensitivity calculated for all three instruments and two energy ranges ( $E > 300$  GeV above plots, and  $E < 300$  GeV below plots). The sensitivity has been calculated for a grid of  $\theta^2$  and  $\gamma$ , and the minimum achieved sensitivity is indicated along with the corresponding optimal parameters.

Table 7: Computed integral sensitivities for both energy ranges ( $E < 300$  GeV and  $E > 300$  GeV).

	3-tel stereo	LST-1 (1stchain)	MAGIC (mars)
Integral sensibility $E < 300$ GeV	2.09 % C.U.	4.21 % C.U.	2.99 % C.U.
Integral sensibility $E > 300$ GeV	0.79 % C.U.	1.21 % C.U.	1.38 % C.U.

First of all, it can be seen in Fig.41 and Table 7 that, in both energy ranges, the 3-telescope analysis achieves better sensitivity than MAGIC, and MAGIC, in turn, achieves worse sensitivity than LST-1. The sensitivity is decreased by 50% and 34% for  $E < 300$  GeV and  $E > 300$  GeV, respectively, compared to MAGIC analysis, and by 30% and 43% compared to LST-1 analysis. The achieved sensitivities for MAGIC and LST-1 standalone are compatible with those obtained in their respective individual analysis [65, 73, 75]. Regarding the optimal parameters, it can be observed that they differ for each instrument. For the 3-telescope analysis, the optimal parameters include a low  $\theta^2$  cut and a strong gammaness cut. In the case of MAGIC, the cut in  $\gamma$  is not as strong, while for LST-1, the cut in  $\theta^2$  is relatively softer.

In the standard analysis, IRFs are computed using gamma MC files on a run-by-run basis, meaning that one IRF is computed for each run [72]. They are computed using the `1st1_magic_create_irf` tool from `magic-cta-pipe`, and they include the *migration matrix* for the energy values. The migration matrix determines the discrepancy between the reconstructed energy values and the actual values. An example of a migration matrix for MC files at a zenith distance of 45° is shown in Fig.42. This migration matrix has been computed using 14 energy bins of width 0.2 in logarithmic scale, which corresponds to the energy axis used in the subsequent DL3 analysis.

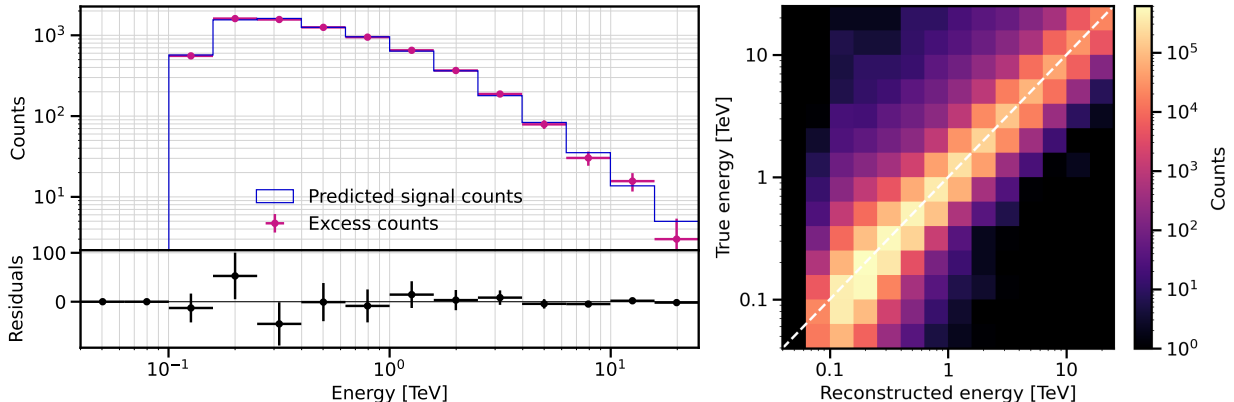


Figure 42: (Left) The predicted counts obtained using the migration matrix from IRFs plotted alongside the real data (obtained with a fit of the data, see section 7). Additionally, the residuals (data-model) have been calculated. (Right) The migration matrix computed for an MC file with a zenith distance of 45°, using 14 energy bins of width 0.2 in logarithmic scale.

With the migration matrix, the predicted counts in each energy bin can be computed. We can compare this with the real data results (where a fit has been performed using the data, this fit will be explained in section 7), as shown in Fig.42, where the residuals are also represented. The application of the IRFs is necessary to determine the spectrum or fluxes of the source while accounting for the limitations of the instrument’s measurements. This final step, which involves applying the IRFs to the data, will be performed using the Gammapy software.

## 7 Analysis beyond DL2: Spectrum and light curves

Gammify is a software for high-level data analysis framework of CTA [61, 3]. It is used to obtain final products such as light curves and Spectral Energy Distributions (SEDs). Gammify uses binned Poisson maximum likelihood estimation methods to fit the parameters. Using this method, the SED can be computed in the specified energy bins, assuming that the source (in our case, the Crab Nebula) is a point source and its position is assumed to be the same as the nominal Crab Nebula position. In this work, the version of Gammify used is v1.0. The DL3 data is passed to Gammify, and then the models and estimators can be built. For this analysis, a total of 44 LST-1 runs were used.

First of all, the different sky regions are defined using a global  $\theta^2$  cut of  $0.04 \text{ deg}^2$ . In this analysis, 3 OFF-regions are used. We also create the energy axes. For the reconstructed energy, we used 5 bins per decade from  $40 \text{ GeV}$  to  $25 \text{ TeV}$ , and for the true energy, 10 bins per decade from  $10 \text{ GeV}$  to  $100 \text{ TeV}$ . A Gammify "maker" is created to run a data reduction chain. This reduction transforms the data into the number of counts within ON and OFF-regions, and exposure. In this step, the IRFs are applied.

The Spectral Energy Distribution (SED) is the differential energy flux, represented as  $\frac{dN}{dE}$  (number of photons per area per time per energy), multiplied by the square of the energy [76]. In general, the SED is a good way to represent how emitted photons are distributed over energies, as photons with lower energy contribute less to the total energy compared to higher energy particles. Multiplying the SED by  $E^2$  will result in units of  $\text{erg cm}^{-2} \text{s}^{-1}$ , i.e., energy per area per time. Also, when represented on a logarithmic energy scale, the area under the SED directly represents the total energy [76]. The SED is obtained from the dataset using the `FluxPointsEstimator` tool from Gammify. It will be fitted with a log parabola model [77], which is given by,

$$\frac{dN}{dE}(E) = \Phi_0 \left( \frac{E}{E_{\text{ref}}} \right)^{-\alpha - \beta \log\left(\frac{E}{E_{\text{ref}}}\right)}. \quad (5)$$

Where  $\Phi_0$  is the amplitude factor,  $E_{\text{ref}}$  is the reference energy (i.e., the normalization factor), and  $\alpha$  and  $\beta$  are the parameters that characterize the parabola. The logarithms will always be in base 10.

### 7.1 Light curves

To obtain the flux of gamma rays in a specific energy range, the runs are analyzed one by one. This is done after fitting the model to the data. Then, when the data is characterized by a log parabola and all the parameters are obtained, the geometric parameters  $\alpha$  and  $\beta$  are fixed and assumed to be constant across all observations. The amplitude  $\Phi_0$  remains as a free parameter. By fitting the model run by run, the magnitude of the amplitude provides the corresponding flux in each observation. The flux estimation is performed using the `FluxPointsEstimator` tool from Gammify. The result of the run-wise light curve estimation for the Crab Nebula is shown in Fig.43.

The fluxes in Fig.43 correspond to 44 LST-1 runs. The observations can be separated into two time periods: winter and spring of 2020-2021, and spring 2021-2022. The flux of the Crab reference,  $0.790 \times 10^{-9} \text{ cm}^{-2} \text{s}^{-1}$  [78], is represented with a dashed line. The best constant fit for the flux, along with its respective standard deviation, is shown with a solid line ( $0.792 \pm 0.159 \times 10^{-9} \text{ cm}^{-2} \text{s}^{-1}$ ). The obtained value has a difference of only 2.5 % from the reference. However, we can see that the dispersion of the values is significant, approximately 20 % of the value. This can be attributed to varying cut efficiencies and background normalization [65]. Additionally,

the two periods analyzed differ by almost one full year. During this period, the eruption of the Cumbre Vieja Volcano took place, and the instruments stopped taking data for months. This could have led to changes in the performance of the instruments.

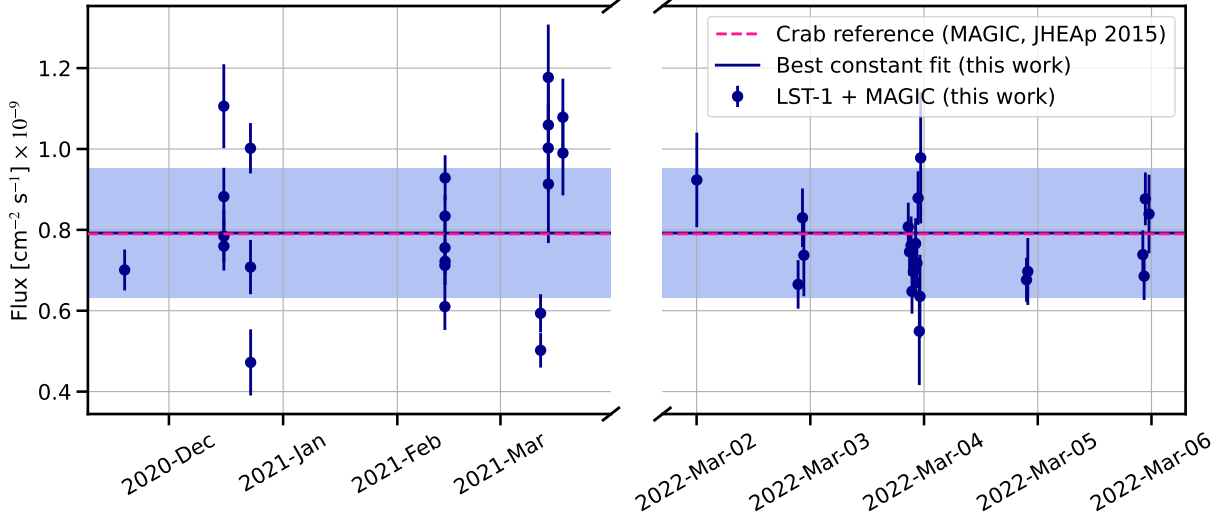


Figure 43: Light curve for Crab Nebula for energies greater than 63 GeV.

## 7.2 Spectral Energy Distributions (SEDs)

Now the SED points we obtained from our data will be analyzed. As explained, the data will be compared to a log parabola model (5). The comparison can be done by considering the Crab reference values [78]:  $\Phi_0 = 3.23 \times 10^{-11} \text{ cm}^{-2} \text{ s}^{-1} \text{ TeV}^{-1}$ ,  $E_{\text{ref}} = 1 \text{ TeV}$ ,  $\alpha = 2.47$ , and  $\beta = 0.24$ , with a Compton peak located at 105 GeV. By fitting the obtained points from this work, the resulting log parabola is represented in Figure 44.

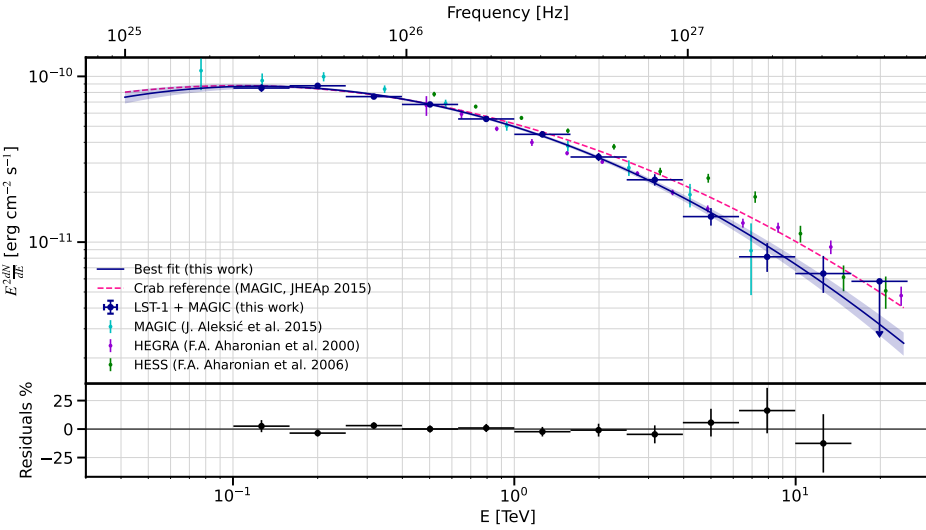


Figure 44: SED of the Crab Nebula obtained in this work. The solid line represents the best fit for this work, with the shaded area representing the statistical uncertainties. The dotted line represents the reference model [78]. It is also shown alongside SED points from other instruments: green points for HESS [79], cyan for MAGIC data [78], and purple for HEGRA [80].

The obtained parameters for our data are  $\Phi_0 = 3.104 \pm 0.062 \times 10^{-11} \text{ cm}^{-2} \text{ s}^{-1} \text{ TeV}^{-1}$ ,  $\alpha = 2.536 \pm 0.019$ , and  $\beta = 0.128 \pm 0.012$ , with  $E_{\text{ref}} = 1 \text{ TeV}$ . We can observe that the obtained fit

is softer for higher energies compared to the fit of [78]. However, in general the errors are low and there is a good agreement with both models. In our results, the Compton peak is located at 123 GeV. The residuals are also represented, and they have been calculated using,

$$\text{Residuals\%} = \frac{\Phi_{\text{model}} - \Phi_{\text{exp}}}{\Phi_{\text{model}}} \times 100. \quad (6)$$

Where  $\Phi_{\text{exp}}$  is the obtained experimental SED point, and  $\Phi_{\text{model}}$  is the corresponding value of the SED for the model evaluated at the same energy as the experimental point. The residuals are generally small, where the largest disagreement is around 20 %. The uncertainty is shown as a shaded area in Fig.44, but this uncertainty represents only the uncertainty coming from statistics. There will also be systematic uncertainties, given by the methodology [81, 82]. Using MC simulations to analyze the data will always introduce a certain systematic error. Since the atmosphere is part of the instrument and varies over time, we do not know the conditions that exist at all times. It will also be a significant source of uncertainty, and the background estimation will also have uncertainties [83]. In order to estimate the systematic contributions, some parameters are changed in the simulations, and the resulting change in the SED will characterize this error. It is studied how underestimating and overestimating the arriving light can affect the resulting spectrum. IACTs have systematic uncertainties in the energy scale of around  $\sim 15\%$  [81, 84]. The systematic uncertainties of the MAGIC+LST-1 system have not been analyzed in detail. In fact, there is not yet an LST-1 publication focused on systematic errors. But as discussed in [69], the systematic uncertainty for the group of three telescopes should be similar of those of MAGIC ( $\sim 15\%$ ).

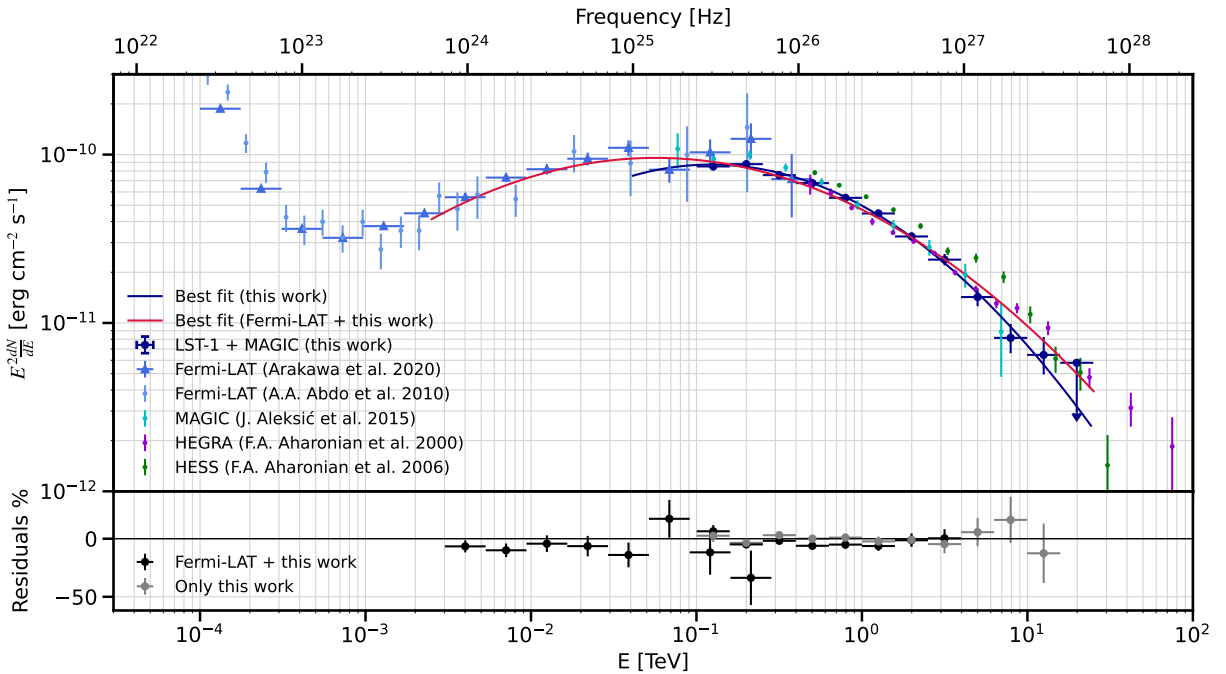


Figure 45: SED points of this work in dark blue, Fermi-LAT in light blue (dots and triangles) [85, 86], cyan for MAGIC data [78], green points for HESS [79] and purple for HEGRA [80]. The best log parabola fit for MAGIC+LST-1 is represented by a pink solid line.

We know that the Crab Nebula in HE and VHE can be characterized with a log parabola [78]. However, for our work, the energy threshold is at about 60 GeV, so the lower energy part of the bump is not covered. To perform the fit while also considering the low-energy gamma rays, we will use data from Fermi-LAT [85, 86]. The Fermi-LAT instrument covers the energy range from

200 MeV to 300 GeV, overlapping with MAGIC. All Fermi-LAT points, taken from [85, 86], are shown in Fig.45. Thus, by using the Fermi-LAT points that cover LE and HE gamma rays, along with LST-1+MAGIC covering HE and VHE, we perform a log parabola fit. We can observe that around 1 GeV, the SED is no longer modeled with a log parabola. Therefore, we selected the last points for Fermi-LAT and the first points of MAGIC+LST-1. The selected points can be seen in the residuals plot in Fig.45.

For this case, the parameters obtained for the fit are  $\Phi_0 = 2.942 \pm 0.078 \times 10^{-11} \text{ cm}^{-2} \text{ s}^{-1} \text{ TeV}^{-1}$ ,  $\alpha = 2.493 \pm 0.018$ , and  $\beta = 0.086 \pm 0.030$  using  $E_{\text{ref}} = 1 \text{ TeV}$ . The Compton peak is displaced from 123 GeV to 57 GeV.

### 7.3 Multiwavelength analysis

We have analyzed the SED of the data processed in this work, for MAGIC+LST-1, in the HE and VHE ranges. However, with this approach, a study of the emission mechanisms present in the source cannot be conducted [57]. To accomplish that, we need to consider the full Crab Nebula spectrum. In Fig.46 the multi-wavelength spectrum of the nebula, with measurements from radio to gamma rays, is shown. The radio points (red and dark red) are from [87, 88, 89, 90], the optical points (green) from [91, 92], the x-ray ones (cyan) from [93, 94] taken with INTEGRAL-SPI and XMM-Newton. For the gamma-ray band, specifically for the LE and HE ranges, Fermi-LAT points are displayed [85, 86] (cyan), whereas for the HE and VHE ranges, we solely included the data points from this work (dark blue), excluding others (as shown in Fig.44). This selection allows us to examine the effect of our data on the SED. The HEGRA data (purple) [80] is not included in the fit, but it is displayed to observe if the behavior in the higher VHE range aligns with the model.

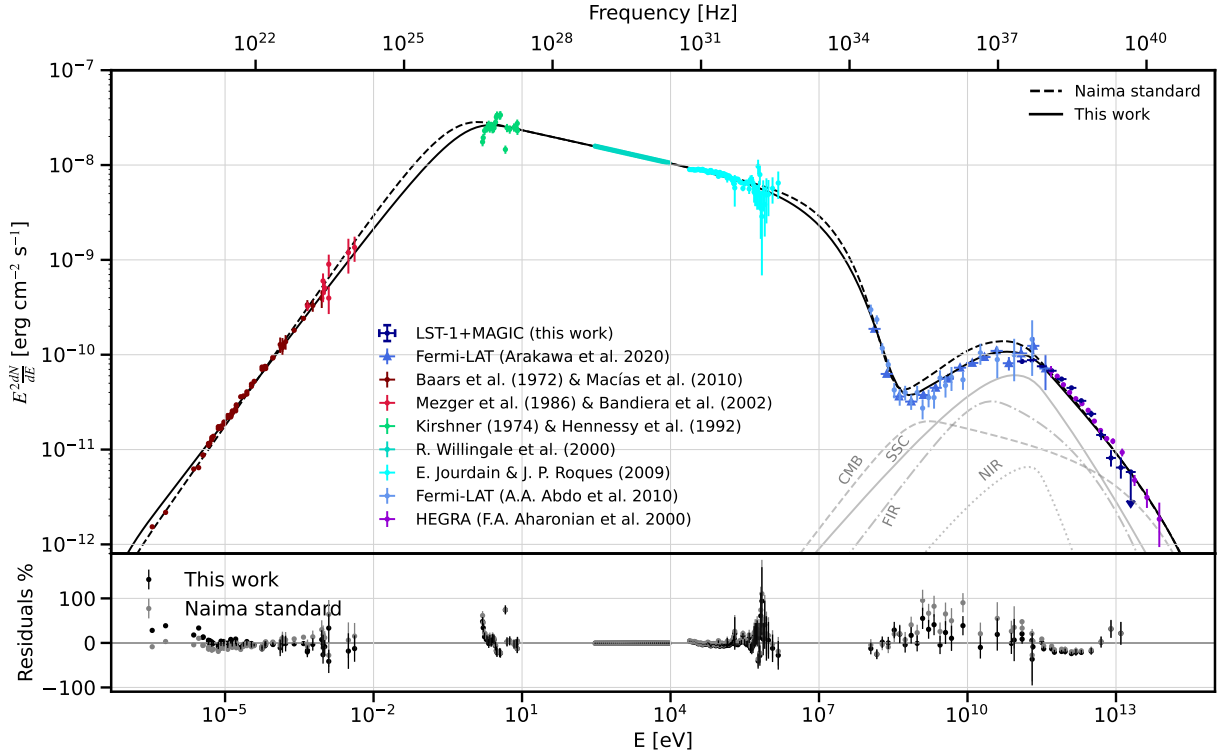


Figure 46: Multiwavelength SED of the Crab Nebula. Points from various observations are represented in different colors (see the text for references to the respective points). Multiwavelength fit incorporating contributions from various radiative mechanisms. Residuals are displayed for each point used.

In order to build a model to fit the Crab SED we will use *Naima* radiative processes Python package [95]. This software provides the tools to generate different radiative model contributions based on the parameters of the source. By using the experimental points and a model with various free parameters, we can fit the model to the points and obtain a phenomenological fit for all the parameters [96]. The mechanisms considered for the Crab Nebula will be synchrotron for lower energies [45], and for higher energies, IC [47, 48], including contributions from Synchrotron Self-Compton (SSC), IC over the CMB, and over Far Infrared (FIR) and Near Infrared (NIR). Bremsstrahlung or neutral pion decay is not considered because it is not believed to have significant importance for the Crab Nebula SED [97, 98]. The synchrotron part of the SED can be modeled using different combinations of magnetic field and electron density: there is a degeneracy between these two parameters. Including the IC part in the fit will resolve this degeneracy.

There are some fixed parameters we will take into account following the arguments used in [99]. The distance to the Crab Nebula can be fixed at a value of 2 kpc, which is the nominal value [100]. The NIR and FIR contributions to IC are fixed based on measurements of infrared energy densities and temperatures [101, 102]:  $\epsilon_{\text{NIR}} = 1 \text{ eV cm}^{-3}$  with a temperature of 5000 K, and  $\epsilon_{\text{FIR}} = 0.5 \text{ eV cm}^{-3}$  with a temperature of 70 K. The CMB is fixed at the standard temperature of 2.7 K [103]. The free parameters to be determined through the fit are the electron distribution and the magnetic field. In our case, the population of electrons will be described by a general Exponential Cut-off Broken Power Law (ECBPWL) [104], which is defined with:

$$\frac{dN}{dE}(E) = A \exp\left(-\left(\frac{E}{E_{\text{cut-off}}}\right)^{\beta}\right) \times \begin{cases} \left(\frac{E}{E_0}\right)^{-\alpha_1} & E \leq E_{\text{break}} \\ \left(\frac{E_{\text{break}}}{E_0}\right)^{\alpha_2-\alpha_1} \left(\frac{E}{E_0}\right)^{-\alpha_2} & E > E_{\text{break}} \end{cases} \quad (7)$$

Here,  $A$  represents the amplitude with units of  $\text{eV}^{-1}$ ,  $E_0$  denotes the normalization energy, which is fixed at 1 TeV in our case.  $\alpha_1$  and  $\alpha_2$  represent the two power law slopes that compose the electron spectrum.  $E_{\text{break}}$  refers to the energy where the slope changes,  $E_{\text{cut-off}}$  represents the energy at which the cut-off occurs, and  $\beta$  is the exponent for the exponential cutoff energy. The fit was performed using non-linear least squares estimation with the help of `scipy` [105]. Fig.46 displays the SED points and derived models.

Fig.46 displays the Crab Nebula model with the *Naima* standard parameters (from Eq.(7)) represented by the dotted line [99], along with the SED model obtained from the fit in this work, shown as the solid line. The residuals for both models have also been calculated using Eq.(6). The parameters obtained for our model, along with a comparison to the standard Naima parameters, are presented in Table 8.

Table 8: The parameters obtained from the multiwavelength fit in this work are compared to the standard parameters used in *Naima* [99]. The relative difference is calculated using  $(x_{\text{naima}} - x_{\text{this work}})/x_{\text{naima}}$ , where  $x$  represents the different parameters. For the case of the spectral indexes ( $\alpha_1$ ,  $\alpha_2$  and  $\beta$ ) the differences are given simply by  $\Delta x = x_{\text{naima}} - x_{\text{this work}}$  for each spectral index  $x$ .

	Amplitude [ $\text{TeV}^{-1}$ ]	$E_{\text{cut-off}}$ [TeV]	$E_{\text{break}}$ [TeV]	$\alpha_1$	$\alpha_2$	$\beta$	$B$ [ $\mu\text{G}$ ]
<i>Naima</i>	$3.70 \times 10^{24}$	1863	0.27	1.50	3.23	2	125.0
This work	$(1.94 \pm 0.15) \times 10^{24}$	$1577 \pm 171$	$0.376 \pm 0.023$	$1.636 \pm 0.018$	$3.2313 \pm 0.0090$	$1.37 \pm 0.17$	$119.3 \pm 2.9$
Relative diff.	47.6 %	15.3 %	-40.7 %	$\Delta_{\alpha_1} = -0.14$	$\Delta_{\alpha_2} = 0.0013$	$\Delta_{\beta} = 0.63$	4.5 %

We can see that the electron density (the amplitude of the ECBPWL) and the magnetic field in our work are lower, and the other parameters are also slightly different, but overall, they are in the same ballpark as the standard ones for Crab Nebula in *Naima*. The full electron population can be seen in Fig.47. Both populations are very similar in the part after the break and before the

cut-off (with  $\alpha_2$  being the same for both fits), but they differ slightly in the other two sections. Fig.46 shows that our work provides a better fit in the HE and VHE part of the SED, whereas the Naima standard model fits the radio experimental points better.

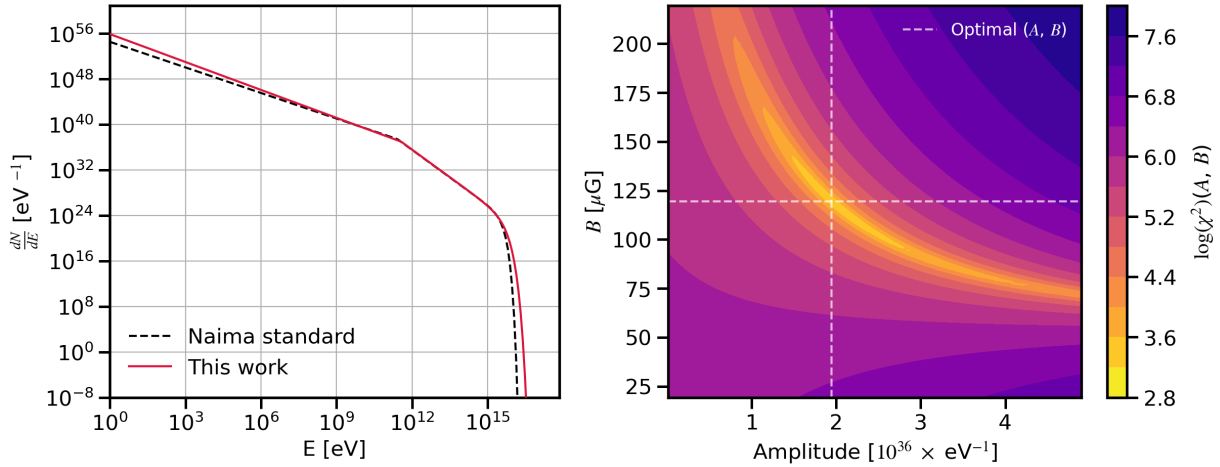


Figure 47: (Left) Electron spectra computed for the Naima standard fit [95, 99] and the one obtained in our work are shown. (Right) Least squares estimator values represented in the amplitude of the electron population and magnetic field plane are shown. The point representing the obtained minimizing parameters is shown. The degeneracy between amplitude and  $B$  is clearly seen on the right panel.

A first-order estimation for the magnetic field in astrophysical sources can be performed by comparing the luminosity data of the HE and VHE with the X-rays [95, 106]. This estimation can be carried out using the following expression:

$$\frac{L_{\text{X-ray}}}{L_\gamma} \approx \frac{u_B}{u_{\text{ph}}} = \frac{B^2}{8\pi u_{\text{ph}}} \quad (8)$$

We used the `estimate_B` utility from Naima, which takes the SED points as input, calculates the luminosities, and returns an estimation of the magnetic field. We obtained a magnetic field of  $B = 91.07 \mu\text{G}$ . It is of the same order of magnitude as the result obtained in the fit. Other parameters that can be inferred from the SED are the energy contributions of the different emission mechanisms in the model. As defined before, in logarithmic energy scale, the SED integration provides the total energy emission of the source [76]. Therefore, by integrating the SED contributions separately, we obtain the results shown in Table 9.

Table 9: The energy budget provided by different SED contributions is shown. All units are given in  $\text{keV cm}^{-2} \text{s}^{-1}$ . The relative difference is calculated as  $(E_{\text{naima}} - E_{\text{this work}})/E_{\text{naima}}$  where  $E$  represents the respective value. The CMB, NIR, and FIR contributions are the same, as they are fixed by experimental measurements [101, 102, 103].

	Total	Synchrotron	IC (Total)	IC (SSC)	IC (CMB)	IC (NIR)	IC (FIR)
Naima [ $\text{eV cm}^{-2} \text{s}^{-1}$ ]	$1.82 \times 10^5$	$1.81 \times 10^5$	518.9	287.8	99.41	19.22	112.4
This work [ $\text{eV cm}^{-2} \text{s}^{-1}$ ]	$1.68 \times 10^5$	$1.67 \times 10^5$	416.2	194.3	99.41	19.22	112.4
Relative diff.	8.01 %	7.98 %	19.79 %	32.46 %	0 %	0 %	0 %

As can be seen at first glance in Fig.46, the Synchrotron emission contributes to the total energy by several orders of magnitude more than any other mechanisms. After that, SSC is the second most important energy source. The other contributions are smaller, with the NIR IC

being the weakest.

The fit can be studied in more detail to observe the degeneracy that exists between the magnetic field  $B$  and the electron density or amplitude of the ECBPWL. In order to do that, we fixed all other ECBPWL parameters except the amplitude and stored the least squares values [96], i.e. the function,

$$\chi^2(A, B) = \sum_i^N \frac{(\Phi_i^{\text{exp}} - \Phi_i^{\text{model}}(A, B))^2}{\sigma_i^2}. \quad (9)$$

Where  $N$  is the number of experimental points,  $\Phi_i^{\text{exp}}$  is the experimental SED value,  $\Phi_i^{\text{model}}$  is the corresponding value of the model, and  $\sigma_i$  is the respective error in the SED. All calculated for different amplitudes  $A$  and magnetic fields  $B$ . The result is shown in Fig.47. It can be seen that there is a preferential region in the  $A$ - $B$  plane that has a minimum at ( $A = 3.7 \times 10^{36} \text{ eV}^{-1}$ ,  $B = 119.33 \mu\text{G}$ ). There exists an inverse relation. As the SSC contribution depends only of the electron density, and not of the magnetic field (following current models [48]), the fit using this data will break the degeneracy.

It is important to note that the obtained electron distributions (see Fig.47) do not follow the power law slope that is naively expected from a simple Diffusive Shock Acceleration mechanism [43], which is  $\sim 2$ . The Crab Nebula spectrum cannot be explained with this assumption [96]. For this reason, we treat the electron distribution as a completely free parameter in order to obtain an empirical description of the electron distribution.

## 8 Conclusion

In this work we explored the analyzed data from the IACTs MAGIC and LST-1 taken in stereoscopic mode, that cover the energy range from 60 GeV to 30 TeV. Adding one more telescope to MAGIC was expected to improve the performance of the observations. Stereoscopic measurements with all three of these telescopes are something that has recently started to be used. For this reason there are still no publications by CTA or MAGIC on the stereoscopic performance (it will be published soon [69]). In this work we explored the methodology to understand all the steps and try to analyze in detail everything that the `magic-cta-pipe` does (the official MAGIC+LST-1 analysis pipeline [1]).

We performed a data selection for the study of the Crab Nebula, which is the standard candle in HE and VHE astronomy. This source can provide us with sufficient statistics despite the limited observation time available. This allows us to study the performance of the stereoscopic analysis compared to the MAGIC analysis, as well as comparing it with the analysis using LST-1 alone. Data was taken from two periods: 2020 and 2021 (pre-volcano eruption in La Palma) and from 2022 (post-volcano eruption). Diverse filters were applied, for example, runs with event rates that deviated significantly from the mean were discarded, and an intensity filter was applied at 80 p.e.. With that, we end up with 10.7 h of effective observation time, and  $\sim 3$  million events detected by all three telescopes.

A set of scripts was prepared to process all the runs, starting from raw files and generating DL2 and DL3 data [2] (see Fig.23). This processing utilizes the data available at the on-site computing cluster on the island of La Palma and can be used to process data from any source. With the script, all the calculations can be reproduced using the code at [2]. Using this approach, we processed all the data up to DL2 and DL3, allowing us to compare the reconstructed energies. In general, we achieved accurate reconstruction, except for certain specific combinations (see Fig.30

and Fig.31). We found that this mismatch was caused by the different MC simulations required for the analysis of different periods (some of which have not yet been generated). We also analyzed the artifacts found in the reconstructed positions of showers for DL2 data (see Fig.34). We found that the observed pattern disappears when we project the positions onto a plane where the showers are developing (see Fig.36), but this study has not yielded any completely conclusive findings. Relevant advances have been communicated to the people working on `magic-cta-pipe`.

With the DL2 data, a characterization of the instrument has been done. Different cuts in gammaness have been applied to separate hadronic showers from gamma ray showers. A 90 % dynamic gammaness cut and a fixed cut that maximizes the total significance of the signal (see Fig.38). The angular resolution (signal 68 % containment for a point source) has been calculated (see Fig.6). It was found that it is always approximately  $0.15^\circ$  below that achieved by LST-1 alone. Compared with MAGIC, they are similar, but for lower energies, the 3-telescope stereo setup shows a significant improvement in the angular resolution of 19 %. Also the integral sensitivity was computed , which refers to the flux capable of being detected with a sensitivity of  $5\sigma$  in 50 h (see Fig.41). For energies  $< 300 \text{ GeV}$ , the achieved integral sensitivity is 2.09 % C.U., and for energies  $> 300 \text{ GeV}$ , 0.79 % C.U. is obtained. For the case of lower energies, the minimum flux detectable with the 3-telescope setup is 34 % of the one for MAGIC (and 43 % relative to that of LST-1 standalone).

Finally, we used Gammapy tools to analyze the DL3 data [3]. The light curve and Spectral Energy Distribution (SED) were computed for the Crab Nebula. The light curve yielded a average flux of  $0.79 \pm 0.16 \times 10^{-9} \text{ cm}^{-2} \text{ s}^{-1}$ , very close to the reference value of MAGIC [78], but with a high error (see Fig.43), which is most likely due to the different behavior of the telescope after being stopped for a few months during the volcano eruption at La Palma (2021). The SED was computed and parameterized using a log parabola model (see Fig. 44 and Fig. 45), and then fitted again by adding Fermi-LAT data to cover energies around 10 GeV. Using only the data from this work, we found a Compton peak at 123 GeV, while with the Fermi-LAT data, the peak was found at 57 GeV.

A multiwavelength analysis was performed with data covering from radio to VHE (see Fig.46). The *Naima* radiative modeling package [95] was used to produce the SED model with synchrotron and the respective IC processes. Treating the electron population and the magnetic field as free parameters (assuming only that electrons follow an ECBWL) the fit was performed. Obtaining an amplitude of  $1.94 \times 10^{36} \text{ eV}^{-1}$  and a magnetic field of  $B = 119.33 \mu\text{G}$ . The results with our data suggest a lower energy contribution of the IC bump compared to that derived in the standard Naima model [99], but with no significant difference. Our results fit better in the HE and VHE ranges, but worse in the radio part of the spectrum. With the phenomenological fit, the electron population was determined without assuming any acceleration model, and a estimation of the magnetic field over the Crab Nebula was obtained.

## References

- [1] CTA collaboration. magic-cta-pipe. <https://github.com/cta-observatory/magic-cta-pipe>, 2023.
- [2] Jimenez J. stereo\_processing\_magic\_lst. [https://github.com/juanjq/stereo\\_processing\\_magic\\_lst.git](https://github.com/juanjq/stereo_processing_magic_lst.git), 2023.
- [3] Fabio Acero, Arnau Aguasca-Cabot, Johannes Buchner, and more. Gammapy: Python toolbox for gamma-ray astronomy. Zenodo, March 2023. <https://doi.org/10.5281/zenodo.7734804>.
- [4] W. L. Kraushaar, G. W. Clark, G. P. Garmire, R. Borken, P. Higbie, V. Leong, and T. Thorsos. High-Energy Cosmic Gamma-Ray Observations from the OSO-3 Satellite. *Astrophysical Journal*, 177:341, November 1972. <https://doi.org/10.1086/151713>.
- [5] C. E. Fichtel, R. C. Hartman, D. A. Kniffen, D. J. Thompson, G. F. Bignami, H. Ögelman, M. E. Özel, and T. Tümer. High-energy gamma-ray results from the second Small Astronomy Satellite. *Astrophysical Journal*, 198:163–182, May 1975. <https://doi.org/10.1086/153590>.
- [6] D. J. Thompson, C. E. Fichtel, D. A. Kniffen, and H. B. Ogelman. SAS-2 high-energy gamma-ray observations of the Vela pulsar. *Astrophysical Journal, Letters*, 200:L79–L82, September 1975. <https://doi.org/10.1086/181902>.
- [7] J. Clear, K. Bennett, R. Buccheri, I. A. Grenier, W. Hermsen, H. A. Mayer-Hasselwander, and B. Sacco. A detailed analysis of the high energy gamma-ray emission from the Crab pulsar and nebula. *Astronomy and Astrophysics*, 174:85–94, March 1987. <https://sci.esa.int/s/8ZkvxyxA>.
- [8] W. Hermsen. The Second COS-B Catalogue of High-Energy  $\gamma$ -ray Sources. *Philosophical Transactions of the Royal Society of London Series A*, 301(1462):519–521, June 1981. <https://doi.org/10.1098/rsta.1981.0127>.
- [9] T. C. Weekes, M. F. Cawley, D. J. Fegan, K. G. Gibbs, A. M. Hillas, et al. Observation of TeV Gamma Rays from the Crab Nebula Using the Atmospheric Cerenkov Imaging Technique. *Astrophysical Journal*, 342:379, July 1989. <https://doi.org/10.1086/167599>.
- [10] M. A. McLaughlin, J. R. Mattox, J. M. Cordes, and D. J. Thompson. Variability of CGRO/EGRET Gamma-Ray Sources. *Astrophysical Journal*, 473:763, December 1996. <https://doi.org/10.1086/178188>.
- [11] J. P. Roques, J. Paul, P. Mandrou, and F. Lebrun. The sigma mission on the granat satellite. *Advances in Space Research*, 10(2):223–232, January 1990. [https://doi.org/10.1016/0273-1177\(90\)90146-Q](https://doi.org/10.1016/0273-1177(90)90146-Q).
- [12] M. Ackermann, M. Ajello, W. B. Atwood, et al. 2FHL: The Second Catalog of Hard Fermi-LAT Sources. *Astrophysical Journal, Supplement*, 222(1):5, January 2016. <https://doi.org/10.3847/0067-0049/222/1/5>.
- [13] C. Winkler, T. J. L. Courvoisier, G. Di Cocco, N. Gehrels, A. Giménez, S. Grebenev, W. Hermsen, J. M. Mas-Hesse, F. Lebrun, N. Lund, G. G. C. Palumbo, J. Paul, J. P. Roques, H. Schnopper, V. Schönfelder, R. Sunyaev, B. Teegarden, P. Ubertini, G. Vedrenne, and A. J. Dean. The INTEGRAL mission. *Astronomy and Astrophysics*, 411:L1–L6, November 2003. <https://doi.org/10.1051/0004-6361:20031288>.
- [14] S. Abdollahi, F. Acero, M. Ackermann, M. Ajello, W. B. Atwood, et al. Fermi large area telescope fourth source catalog. *The Astrophysical Journal Supplement Series*, 247(1):33, mar 2020. <https://doi.org/10.3847/1538-4365/ab6bcb>.
- [15] Federico Di Pierro. Status of the Large-Sized Telescope of the Cherenkov Telescope Array. In *Journal of Physics Conference Series*, volume 2429 of *Journal of Physics Conference Series*, page 012020, February 2023. <https://doi.org/10.1088/1742-6596/2429/1/012020>.
- [16] G. di Sciascio and Lhaaso Collaboration. The LHAASO experiment: From Gamma-Ray Astronomy to Cosmic Rays. *Nuclear and Particle Physics Proceedings*, 279-281:166–173, October 2016. <https://doi.org/10.1016/j.nuclphysbps.2016.10.024>.
- [17] S. P. Swordy. The energy spectra and anisotropies of cosmic rays. *Space Science Reviews*, 99(1):85–94, Oct 2001. <https://doi.org/10.1023/A:1013828611730>.
- [18] IceCube Collaboration. First year performance of the IceCube neutrino telescope. *Astroparticle Physics*, 26(3):155–173, October 2006. <https://doi.org/10.1016/j.astropartphys.2006.06.007>.
- [19] V. Schoenfelder. The first comptel source catalogue. *Astron. Astrophys. Suppl. Ser.*, 143:145, 2000. <https://doi.org/10.1051/aas:2000101>.
- [20] R. C. Hartman, D. L. Bertsch, S. D. Bloom, A. W. Chen, P. Deines-Jones, J. A. Esposito, et al. The Third EGRET Catalog of High-Energy Gamma-Ray Sources. *Astrophysical Journal, Supplement*, 123(1):79–202, July 1999. <https://doi.org/10.1086/313231>.
- [21] William S. Paciesas, Charles A. Meegan, Geoffrey N. Pendleton, Michael S. Briggs, et al. The Fourth BATSE Gamma-Ray Burst Catalog (Revised). *Astrophysical Journal, Supplement*, 122(2):465–495, June 1999. <https://doi.org/10.1086/313224>.
- [22] Volker Schönfelder. Imaging principles and techniques in space-borne gamma-ray astronomy. *Nuclear Instruments and Methods in Physics Research A*, 525(1-2):98–106, June 2004. <https://doi.org/10.1016/j.nima.2004.03.029>.

- [23] Richard Kruse. Historic spacecraft website. <https://historicsspacecraft.com>, 2023.
- [24] W. B. Atwood, A. A. Abdo, M. Ackermann, W. Althouse, B. Anderson, M. Axelsson, L. Baldini, et al. The large area telescope on the fermi gamma-ray space telescope mission. *The Astrophysical Journal*, 697(2):1071, may 2009. <https://doi.org/10.1088/0004-637X/697/2/1071>.
- [25] Daniel Gomez Toro. *Temporal Filtering with Soft Error Detection and Correction Technique for Radiation Hardening Based on a C-element and BICS*. PhD thesis, Université de Bretagne Occidentale, 2014, 12 2014. <https://hal.science/tel-01191520>.
- [26] F. Aharonian, J. Buckley, T. Kifune, and G. Sinnis. High energy astrophysics with ground-based gamma ray detectors. *Rep. Prog. Phys.*, 71:96901–56, 09 2008. <https://dx.doi.org/10.1088/0034-4885/71/9/096901>.
- [27] Mathieu de Naurois and Daniel Mazin. Ground-based detectors in very-high-energy gamma-ray astronomy. *Comptes Rendus Physique*, 16(6):610–627, 2015. <https://doi.org/10.1016/j.crhy.2015.08.011>.
- [28] G. Puppi, H.S. Bridge, and K. Greisen. *Progress in Cosmic Ray Physics. Vol. 3. Edited by J.G. Wilson ... Contributors: K. Greisen, H.S. Bridge, R.W. Thompson, G. Puppi*. North-Holland Publishing Co, 1956.
- [29] Julian Sitarek. TeV Instrumentation: Current and Future. *Galaxies*, 10(1):21, 2022. <https://doi.org/10.3390/galaxies10010021>.
- [30] A. J. Smith and HAWC Collaboration. HAWC: Design, Operation, Reconstruction and Analysis. In *34th International Cosmic Ray Conference (ICRC2015)*, volume 34 of *International Cosmic Ray Conference*, page 966, July 2015. <https://doi.org/10.22323/1.236.0966>.
- [31] J V Jelley. Cerenkov radiation and its applications. *British Journal of Applied Physics*, 6(7):227, jul 1955. <https://dx.doi.org/10.1088/0508-3443/6/7/301>.
- [32] J. Holder, R.W. Atkins, H.M. Badran, G. Blaylock, S.M. Bradbury, J.H. Buckley, et al. The first veritas telescope. *Astroparticle Physics*, 25(6):391–401, 2006. <https://doi.org/10.1016/j.astropartphys.2006.04.002>.
- [33] Berrie Giebels and H. E. S. S. Collaboration. Status and recent results from H.E.S.S. *arXiv e-prints*, page arXiv:1303.2850, March 2013. <https://doi.org/10.48550/arXiv.1303.2850>.
- [34] J. Aleksić, S. Ansoldi, L.A. Antonelli, P. Antoranz, A. Babic, et al. The major upgrade of the magic telescopes, part i: The hardware improvements and the commissioning of the system. *Astroparticle Physics*, 72:61–75, 2016. <https://doi.org/10.1016/j.astropartphys.2015.04.004>.
- [35] CTA Collaboration. Cherenkov telescope array webpage, 2023. <https://www.cta-observatory.org/>.
- [36] Konrad Bernlöhr. Simulation of imaging atmospheric cherenkov telescopes with corsika and sim\_telarray. *Astroparticle Physics*, 30:149–158, 08 2008. <https://doi.org/10.1016/j.astropartphys.2008.07.009>.
- [37] Prity Rekha Das and Kalyanee Boruah. Gamma hadron separation method in ground-based gamma ray astronomy using simulated data. *Indian Journal of Physics*, 97(2):347–357, February 2023. <https://doi.org/10.1007/s12648-022-02423-y>.
- [38] and, , and and. Gamma/hadron segregation for a ground based imaging atmospheric cherenkov telescope using machine learning methods: Random forest leads. *Research in Astronomy and Astrophysics*, 14(11):1491, nov 2014. <https://doi.org/10.1088/1674-4527/14/11/012>.
- [39] Giuseppe Di Sciascio. Ground-based gamma-ray astronomy: an introduction. *Journal of Physics: Conference Series*, 1263(1):012003, jun 2019. <https://dx.doi.org/10.1088/1742-6596/1263/1/012003>.
- [40] V. P. Fomin, A. A. Stepanian, R. C. Lamb, D. A. Lewis, M. Punch, and T. C. Weekes. New methods of atmospheric Cherenkov imaging for gamma-ray astronomy. I. The false source method. *Astroparticle Physics*, 2(2):137–150, May 1994. [https://doi.org/10.1016/0927-6505\(94\)90036-1](https://doi.org/10.1016/0927-6505(94)90036-1).
- [41] D. Bose, V. R. Chitnis, P. Majumdar, and A. Shukla. Galactic and extragalactic sources of very high energy gamma rays. *European Physical Journal Special Topics*, 231(1):27–66, January 2022. <https://doi.org/10.1140/epjs/s11734-022-00434-8>.
- [42] Roger Blandford and David Eichler. Particle acceleration at astrophysical shocks: A theory of cosmic ray origin. *Physics Reports*, 154(1):1–75, October 1987. [https://doi.org/10.1016/0370-1573\(87\)90134-7](https://doi.org/10.1016/0370-1573(87)90134-7).
- [43] Matthew G. Baring. Diffusive shock acceleration: The Fermi mechanism. In *32nd Rencontres de Moriond: High-Energy Phenomena in Astrophysics*, pages 97–106, 1997.
- [44] Pierluca Carenza and Giuseppe Lucente. Revisiting axion-electron bremsstrahlung emission rates in astrophysical environments. *Phys. Rev. D*, 103:123024, Jun 2021. <https://doi.org/10.1103/PhysRevD.103.123024>.
- [45] T. Huege and H. Falcke. Principles of synchrotron emission in an astrophysical context. In Franco Mantovani and Andrzej Kus, editors, *The Role of VLBI in Astrophysics, Astrometry and Geodesy*, pages 13–27, Dordrecht, 2005. Springer Netherlands.
- [46] Robert Buschauer and Gregory Benford. General Theory of Coherent Curvature Radiation. *Monthly Notices of the Royal Astronomical Society*, 177(1):109–136, 10 1976. <https://doi.org/10.1093/mnras/177.1.109>.

- [47] M. Breuhaus, J. Hahn, C. Romoli, B. Reville, G. Giacinti, R. Tuffs, and J. A. Hinton. Ultra-high energy inverse compton emission from galactic electron accelerators. *The Astrophysical Journal Letters*, 908(2):L49, feb 2021. <https://doi.org/10.3847/2041-8213/abe41a>.
- [48] He Gao, Wei-Hua Lei, Xue-Feng Wu, and Bing Zhang. Compton scattering of self-absorbed synchrotron emission. *Monthly Notices of the Royal Astronomical Society*, 435(3):2520–2531, 09 2013. <https://doi.org/10.1093/mnras/stt1461>.
- [49] Ervin Kafexhiu, Felix Aharonian, Andrew M. Taylor, and Gabriela S. Vila. Parametrization of gamma-ray production cross sections for  $pp$  interactions in a broad proton energy range from the kinematic threshold to pev energies. *Phys. Rev. D*, 90:123014, Dec 2014. <https://doi.org/10.1103/PhysRevD.90.123014>.
- [50] Kevork N. Abazajian, Nicolas Canac, Shunsaku Horiuchi, and Manoj Kaplinghat. Astrophysical and dark matter interpretations of extended gamma-ray emission from the galactic center. *Phys. Rev. D*, 90:023526, Jul 2014. <https://doi.org/10.1103/PhysRevD.90.023526>.
- [51] NASA Goddard Space Flight Center. High Energy Astrophysics Science Archive Research Center. <https://heasarc.gsfc.nasa.gov/>, accessed April 2023.
- [52] I. F. Mirabel. Gamma-ray binaries revealed. *Science*, 335(6065):175–176, 2012. <https://doi.org/10.1126/science.1215895>.
- [53] P. Padovani. Gamma-Ray Emitting AGN and Unified Schemes. In Y. Giraud-Heraud and J. Tran Thanh van, editors, *Very High Energy Phenomena in the Universe; Moriond Workshop*, page 7, January 1997. <https://doi.org/10.48550/arXiv.astro-ph/9704002>.
- [54] HESS collaboration. First detection of vhe s from sn 1006 by hess. *A&A*, 516:A62, 2010. <https://doi.org/10.1051/0004-6361/200913916>.
- [55] H. Sano, H. Yamaguchi, M. Aruga, Y. Fukui, K. Tachihara, M. D. Filipović, and G. Rowell. An expanding shell of neutral hydrogen associated with sn 1006: Hints for the single-degenerate origin and faint hadronic gamma-rays. *The Astrophysical Journal*, 933(2):157, jul 2022. <https://doi.org/10.3847/1538-4357/ac7465>.
- [56] LIGO Scientific Collaboration and Virgo Collaboration. GW170817: Observation of Gravitational Waves from a Binary Neutron Star Inspiral. *Physical Review Letters*, 119(16):161101, October 2017. <https://doi.org/10.1103/PhysRevLett.119.161101>.
- [57] M. Meyer, D. Horns, and H. S. Zechlin. The Crab Nebula as a standard candle in very high-energy astrophysics. *Astronomy and Astrophysics*, 523:A2, November 2010. <https://doi.org/10.1051/0004-6361/201014108>.
- [58] G. Dubner, G. Castelletti, O. Kargaltsev, G. G. Pavlov, M. Bietenholz, and A. Talavera. Morphological properties of the crab nebula: A detailed multiwavelength study based on new vla, hst, chandra, and xmm-newton images. *The Astrophysical Journal*, 840(2):82, may 2017. <https://doi.org/10.3847/1538-4357/aa6983>.
- [59] CTA collaboration. cta-lstchain. <https://github.com/cta-observatory/magic-cta-pipe>, 2023.
- [60] conda-forge/packages/protozfits. protozfits 2.2.0. Python bindings for the CTA zfits reader, June 2023. [Online]. Available: <https://gitlab.cta-observatory.org/cta-computing/common/acada-array-elements/adh-apis>.
- [61] C. Deil, R. Zanin, J. Lefaucheur, C. Boisson, B. Khelifi, J. Watson, R. Lopez-Coto, CTA Consortium, et al. Gammapy - A prototype for the CTA science tools. In *35th International Cosmic Ray Conference (ICRC2017)*, volume 301 of *International Cosmic Ray Conference*, page 766, January 2017. <https://doi.org/10.48550/arXiv.1709.01751>.
- [62] D. C. Wells, E. W. Greisen, and R. H. Harten. FITS - a Flexible Image Transport System. *Astronomy and Astrophysics, Supplement*, 44:363, June 1981.
- [63] A. Moralejo, M. Gaug, E. Carmona, P. Colin, C. Delgado, S. Lombardi, D. Mazin, V. Scalzotto, J. Sitarek, and D. Tescaro. MARS: The MAGIC Analysis and Reconstruction Software. *Astrophysics Source Code Library*, record ascl:1011.004, November 2010.
- [64] Rene Brun and Fons Rademakers. ROOT - an object oriented data analysis framework. *Nucl. Inst. & Meth. in Phys. Res. A*, 389(1):81–86, 1997. [https://doi.org/10.1016/S0168-9002\(97\)00048-X](https://doi.org/10.1016/S0168-9002(97)00048-X).
- [65] CTA-LST Project. Observations of the crab nebula and pulsar with the large-sized telescope prototype of the cherenkov telescope array, 2023.
- [66] S Agarwal, B Banerjee, A Shukla, J Roy, S Acharya, B Vaidya, V R Chitnis, S M Wagner, K Mannheim, and M Branchesi. Flaring activity from magnetic reconnection in BL Lacertae. *Monthly Notices of the Royal Astronomical Society: Letters*, 521(1):L53–L58, 03 2023. <https://doi.org/10.1093/mnrasl/slad023>.
- [67] MAGIC collaboration. Magic tev gamma-ray observations of markarian 421 during multiwavelength campaigns in 2006. *A&A*, 519:A32, 2010. <https://doi.org/10.1051/0004-6361/200913945>.
- [68] A. Berti, F. Di Pierro, J Sitarek, and Y. Suda. School on magic+lst data analysis. Online event, February 2023.

- [69] CTA Collaboration. Performance of the joint lst-1 and magic observations evaluated with crab nebula observations. Draft version, April 4, 2023, in preparation.
- [70] A. Moralejo and R. Lopez-Coto. School on lst data analysis. Online event, January 2022. <https://doi.org/10.48550/arXiv.2306.12960>.
- [71] T. P. Li and Y. Q. Ma. Analysis methods for results in gamma-ray astronomy. *Astrophysical Journal*, 272:317–324, September 1983. <https://doi.org/10.1086/161295>.
- [72] M Linhoff, M Peresano, P Michael Dominik, J Sitarek, T Vuillaume, M Punch, L Nickel, N Biederbeck, G Maier, A Moralejo, L Jouvin, G Verna, and H van Kemenade. cta-observatory/pyirf. Zenodo, June 2023. <https://doi.org/10.5281/zenodo.7741289>.
- [73] MAGIC Collaboration. The major upgrade of the MAGIC telescopes, Part II: A performance study using observations of the Crab Nebula. *Astroparticle Physics*, 72:76–94, January 2016. <https://doi.org/10.1016/j.astropartphys.2015.02.005>.
- [74] Vovk, I., Strzys, M., and Fruck, C. Spatial likelihood analysis for magic telescope data - from instrument response modelling to spectral extraction. *A&A*, 619:A7, 2018. <https://doi.org/10.1051/0004-6361/201833139>.
- [75] Abelardo Moralejo. Lst-1, the large-sized telescope prototype of cta. status and first observations. *Journal of Physics: Conference Series*, 2156(1):012089, dec 2021. <https://doi.org/10.1088/1742-6596/2156/1/012089>.
- [76] N. Gehrels. Use of  $\nu F_\nu$  spectral energy distributions for multiwavelength astronomy. *Nuovo Cimento B Serie*, 112B(1):11–15, January 1997.
- [77] E. Massaro, M. Perri, P. Giommi, and R. Nesci. Log-parabolic spectra and particle acceleration in the BL Lac object Mkn 421: Spectral analysis of the complete BeppoSAX wide band X-ray data set. *Astronomy and Astrophysics*, 413:489–503, January 2004. <https://doi.org/10.1051/0004-6361:20031558>.
- [78] MAGIC collaboration. Measurement of the Crab Nebula spectrum over three decades in energy with the MAGIC telescopes. *Journal of High Energy Astrophysics*, 5:30–38, March 2015. <https://doi.org/10.1016/j.jheap.2015.01.002>.
- [79] HESS collaboration. Observations of the crab nebula with hess. *A&A*, 457(3):899–915, 2006. <https://doi.org/10.1051/0004-6361:20065351>.
- [80] HEGRA collaboration. The energy spectrum of tev gamma rays from the crab nebula as measured by the hegра system of imaging air cerenkov telescopes. *The Astrophysical Journal*, 539(1):317, aug 2000. <https://doi.org/10.1086/309225>.
- [81] MAGIC Collaboration. Constraining very-high-energy and optical emission from FRB 121102 with the MAGIC telescopes. *Monthly Notices of the Royal Astronomical Society*, 481(2):2479–2486, 09 2018. <https://doi.org/10.1093/mnras/sty2422>.
- [82] MAGIC collaboration. Performance of the magic stereo system obtained with crab nebula data. *Astroparticle Physics*, 35(7):435–448, 2012. <https://doi.org/10.1016/j.astropartphys.2011.11.007>.
- [83] LST-CTA. Status and results of the prototype LST of CTA. *PoS*, ICRC2021:872, 2021. <https://doi.org/10.22323/1.395.0872>.
- [84] M. Gaug, S. Fegan, A. M. W. Mitchell, M. C. Maccarone, T. Mineo, and A. Okumura. Using muon rings for the calibration of the cherenkov telescope array: A systematic review of the method and its potential accuracy. *The Astrophysical Journal Supplement Series*, 243(1):11, jul 2019. <https://doi.org/10.3847/1538-4365/ab2123>.
- [85] Fermi Collaboration. Fermi large area telescope observations of the crab pulsar and nebula. *The Astrophysical Journal*, 708(2):1254, dec 2009. <https://doi.org/10.1088/0004-637X/708/2/1254>.
- [86] Masanori Arakawa, Masaaki Hayashida, Dmitry Khangulyan, and Yasunobu Uchiyama. Detection of Small Flares from the Crab Nebula with Fermi-LAT. *Astrophysical Journal*, 897(1):33, July 2020. <https://doi.org/10.3847/1538-4357/ab9368>.
- [87] J. W. M. Baars and A. P. Hartsuijker. The Decrease of Flux Density of Cassiopeia A and the Absolute Spectra of Cassiopeia A, Cygnus A and Taurus A. *Astronomy and Astrophysics*, 17:172, March 1972. <https://doi.org/10.1016/j.jheap.2015.01.002>.
- [88] J. F. Macías-Pérez, F. Mayet, J. Aumont, and F. X. Désert. Global Spectral Energy Distribution of the Crab Nebula in the Prospect of the Planck Satellite Polarization Calibration. *Astrophysical Journal*, 711(1):417–423, March 2010. <https://doi.org/10.1088/0004-637X/711/1/417>.
- [89] P. G. Mezger, R. J. Tuffs, R. Chini, E. Kreysa, and H. P. Gemund. Maps of Cassiopeia A and the Crab nebula at lambda 1.2 mm. *Astronomy and Astrophysics*, 167:145–150, October 1986.
- [90] Bandiera, R., Neri, R., and Cesaroni, R. The crab nebula at 1.3 mm\* - evidence for a new synchrotron component. *A&A*, 386(3):1044–1054, 2002. <https://doi.org/10.1051/0004-6361:20020325>.
- [91] Robert P. Kirshner. Spectrophotometry of the Crab Nebula. *Astrophysical Journal*, 194:323–328, December 1974. <https://doi.org/10.1086/153248>.

- 
- [92] Gregory S. Hennessy, Robert W. O'Connell, Kwang P. Cheng, Ralph C. Bohlin, Nicholas R. Collins, Theodore R. Gull, Paul Hintzen, Joan E. Isensee, and more. Ultraviolet Imaging Telescope Observations of the Crab Nebula. *Astrophysical Journal, Letters*, 395:L13, August 1992. <https://doi.org/10.1086/186477>.
  - [93] Willingale, R., Aschenbach, B., Griffiths, R. G., Sembay, S., Warwick, R. S., Becker, W., Abbey, A. F., and Bonnet-Bidaud, J.-M. New light on the x-ray spectrum of the crab nebula. *A&A*, 365(1):L212–L217, 2001. <https://doi.org/10.1051/0004-6361:20000114>.
  - [94] E. Jourdain and J. P. Roques. The high-energy emission of the crab nebula from 20 kev to 6 mev with integral spi\*. *The Astrophysical Journal*, 704(1):17, sep 2009. <https://doi.org/10.1088/0004-637X/704/1/17>.
  - [95] V. Zabalza. naima: a python package for inference of relativistic particle energy distributions from observed nonthermal spectra. *Proc. of International Cosmic Ray Conference 2015*, page 922, 2015.
  - [96] Dirson, L. and Horns, D. Phenomenological modelling of the crab nebula's broadband energy spectrum and its apparent extension. *A&A*, 671:A67, 2023. <https://doi.org/10.1051/0004-6361/202243578>.
  - [97] K Cheng, Terri Tl Cheung, M Lau, Peter Yu, and P Kwok. Could very high energy gamma rays from the crab nebula result from p-p collision? *Journal of Physics G: Nuclear and Particle Physics*, 16:1115, 01 1999. <https://doi.org/10.1088/0954-3899/16/7/022>.
  - [98] A. Borione, M. A. Catanese, M. C. Chantell, C. E. Covault, J. W. Cronin, B. E. Fick, L. F. Fortson, and more. A Search for Ultra-High-Energy Gamma-Ray Emission from the Crab Nebula and Pulsar. *Astrophysical Journal*, 481(1):313–326, May 1997. <https://doi.org/10.1086/304042>.
  - [99] Dmitry Khangulyan, Masanori Arakawa, and Felix Aharonian. Detection of ultra-high-energy gamma rays from the Crab Nebula: physical implications. *Monthly Notices of the Royal Astronomical Society*, 491(3):3217–3224, 12 2019. <https://doi.org/10.1093/mnras/stz3261>.
  - [100] VIRGINIA TRIMBLE. The distance to the crab nebula and np 0532. *Publications of the Astronomical Society of the Pacific*, 85(507):579–585, 1973.
  - [101] E. E. Becklin and D. E. Kleinmann. Infrared Observations of the Crab Nebula. *Astrophysical Journal, Letters*, 152:L25, April 1968. <https://doi.org/10.1086/180171>.
  - [102] P. L. Marsden, F. C. Gillett, R. E. Jennings, J. P. Emerson, T. de Jong, and F. M. Olnon. Far-infrared observations of the Crab nebula. *Astrophysical Journal, Letters*, 278:L29–L32, March 1984. <https://doi.org/10.1086/184215>.
  - [103] Planck Collaboration. Planck 2018 results. VI. Cosmological parameters. *Astronomy and Astrophysics*, 641:A6, September 2020. <https://doi.org/10.1051/0004-6361/201833910>.
  - [104] Federico Fraschetti. Effect of Acceleration and Escape of Energetic Particles on Spectral Steepening at Shocks. *Astrophysical Journal, Letters*, 909(1):42, March 2021. <https://doi.org/10.3847/1538-4357/abd699>.
  - [105] Pauli Virtanen, Ralf Gommers, Travis E. Oliphant, Matt Haberland, Tyler Reddy, David Cournapeau, and more. SciPy 1.0: Fundamental Algorithms for Scientific Computing in Python. *Nature Methods*, 17:261–272, 2020. <https://doi.org/10.1038/s41592-019-0686-2>.
  - [106] A. M. Atoyan and F. A. Aharonian. On the mechanisms of gamma radiation in the Crab Nebula. *Monthly Notices of the RAS*, 278(2):525–541, January 1996. <https://doi.org/10.1093/mnras/278.2.525>.
  - [107] Anaconda, Inc. Anaconda software distribution. <https://www.anaconda.com>, 2023.

## A Instructions for the processing

A detailed description of all the steps in the pipeline are described below. As well as step-by-step instructions on how to use it. The scripts are prepared to run in the *IT cluster*, since it uses files that are there. But you can still run it from outside if you download the files and use them from another location, changing the paths. All the scripts and notebooks can be downloaded from the GitHub that has been prepared for this work [2].

As explained in section 4.1 and is sketched in Fig.23, the already available data is, for the case of MAGIC; the calibrated data, and in the case of LST-1; the DL1 stage. MAGIC data is found at `/fefs/onsite/common/MAGIC/data/MX/event/Calibrated` (with MX being M1 for MAGIC-1 and M2 for MAGIC-2) and LST-1 DL1 data at `/fefs/aswg/data/real/DL1`. Also the MC files are already processed, and are located at the respective subdirectory of `/fefs/aswg/LST1MAGIC/mc/models`.

Before starting with the running of the pipeline, some considerations should be taken and the files need to be configured for the analysis you want to perform. The main parameters that can be changed in the `config.yaml` file inside the `config_files` folder. The parameters that can be selected are summarized here:

- *Source name.* The source that is being studied can be changed. Using the `source_name` variable in `config.yaml` the source can be specified by its standard name. Otherwise the exact coordinates can also be specified.
- *Interpolation method.* Changing `interpolation_method` in `config.yaml` to `nearest` (no interpolation), `linear` or `cubic` the interpolation method to use the IRFs can be specified.
- *Cut types.* For the cuts applied in gammaness and  $\theta^2$  a fixed cut or a dynamic cut can be specified with the variable `cut_type` in `config.yaml`. For a fixed cut, use `global`, and for a dynamic one `dynamic`. The cut values or efficiencies can also be specified.
- *Mean method.* The method to apply the mean of parameters can be specified in the scripts `script_merge_and_mean.py` in the `bash_scripts/bash_merge_and_mean` folders. As explained in section 4.4, the weight types can be selected changing the variable `weight_type` to `simple`, `intensity` or `variance`.
- *MC files.* The MC directories should be changed in order to analyse other sources different than the Crab Nebula. The correct declination and NSB should be selected.
- *Selecting runs.* In order to select the runs you want to analyse of a determined source, the notebook `create_configuration_txt_files.ipynb` inside the folder `notebooks_data-generation` will be used to read the stereo log archive (the updated version can be downloaded from ). In this notebook the runs can be filtered by source name, amount of observation time of observations, type of wobble, time of same wobble, and many other parameters. Once filtered, two configuration `.txt` files will be generated with the MAGIC and LST run numbers.

Once the configuration files have been prepared, we can start running the scripts to obtain the processed files and then, the physical results. The notebooks need to be run with the Anaconda [107] environment `magic-cta-pipe` [1]. The steps that need to be performed, in the order that they should be applied are the following:

1. **MAGIC calibration to DL1.** The DL1 data is already computed for LST-1 but this is not the case of MAGIC, so the first step will be process the MAGIC calibrated data to DL1.

The starting point will be subrun-wise calibrated MAGIC files, a set of files per run, and per telescope. In the prepared GitHub [2], inside the folders `bash_scripts/bash_magic_cal_to_dl1`, the Bash script `cal_to_dl1.sh` sends the fragmented jobs to the *IT cluster* queues. This script will generate a folder per observation night (group of 2 to 10 runs), containing the DL1 MAGIC files, merged run-wise.

2. **DL1 stereo coincidences.** Once we have all the data in the same stage and format (DL1), the stereo information can be extracted, finding the coincidence of the events. The Bash script `dl1_to_stereo.sh` located in the folders `bash_scripts/bash_dl1_to_stereo` has to be run. This script find the coincident events between telescopes as explained in section 2.3.1, and then create a unique DL1 files per telescope. The files are stored in a folder per each LST-1 run and in subrun-wise format.
3. **DL1 to DL2.** All DL1 data is processed with those scripts to DL2. In this step the RF files need to be input, the source path can be changed in order to use different RFs. The script `stereo_to_dl2.sh` is located in the GitHub folder `bash_scripts/bash_stereo_to_dl2`. Running it will generate a DL2 file per run, and will store it in a unique folder (that can be specified).
4. **Create IRFs and DL2 to DL3.** Before obtaining the DL3 data, the specific IRFs need to be produced. The notebook `create_irfs_and_dl2_to_dl3.ipynb` inside the folder `notebooks_dl2_to_dl3` in the GitHub should be run. The first part of this notebook generate the IRFs given the required MC files, and it store them in one folder. Then, the second part of the notebook processes the DL2 data to DL3, creating the respective index files. The DL3 data is also stored run-wise in a unique folder.
5. **Standalone datasets.** In order to compare the data obtained with this analysis with data obtained with individual telescopes analysis, the notebook `create_lst_only_hdf.ipynb` inside `notebooks_data_generation` folder should be run in order to obtain the LST-1 standalone dataset. For the case of MAGIC, the notebook `create_melibea_hdf.ipynb` in the same folder should be run. Both will select the exact same events that have been analysed for the three telescopes and will create a DL2 dataset with these events in `.hdf5` format.
6. **MC dataset.** In order to do some comparisons with gamma-ray MCs a dataset with enough statistics of MC simulations can be created using the notebook `create_mc_dataframes.ipynb` inside `notebooks_data_generation`. A unique `.hdf` file of DL2 data will be created.
7. **Mean and merge DL2.** This set of scripts use the tool `get_dl2_mean` from `magic-cta-pipe` to the DL2 data that is obtained for each telescope and performs a mean of the parameters (weighted by the inverse of the variances). As the direction, energy and gammaness parameters are calculated for each telescope a mean should be computed in order to obtain a unique value for a determined event (as explained in section 4.4). The bash script `merge_and_mean.sh` inside the folders `bash_scripts/bash_merge_and_mean` folder should be run (it can be sent to the queue of the IT cluster). The script also generates a DL2 merged dataset with all the runs that has been processed.
8. **Coincidences datasets.** In the second step of this chain the event coincidence finding has been performed. In the generated files there are more information than the DL1 data. Additional information is also stored in the keys `coincidence/profile` and `coincidence/feature` of the `.hdf5` files. The first one containing the number of coincident events for the different tried time offsets (see section 2.3.1), and the latter one containing the timestamps and pointings of the different telescopes for each event. This information is merged for all runs and stored in two unique `.hdf5` file. This is achieved running the notebook `create_coincidences_datasets.ipynb` inside `notebooks_data_generation` folder.

**9. Add complementary data.** The last step to perform is adding some additional data to the DL2 files. These scripts add data to the before generated files, with the selected number of off regions, it calculates the  $\theta^2$  parameter (see section 2.3.1) for the ON and OFF regions. It also add another supplementary information as can be the zenith distance (from the altitude coordinate) only for commodity in the further analysis. The scripts can be run with the notebook `dl2_additional_data.ipynb` inside `notebooks_data_generation` folder.

With that, all the data has been processed, and different files with all the information have been stored. Now the physical analysis can start to be done. It can be divided in three main parts.

1. *Data sample analysis.* The notebooks to analyse the dataset itself, in order to characterise it well. Also the quality of the data is checked and runs can be filtered. The notebooks are located at the folder `notebooks_analysis_dataset`.
2. *DL2 analysis.* The notebooks located at the folder `notebooks_analysis_dl2` are in general to analyse different aspects of the DL2 data. The gammaness, intensity, energy, IRFs, etc is analysed in the different notebooks. In the sub-folder `arrival_positions`, the artifact explained in section 6.3 is analysed in different notebooks.
3. *DL3 analysis.* The higher analysis is done using Gammapy, so the Anaconda [107] environment that should be used now need to contain the last version of Gammapy. The environment `gammapy-v1.0` can be used.